Stony Brook University

The role of magmatic volatiles in igneous systems on Mars: Inferences from martian meteorites and experimental investigations.

A Dissertation Presented

by

Francis Michael McCubbin

to

The Graduate School

in Partial fulfillment of the

Requirements

for the Degree of

Doctor of Philosophy

in

Geosciences

Stony Brook University

May 2009

Stony Brook University

The Graduate School

Francis Michael McCubbin

We, the dissertation committee for the above candidate for the
Doctor of Philosophy degree,
hereby recommend acceptance of this dissertation.

Dr. Hanna Nekvasil, Advisor
Professor, Department of Geosciences

Dr. Scott M. McClennan Chairperson of Defense
Professor, Department of Geosciences

Dr. Timothy D. Glotch
Assistant Professor, Department of Geosciences

Dr. Donald H. Lindsley
Professor Emeritus, Department of Geosciences

Dr. James D. Webster
Curator of Mineral Deposits, Department of Earth and Planetary Sciences,
American Museum of Natural History, New York, NY

This dissertation is accepted by the Graduate School

Lawrence Martin
Dean of the Graduate School

Abstract of the Dissertation

The role of magmatic volatiles in igneous systems on Mars: Inferences from martian meteorites and experimental investigations.

By

Francis Michael McCubbin

in

Geosciences

Stony Brook University

2009

Magmatic volatiles, specifically water, fluorine, chlorine and sulfur, play important and diverse roles in silicate melts by controlling many physiochemical processes such as thermal stabilities of minerals and melts, melt density and viscosity, magma eruptive processes, and the formation of hydrothermal fluids that transport economically important metals. Some of these volatiles, perhaps most notably water, likely play a crucial role in the origin of life. Although the terrestrial magmatic volatile budget is well constrained, much remains uncertain about the martian volatile budget. Mars has commonly been referred to as a "volatile-rich" planet, and there is little doubt about the presence of frozen water-ice at the martian poles and abundant Cl and S in rocks, soils and dust. Yet, contradictory information abounds, particularly regarding magmatic water contents and the accepted mantle water budget for Mars.

This body of work provides the first studies focused on assessing the volatile budget of martian magmas and exploring the implications of these volatiles on ancient martian igneous and hydrothermal systems. We report, through textural analysis and electron probe microanalysis (EPMA) of minerals in martian meteorites, strong evidence for water, F, and Cl-bearing magmas and strong evidence for both water-rich and chlorine-rich hydrothermal fluids in martian magmatic systems. We collected new secondary ion mass spectrometry (SIMS) data on kaersutite from the Chassigny meteorite, which we use to show that at least some magma source regions on Mars likely have water contents similar to terrestrial values. In order to show that low-OH F-Cl apatite analyses obtained from the Chassigny meteorite are viable compositions (these compositiojns are rare in terrestrial rocks), low-OH F-Cl apatite was synthesized and characterized by EPMA, single-crystal X-ray diffraction and various nuclear magnetic resonance (NMR) techniques. Finally, the effect of water on the compositional diversity of magmas that can be produced from fractionation of a martian liquid at the base of a thick crust was investigated experimentally. Using a synthetic powder modeled after Humphrey (a picrobasalt analyzed in Gusev Crater, Mars), we verified the possibility of igneous crustal stratification, which does not require large-scale lithologic diversity among rocks on the martian surface.

Dedication

First and foremost, I would like to thank my mother, Joyce Marie Mazur for all of her love and support. Without her, I would not be where I am today. I would also like to thank my girlfriend, Lisa Ann Stallings, whose patience and support have helped me through many tumultuous times. I would also like to dedicate this work to the loving memories of my father, Francis Michael McCubbin Sr., and my grand parents Charles Francis Lawyer, and Elsie Lee Lawyer. Their collective love and support provided me with the strength and confidence I needed to become the scientist I am today.

Table of Contents

List of Figures

List of Tables

Acknowledgments

First, I would like to acknowledge my advisor Hanna Nekvasil, and my unofficial co-advisor Donald H. Lindsley. Without their help and intellectual support, this work would not have been possible. I also thank Guy Consolmagno of the Vatican Observatory, Robert Dodd (formerly at Stony Brook University) and the Meteorite curatorial staff at the Lyndon B. Johnson Space Center in Houston, TX for providing us with thin sections of martian meteorites. In addition, the work presented in this dissertation was strengthened by many helpful and productive scientific conversations with Alexander Smirnov, Charles Mandeville, Darby Dyar and Laurie Leshin. I am also grateful to Alexander Smirnov, Charles Mandeville, J. F. Britten and Yu-Sheng Chen for assistance with use of of various analytical instruments. I would also like to thank Alan Boudreau, Molly McCanta, Rhian Jones, Robert Dymek, John M. Hughes, Michael Fechtelkord, Richard Thompson and Harry McSween for insightful reviews of various portions of this work. Financial support for this work was provided by NASA grant NNG04GM79G from the Mars Fundamental Research Program awarded to Hanna Nekvasil. I was grateful for a GAANN fellowship. Grants NSF-DMR 0452444 and EAR-0510501 awarded to John Parise also aided in financially supporting this work.

Maskelynite-hosted apatite in the Chassigny meteorite: Insights into late-stage magmatic volatile evolution in martian magmas.

Francis M. McCubbin[1] and Hanna Nekvasil[1]

[1]Department of Geosciences, Stony Brook University, Stony Brook, New York 11794-2100, U.S.A.

Manuscript published in American Mineralogist, April, 2008

1.1. Introduction

The Chassigny martian meteorite is representative of the Chassignite class of SNC meteorites. It is a cumulate dunite (Floran et al., 1978; McSween and Treiman, 1998; Nekvasil et al., 2007) with cumulus olivine and spinel, and intercumulus pyroxene, maskelynite, apatite, ilmenite, and sulfides. Olivine-hosted polyphase "melt" inclusions (MI) contain augite, low-Ca pyroxene, kaersutite, pyrrhotite, chromite, pentlandite, Ti-biotite, apatite, rhyolitic glass, maskelynite, ilmenite, and rare Al-rich chromite (Floran et al., 1978; Johnson et al., 1991; McCubbin et al., 2006a; Nekvasil et al., 2007; Nekvasil et al., 2003). Although the Chassigny meteorite has been extensively studied (Floran et al., 1978; Johnson et al., 1991; e.g., Mason et al., 1975; Varela et al., 2000; Wadhwa and Crozaz, 1995), the cumulate nature of the meteorite has made it difficult to constrain the chemical characteristics of the melts associated with its formation. The unknown volatile contents of these liquids and uncertainties regarding volatile evolution during crystallization further complicate petrogenetic interpretations.

Volatiles play a critical role in magmatic systems by controlling many physiochemical processes such as thermal stabilities of minerals and melts, melt density and viscosity, magma eruptive processes, and transport of economically important metals. Three common volatiles in terrestrial magmas are water, fluorine, and chlorine,

and the literature contains extensive information concerning the effects of these volatiles in magmatic systems (Burnham, 1994; Candela, 1986a; e.g., Candela, 1986b; Carroll and Webster, 1994; Halter and Webster, 2004; Mathez and Webster, 2005; Webster, 1992a; Webster, 1992b; Webster, 1997a; Webster, 1997b; Webster, 2004; Webster and De Vivo, 2002; Webster et al., 1999; Webster and Rebbert, 1998). Evidence for the presence of volatiles in martian magmas is preserved in the volatile-bearing mineral phases of the martian meteorites. In the Chassigny meteorite, it is preserved in apatite of the melt inclusions and in regions interstitial to the cumulus phases, and in the kaersutite and biotite of the melt inclusions (e.g., Floran et al., 1978; Johnson et al., 1991). These minerals contain F^-, Cl^-, and OH^-, suggesting the likelihood of elevated amounts of dissolved volatiles in the trapped melt. The effect that these volatiles may have had on the mineral assemblages depends not only upon their abundances, but also on the conditions under which crystallization took place. Open-system conditions in which fluids can leave and enter the system, and closed system conditions in which exsolved fluids are retained into the subsolidus thermal regime may have widely differing effects on the sequence of appearance of minerals, mineral compositions, and hydrothermal processes.

Within cumulate horizons of a magma body, there are two primary crystallization environments: that within melt pockets that were incorporated during growth of the cumulus grains, and that of the interstitial region between cumulus grains. Cumulus minerals such as olivine that possess good mechanical strength and lack cleavage can retain volatiles in melt inclusions. In fact, as summarized in Veksler (2006), melt inclusions in structurally-sound hosts may be of particular use in understanding volatile evolution in magmas in general because they potentially retain more volatiles than ascending de-gassing magma. This is not to say that melt inclusions see a completely closed environment; interactions with the host are to be expected. In the case of olivine, these likely involve Fe:Mg exchange which results in Fe-loss from the melt to the olivine and inhibits the expected Fe-enrichment of crystallizing ferromagnesian phases with dropping temperature (e.g., Danyushevsky et al., 2002, 2004; Gaetani and Watson, 2002), and the production of orthopyroxene by reaction with the evolving liquid. Importantly, however, closed system behavior with respect to magmatic volatiles and fluids may be common.

The intercumulus environment is similar to that within the melt inclusions with respect to interactions with the volumetrically dominant cumulus minerals. However, from a volatile standpoint, it can be quite different. Depending upon the porosity and permeability of the cumulus layer, open-system conditions may prevail interstitially as these regions become conduits for fluid and melt migration during cooling and compaction. Such open-system processes are well documented on Earth in layered intrusions (Boudreau, 1993; Boudreau and McCallum, 1989; Boudreau and McCallum, 1992; Mathez, 1995; e.g., Mathez et al., 1985; Meurer and Boudreau, 1996).

Because of the major effects of volatiles on mineral stability and chemistry, it is anticipated that even with similar starting compositions the differences in volatile behavior in melt inclusions vs. the interstitial regions may lead to significantly different mineral assemblages in these two environments. For this work, we focus on identifying differences in apatite-hosting late-stage feldspar glass (maskelynite) and the included apatite from these two environments within the Chassigny meteorite, and we use these differences to assess the behavior of magmatic volatiles in each environment.

1.2. Analytical / Data Reduction Techniques

Two thin-sections of the Chassigny meteorite (from the Vatican Observatory [slide # P8064] and from the collection of Dr. Robert Dodd [no sample number available]) were studied petrographically and via electron probe microanalysis (EPMA) in order to evaluate the nature of apatite and its hosting phases and to identify any differences in apatite chemistry associated with different hosts.

Electron probe microanalysis was performed using a Cameca Camebax electron microprobe (EMP) equipped with four wavelength dispersive spectrometers, one of which was equipped with an OV-60 detector crystal, which was used to obtain accurate fluorine analyses. An accelerating voltage of 15 kV and a nominal beam current of 10 nA were used during analysis. For apatite and Na-bearing phases, the largest possible raster size was used to minimize unknown analytical problems that occur during highly focused electron beam analysis on such matrices.

Feldspathic glass was analyzed and assessed as to whether it represents maskelynite or a rhyolitic glass composition. Previous workers (e.g., Morgan and London, 1996; Morgan and London, 2005) have shown that EMP analyses of small patches of Na-rich

glass, particularly hydrous glass, commonly show Na loss as suggested by the presence of normative quartz (*Qz*) and corundum (*Co*). Our electron microprobe analyses of feldspathic glass similarly show normative (*Qz*) and (*Co*). Na-loss during analysis was directly observed by time-zero microprobe analysis of the feldspathic glass. In spite of probable Na loss, recognition of feldspar stoichiometry can be made by looking at (i) the cation sum, which for feldspar should be close to 5 per 8 oxygens (ii) the sum of Ca + Na + K which should be near 1 atom (iii) Si + Al (+Fe) which should be near 4, and (iv) Al (+Fe) should be close to Ca + 1. Clearly (i) and (ii) are directly affected by alkali loss while (iii) and (iv) are only indirectly affected (because of the "wrong" number of oxygens). If addition of Na_2O simultaneously causes normative *Co* and *Qz* to disappear and (i)-(iv) to be satisfied, there is a very strong presumption that the analysis represents a stoichiometric feldspar that has undergone alkali loss during analysis. Table 1.1 shows both the maskelynite EMP analysis as well as the results of this evaluation once Na_2O is added back to the analysis until either all normative *Co* or *Qz* has been consumed. We conclude that all feldspathic glass analyzed during this study is maskelynite.

EMP analysis of F and Cl in apatite is susceptible to a problem: anisotropic diffusion of fluorine and chlorine during EMP analysis up the c-axis channels of apatite towards the electron beam (Stormer et al., 1993). This results in over-counting of F and Cl and can be readily seen in time studies in which the extent of time of exposure to the electron beam is varied systematically. Stormer et al. (1993) noted that this effect was minimized if analysis down the c-axis is avoided. For this study, care was taken to avoid analysis of crystals oriented with the c-axis parallel to the beam (as determined by crystal morphology). However, much of the apatite within the Chassigny meteorite is very small (~1-2 □m in the shortest dimension of the melt-inclusion apatite), and the effects of such a focused beam, even on analysis down the a-axis, are unknown and may still result in the over-counting of fluorine and chlorine. Importantly, there is no evidence that this effect perturbs the F:Cl ratio, only the total halogen abundance. Reproducibility of the measured F contents were verified by analyses of the same grains at the American Museum of Natural History, the Geophysical Lab, and Stony Brook University.

Due to the small size of the apatite crystals, microprobe analysis of apatite often resulted in overlap with an adjacent phase. In these instances, the adjacent phase was also analyzed, and an appropriate subtraction and renormalization was performed so that the reported analyses represent only the apatite phase. Hydroxyl was not measured directly in this study; it was calculated by difference, assuming that only fluorine, chlorine, and hydroxyl populate the apatite X-site and that the X-site sums to one when the analysis is normalized to 13 anions.

1.3. Results

1.3.1. Petrographic textural analysis

Petrographic observations of the Chassigny meteorite have been previously reported by Floran et al. (1978), Johnson et al. (1991), Wadhwa and Crozaz (1995), Varela et al. (2000), and others. Consistent with the observations of these workers, cumulus minerals within the Chassigny dunite consist of olivine and Cr-rich spinel. Pyroxene, maskelynite, apatite, ilmenite, and sulfides occur in the regions interstitial to the cumulus grains. Within any individual interstitial region analyzed, more than one patch of maskelynite may exist. Apatite occurs as subhedral prismatic crystals with aspect ratios of about 10:1 or less. It is hosted only by maskelynite; multiple grains can be found within single patches of maskelynite (e.g., Fig. 1.1a).

As has been reported previously (e.g., Floran et al., 1978; Johnson et al., 1991), the cumulus olivine grains contain large polyphase melt inclusions (up to 200 μm in diameter) containing a mineral assemblage that is slightly different from that of the interstitial regions, most notably, one that includes the volatile-bearing minerals, kaersutite and Ti-biotite. Maskelynite is volumetrically dominant in the melt inclusions. More than one type of maskelynite patch is found in the melt inclusions, some with subhedral outlines and others as anhedral patches. Melt inclusion apatite is found as subhedral prismatic crystals (10-20 □m long) with aspect ratios of about 10:1 or less (Fig. 1.1b) and is hosted primarily by maskelynite. Unlike in the interstitial regions, however, apatite is also hosted by pyroxene.

1.3.2. Compositional results

1.3.2.1. Maskelynite

Electron microprobe analysis conducted on glass and glassy material with weak birefringence in the interstitial regions and melt inclusions indicates that most of the glass has feldspar stoichiometry (Table 1.1). In view of its stoichiometry and hence, its non-liquid-like composition, this glass is likely maskelynite (Milton and Decarli, 1963). The maskelynite of the intercumulus (interstitial) regions is of variable composition (Fig. 1.2) ranging from albitic plagioclase to K-rich alkali feldspar; most show significant ternary component. Glass of plagioclase composition is found primarily as either the sole feldspar glass or coexisting with alkali feldspar glass (referred to here as alkali maskelynite). In some interstitial regions there is more than one compositionally distinct type of maskelynite in discrete patches. Where this is found, the maskelynite compositions tend to vary linearly as if reflecting varying extents of intergrowth of an endmember plagioclase and endmember alkali feldspar before shock vitrification. Silica glass is also found and occurs as anhedral patches within the maskelynite and alkali maskelynite patches. No rhyolite composition glass was detected in these interstitial areas.

Analysis of melt inclusion maskelynite also shows varied chemistries ranging from rare intermediate plagioclase to K-rich alkali feldspar (Fig. 1.2), and all show significantly less ternary component than that of the intercumulus (interstitial) regions. Co-existing anhedral maskelynite and subhedral maskelynite have distinct compositions. Maskelynites with the highest An content are most commonly subhedral. Maskelynite with the lowest An content (i.e., albite) is found exclusively as anhedral patches. More than one compositionally distinct alkali maskelynite patch is commonly observed. These have compositions that are linear combinations of albite and highly potassic alkali feldspar, and they also commonly have measurable Cl contents as reported by Varela et al. (2000). Rhyolitic glass [with compositions comparable to those of Johnson et al. (1991)] is present but much less abundant than the feldspar glass, and it is found primarily in very thin anhedral patches bordering the more abundant maskelynite and alkali maskelynite. This rhyolite glass is so volumetrically limited that EMP analyses commonly show overlap with neighboring maskelynite. Apatite is found in maskelynite and alkali maskelynite of all compositions.

1.3.2.2. Apatite

Microprobe analyses of apatite are given in Table 1.2 along with their respective structural formulae based on 13 anions. As seen in Figure 1.3, the Chassigny meteorite contains two chemically distinct populations of apatite. The melt-inclusion apatite is exclusively fluor-rich apatite (ranging from 92-76 mole percent F in the X-site), while that found in the interstitial maskelynite and alkali maskelynite is a chlor-fluorapatite (ranging from 60-33 mole percent F in the X-site). Both apatite populations have very low computed hydroxyl content (ranging from 0-12 mole percent OH^- in the X-site).

Within the melt inclusions, there is no systematic difference in volatile content among apatites included in pyroxene, maskelynite, alkali maskelynite, and maskelynite/rhyolitic glass mixtures. Similarly, volatile contents of apatite in the interstitial maskelynite and alkali maskelynite show no correlation with glass composition.

1.4. Discussion

Assessment of the evolutionary history of magmatic volatiles during the late-stage crystallization of the Chassigny meteorite is a two-part effort involving interpretation of the history, first of the host minerals, and then of the included apatite.

1.4.1. Interstitial apatite-hosting maskelynite

Figure 1.4 shows the compositions of apatite-hosting interstitial maskelynite and alkali maskelynite (using the values corrected for Na-loss). The strongly ternary nature of these maskelynites and the relatively low An content of the most calcic (highest temperature) maskelynite are typical characteristics of feldspar evolution during high temperature crystallization, as seen in trachytes, syenites and rhyolites with low bulk water contents on Earth (Carmichael, 1965; Nash et al., 1969). Such feldspar evolution paths have been discussed in detail by Nekvasil (e.g., Nekvasil, 1990; Nekvasil, 1992a; Nekvasil, 1992b; Nekvasil, 1994). Her results were used to construct a reasonable feldspar evolutionary path for the interstitial maskelynite (Fig. 1.4) in which early ternary plagioclase crystallizes until the feldspar solvus is intersected (shown in Fig. 1.4 at ~ 850°C). Increasing dissolved volatile load through crystallization of volatile-free phases induces continual expansion of the solvus sections as the solidus temperature is depressed, resulting in a decrease in Or component and an increase in Ab component in plagioclase and potassium enrichment of alkali feldspar. Such a path is supported by the

two equilibrium maskelynite-alkali maskelynite pairs found within one interstitial pocket. Geothermometry on these two pairs was conducted using the Lindsley and Nekvasil (1989) ternary feldspar solution model and the SOLVCALC software of Wen and Nekvasil (1994). The results indicated that (i) each set represented an equilibrium pair and (ii) the higher temperature pair crystallized at 800°C (±15°C) and the lower at 713°C at 5 kbar (Fig. 1.4). This pressure was chosen for comparative reasons as it is a pressure of reliable data calibration of the thermodynamic model. Furthermore, the results of Nekvasil et al. (2007) suggest that crystallization of Chassigny occurred above 4.3 kbar.

Of potential additional importance are the maskelynite and alkali maskelynite compositions that deviate from the path shown in Figure 1.4. The ternary compositions lying within the solvus are inconsistent with any path envisioned in that they suggest high-temperature anorthoclase crystallization followed by more anorthitic feldspar at lower temperatures. They can, however, be readily explained as a result of overlap of fine intergrowths of an equilibrium feldspar pair since they lie on the tie-lines connecting equilibrium feldspar pairs. Ab-rich maskelynites with low ternary content found in some interstitial regions show marked similarities to those in the melt inclusions (Fig. 1.2), suggesting that at least some interstitial pockets saw crystallization conditions similar to those within the melt inclusions.

1.4.2. Apatite-hosting maskelynite in melt inclusions

Figure 1.5 shows the compositions of maskelynite and alkali maskelynite from melt inclusions (using the values adjusted for Na-loss). These compositions record much lower crystallization temperatures than those of most of the interstitial regions, with the solvus likely intersected over 200°C lower (as indicated by the low ternary component of the maskelynites). A maskelynite/alkali maskelynite equilibrium pair observed within one inclusion yielded a temperature of 560°C from two-feldspar geothermometry. At this temperature the compositions of this pair may still reflect magmatic crystallization, but only if there was a significant suppression of the solidus temperature. This speaks not only to high volatile load but also to elevated pressure in order to retain these volatiles in the melt.

Of particular interest is the common occurrence in the melt inclusions of maskelynite and alkali maskelynite with almost binary albitic plagioclase and potassic

alkali feldspar compositions. The compositions yield very low equilibration temperatures (Fig. 1.5), temperatures that are suggestive of hydrothermal precipitation or volatile-assisted re-equilibration. The numerous maskelynite compositions lying between the most albitic and potassic compositions may reflect fine intergrowths of albite and orthoclase or varied stages of fluid-assisted re-equilibration of feldspar compositions to lower temperatures.

Crystallization of feldspar to the solidus temperature and its compositional modification in the hydrothermal (subsolidus) regime may at first glance seem inconsistent with the presence of rhyolite glass in the melt inclusions. If the rhyolite glass was produced by rapid quench of glass residual to crystallization, then the melt inclusion could not have seen continued feldspar crystallization into the hydrothermal regime, that is, past the point of crystallization of the lowest temperature liquid. This apparent inconsistency is resolved, however, if the rhyolite glass was produced by shocking of a fine-grained rhyolitic intergrowth of two feldspars and quartz at the same time that the maskelynite was formed. That a fine-grained matrix of quartz and feldspars can vitrify to rhyolite glass during shock is supported by observations of natural impact glasses from structures such as the El'gygytgyn impact structure, Russia (Gurov and Koeberl, 2004). The minimum pressure required for producing such glasses is in keeping with the shock pressure estimated for Chassigny [i.e., 35 GPa (Nyquist et al., 2001)].

1.4.3. Volatile behavior in melt inclusions

The presence of volatile-bearing kaersutite, biotite, fluorapatite, and maskelynite (Boctor et al., 2003; e.g., Floran et al., 1978; Johnson et al., 1991; McCubbin and Nekvasil, 2007; McCubbin et al., 2006a, 2007; Watson et al., 1994) all attest to the presence of the dissolved volatiles F, Cl, and water in the trapped melt inclusions. During typical closed system (with respect to volatiles) crystallization, these volatiles will increase in the melt until a fluid phase exsolves.

Fluid exsolving from a melt containing F, Cl, and H_2O will have a high ratio of (H_2O+Cl):F because of the recognized strong partitioning of F into the melt (e.g., Candela, 1986b; Holland, 1972; Kilinc and Burnham, 1972). This fluid must have contained sufficient Cl in addition to water to facilitate the chemical re-equilibration of the feldspars under subsolidus conditions. This is supported by the occasional occurrence

of high chlorine contents [up to 1.20 wt% Cl; (McCubbin and Nekvasil, 2007; McCubbin et al., 2007a; Varela et al., 2000)] and water contents [~0.3 wt% H_2O; (Boctor et al., 2003)] in maskelynite within the melt inclusions. These high chlorine and water contents measured within the stoichiometric feldspar glass may have arisen from shock vitrification of fluid-inclusion bearing, low-temperature feldspar. Less well constrained are the magmatic water contents. None of the "hydrous" minerals of the MI - kaersutite, Ti-biotite, or fluor-apatite - requires much dissolved water in the melt. Importantly, however, this does not imply low water contents of the trapped melt. Even in the presence of over 1 wt% dissolved water, kaersutite and Ti-biotite will not contain much water because of coupled (Ti^{4+}+O^{2-}) substitution mechanisms (McCubbin et al., 2006b, c; Popp and Bryndzia, 1992; Popp et al., 2006; Popp et al., 1995a, b; Righter et al., 2002). Similarly, even in the presence of an aqueous fluid, the presence of as little as 500 ppm F in the fluid at the feldspar crystallization temperatures produces apatite with less than 10 mol% hydroxylapatite component (Zhu and Sverjensky, 1991), thereby rendering interpretation of magmatic H_2O contents from such apatite impossible.

Regardless of the H_2O/Cl ratio of the melt inclusion fluid or melt, under a wide range of pressures and at the temperatures obtained from two-feldspar geothermometry, fluorapatite of the compositional range observed in the Chassigny melt inclusions would form (Zhu and Sverjensky, 1991). Crystallization of F-bearing phases would result in slightly higher Cl contents of the evolving residual liquids, but this change is readily accommodated by the compositional range in volatile contents of the apatite observed (Fig. 1.3).

If fluid remained available to be involved in subsolidus re-equilibration of feldspars as happens in pegmatitic systems, the olivine must have had sufficient tensile strength to retain the fluids at the overpressures that arose during fluid exsolution at least at depth. However, once the dunite was brought up to shallow levels [presumably as an entrained nodule in later magma (Nekvasil et al., 2007)] and subjected to meteorite impact, rupture of the melt inclusions and fluid loss was inevitable. The radial and concentric fractures observed in the cumulus olivine indicate that such rupture was pervasive.

1.4.4. Volatile behavior in the interstitial regions

Open-system behavior with respect to volatiles in the regions interstitial to the cumulus phases likely consists of a combination of volatile loss upon exsolution and upward migration of fluid, and volatile gain by ingress of fluids from deeper and hotter portions of the underlying magma plumbing system. Volatile loss alone cannot readily explain the formation of the Cl-rich apatite in the interstitial regions since the partitioning of F into the melt rather than the fluid would ensure precipitation of F-rich apatite if the fluid simply left the interstitial region. However, migrating fluids rising from hotter, deeper levels of the magmatic system would be more Cl-rich and H_2O-poor (Webster and Rebbert, 1998). Equilibration of such a fluid with the interstitial melt would involve loss of water to the fluid and gain of chlorine by the melt. Any pre-existing apatite would react with this fluid and become more Cl-rich, and any subsequent crystallization of apatite would also result in more Cl-rich apatite.

The differences in apatite volatile chemistry between the melt inclusions and the interstitial regions support the possibility that a Cl-rich fluid migrated into the interstitial regions of the Chassigny meteorite. Figure 1.6 shows the compositions of the apatite in both the interstitial and melt inclusion environments. The interstitial apatite compositions lie at much higher HCl/HF fugacity ratios than those of the melt inclusion apatites. However, it is only through assessment of temperature constraints that this observation can be used to support the addition of a Cl-rich fluid into the interstitial regions. The chlorinity of a fluid can decrease during cooling and crystallization [as indicated by the arrows in Figure 1.6 (Meurer and Boudreau, 1996; Zhu and Sverjensky, 1991)]. In fact, the lower temperatures of the melt inclusion feldspars relative to the interstitial feldspars seem at first pass to be consistent with a crystallization-induced difference in chlorinity, rather than necessitating fluid addition. However, apatite in the melt inclusions is found in pyroxene in addition to maskelynite and alkali maskelynite. The minimum pyroxene crystallization temperatures within the interstitial regions are similar to those of subcalcic augite in the melt inclusions [i.e., >1100°C; (Nekvasil et al., 2007)]. As seen in Figure 1.6, there is no overlap of the high-temperature melt-inclusion apatite and the interstitial apatite. Figure 1.6 indicates that the observed difference in HCl/HF fugacity ratios could arise from either fluid loss from the melt inclusions while fluid is retained within the

interstitial region – an unlikely scenario - or from the addition of a Cl-rich fluid only to the interstitial regions.

If brine (hydrosaline fluid) was introduced into the accumulating olivine pile from deeper levels, a further indication of the nature of this fluid may be preserved in the REE signature of the minerals that reacted with that fluid and in the REE characteristics of minerals crystallizing after the melt equilibrated with the entering fluid. Wadhwa and Crozaz (1995) noted LREE-enrichment in pyroxene rims, and LREE-enriched maskelynite and apatite in the interstitial regions of Chassigny. Although these workers attributed this to fractionation of a LREE-enriched source, might it have been induced instead by the introduction of a Cl-rich brine? Stalder et al. (1998) determined experimentally that high-temperature fluids equilibrating with pyroxene become LREE-enriched. Similarly, observations of Lieftink et al. (1994) showed that fluid interaction with apatite causes selective LREE-enrichment (specifically of La and Ce) of the fluid. Therefore, any migrating fluid that equilibrated with pyroxene and apatite at deeper levels would likely be LREE-enriched. High chlorinity would cause overall enhancement of REE partitioning into the fluid (e.g., Bai and van Groos, 1999; Candela and Piccoli, 1995; Webster and Rebbert, 1998) and thus, higher LREE loads in the fluid. Equilibration of this fluid with interstitial melt, pyroxenes, and early-formed apatite at the level of the Chassigny cumulates would decrease the chlorinity of the fluid, increase its water content, and decrease its LREE load, while increasing both the chlorinity and LREE load of the melt. In spite of the preferential incorporation of HREE in pyroxene, the higher LREE load of the melt would be manifested by the growth of relatively LREE-enriched rims in pyroxene relative to the cores, as well as later-formed LREE-enriched feldspar and apatite.

The compositions of maskelynite and alkali maskelynite within the interstitial regions also support the possibility of ingress of a Cl-rich fluid into the interstitial regions. Equilibration of such a fluid with the interstitial melt would involve loss of water from the melt to the fluid. Migration of this fluid away from the interstitial regions would result in progressive dehydration of the interstitial melt of the Chassigny cumulate horizon. Dehydration in the interstitial regions would allow feldspar crystallization at higher temperature than in the melt inclusions by diminishing the extent of destabilization

of feldspar components by dissolved water in the melt (e.g., Burnham and Nekvasil, 1986; Zeng and Nekvasil, 1996; Zeng et al., 2000). The higher-temperature feldspar of the interstitial regions would have more ternary character, just as observed. Furthermore, there would be less fluid retained in this open-system environment for re-equilibration of the ternary feldspar to lower-temperature assemblages in the hydrothermal regime. The inferred dehydration is also consistent with the absence of biotite and kaersutite in the interstitial assemblages.

The observations that (i) the evolutionary path of the interstitial feldspars differs from that of the melt inclusion feldspars, (ii) the apatite hosted by maskelynite in the interstitial regions differs from that of the melt inclusions, (iii) the high-temperature pyroxene crystallization temperatures are similar in both regimes and, (iv) kaersutite and Ti-biotite (that likely crystallized after subcalcic augite) occur in the melt inclusions (Nekvasil et al., 2007), but not in the interstitial regions, all put the timing of this ingress of a Cl-rich fluid prior to the crystallization of Ti- biotite, kaersutite, and feldspar, after the crystallization of at least some subcalcic augite, and either during or just after the formation of the first apatite.

1.4.5 Brine exsolution and brine/melt interaction in cumulate rocks on Earth

Terrestrial cumulates may provide further insight into the interaction of melt in small interstitial pockets with a migrating fluid. The Bushveld intrusion shows a variation in apatite chemistry in the Upper Zone which supports the premise that a Cl-rich fluid can exsolve at high temperatures from basaltic magma interstitial to cumulus olivine and migrate from the cumulus pile. Willmore et al. (2000) concluded that the interstitial magma from the Upper Zone of the Bushveld was fluid-saturated by the time apatite crystallized (>1000°C) and that it was the loss of this Cl-rich fluid that resulted in elevated F/Cl ratios of the apatite that crystallized from the fluid-depleted interstitial regions.

For the Stillwater Complex, Meurer and Boudreau (1996) noted increasing Cl:F contents of interstitial apatite up-section in the olivine-bearing horizons in the absence of any correlatable change in olivine composition. They noted that this cannot be ascribed to crystallization of amphibole or biotite and F-partitioning into these phases because these phases are not present interstitially. This reasoning is also applicable to the interstitial

regions of the Chassigny dunite. Boudreau and McCallum (1989) and Meurer and Boudreau (1996) suggested instead that an exsolved Cl-rich fluid migrating upward through a partially solidified crystal pile can cause an upward enrichment in Cl in the interstitial liquid and hence apatite. We propose a similar process here for Chassigny.

1.5. Acknowledgments

We thank Guy Consolmagno of the Vatican Observatory and Robert Dodd for providing us with thin sections of the Chassigny meteorite. We also thank Dr. Alexander Smirnov for assistance with BSE image acquisition. Additionally we thank Dr. Donald H. Lindsley, Dr. Alan Boudreau, Dr. Molly McCanta, and Dr. Rhian Jones for thorough and insightful reviews of this paper. We also thank Dr. Rhian Jones and Dr. Robert Dymek for the careful editorial handling of this paper. Financial support for this work was provided by NASA grant NNG04GM79G from the Mars Fundamental Research Program.

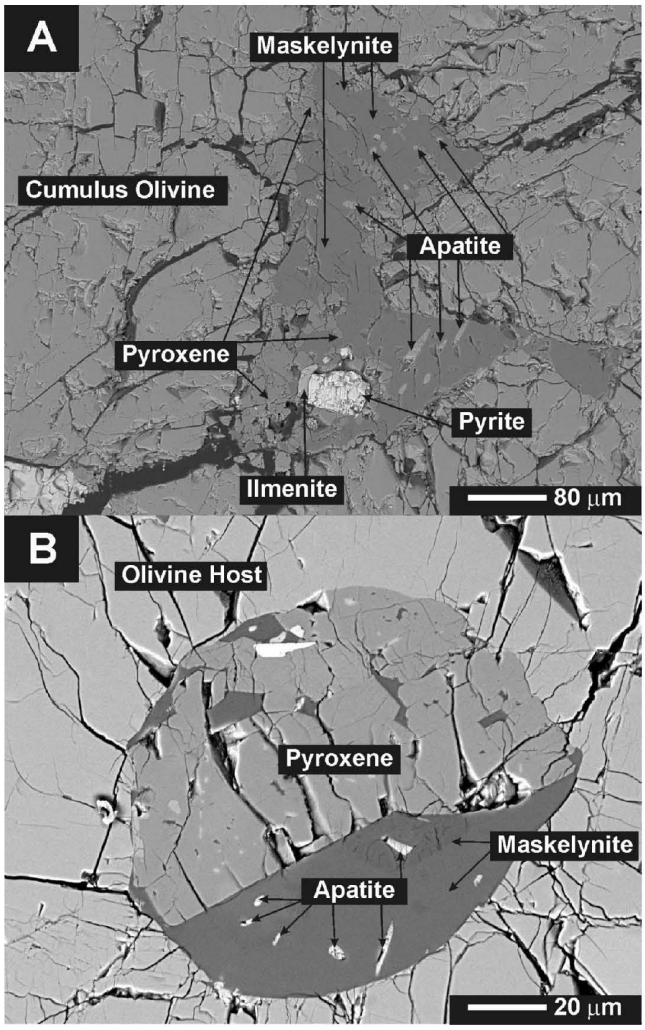

Figure 1.1. (a) Back-scattered electron image of cumulus olivine with interstitial apatite, maskelynite, pyroxene, pyrite, and ilmenite. (b) Back-scattered electron image of an olivine-hosted melt inclusion containing apatite, maskelynite, and pyroxene.

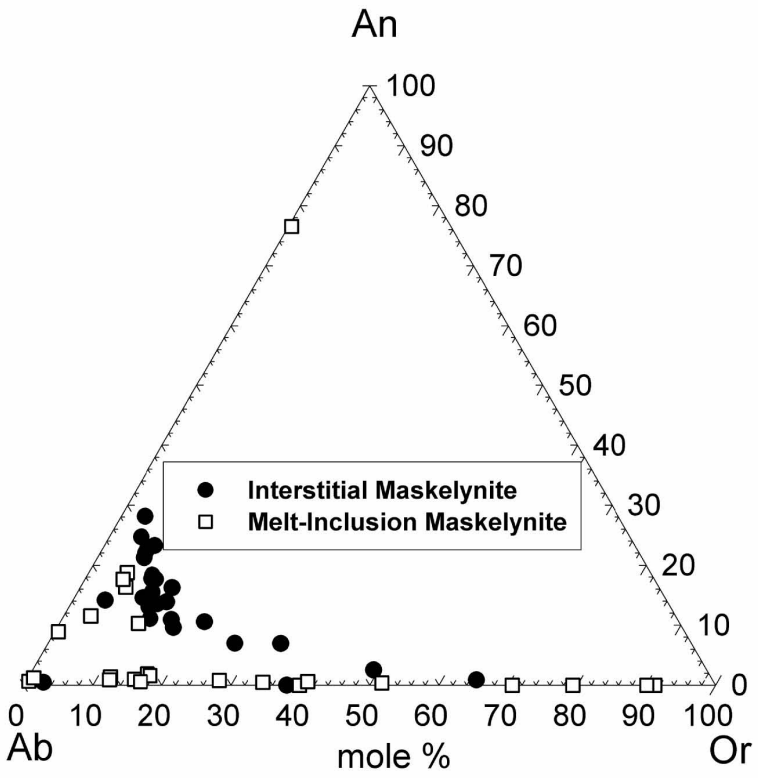

Figure 1.2. Ternary plot of normalized normative feldspar components of maskelynite and alkali maskelynite interstitial to the cumulus phases (solid circles) and within polyphase melt inclusions (open squares). The values used were corrected for Na-loss.

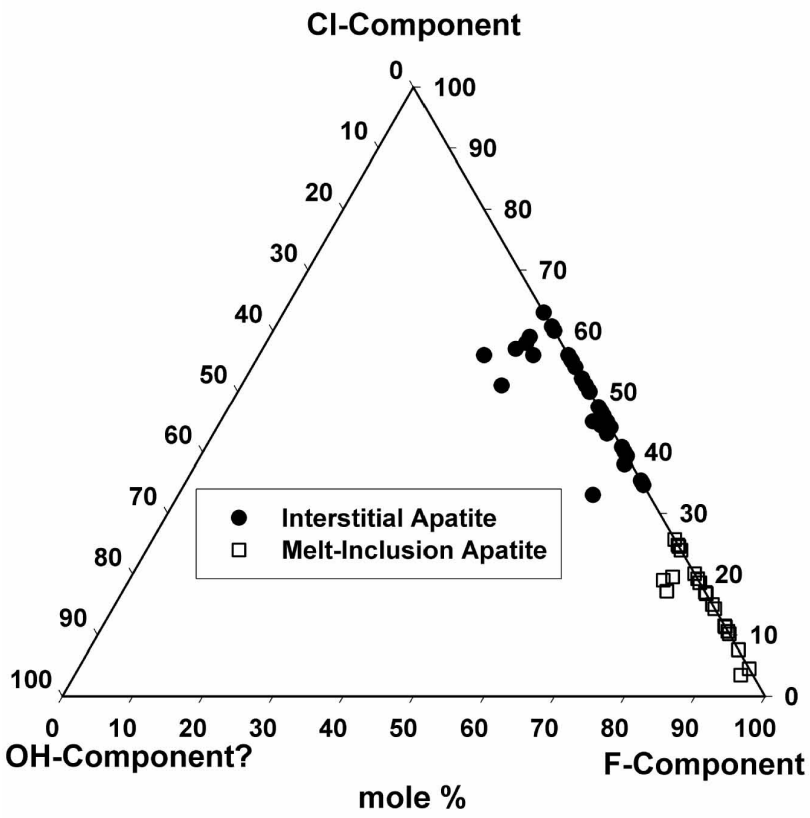

Figure 1.3. Ternary plot of the X-site components of interstitial (filled circles) and melt-inclusion apatite (open squares) within the Chassigny meteorite. Analyses for which (F + Cl) > 1 were plotted as OH^--free apatite with a F:Cl ratio equal to that of the analysis.

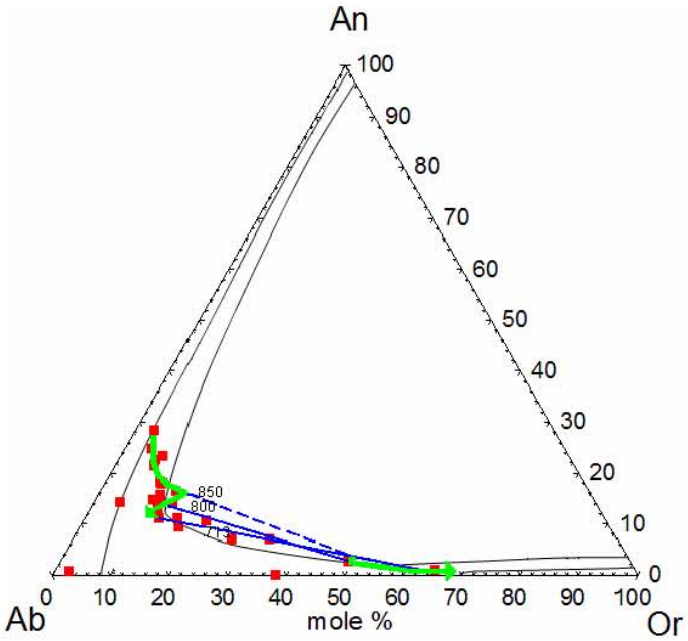

Figure 1.4. Ternary plot of interstitial maskelynite and alkali maskelynite compositions (red circles). Isothermal ternary feldspar solvus sections calculated using SOLVCALC (Wen and Nekvasil, 1994) and the thermodynamic model of Nekvasil and Lindsley (1990) are shown for 800°C and 600°C at 5 kbar. This model was also used to compute the equilibrium temperatures of associated maskelynites and alkali maskelynites. The solid blue tielines show two such compositional pairs and their calculated equilibrium temperatures. The dashed blue tieline shows the composition of the associated alkali maskelynite if intersection of the solvus occurred at 850°C. The green curves indicate plagioclase and alkali feldspar compositional evolution with dropping temperature based on geothermometry and the general feldspar evolutionary paths discussed by (Nekvasil, 1992a; Nekvasil, 1994; e.g., Nekvasil and Lindsley, 1990). (Arrows point in the down-temperature direction.) Once the solvus is intersected by the feldspar solidus, plagioclase becomes both Ab-enriched and Or-depleted with dropping temperature; alkali feldspar becomes Or-enriched.

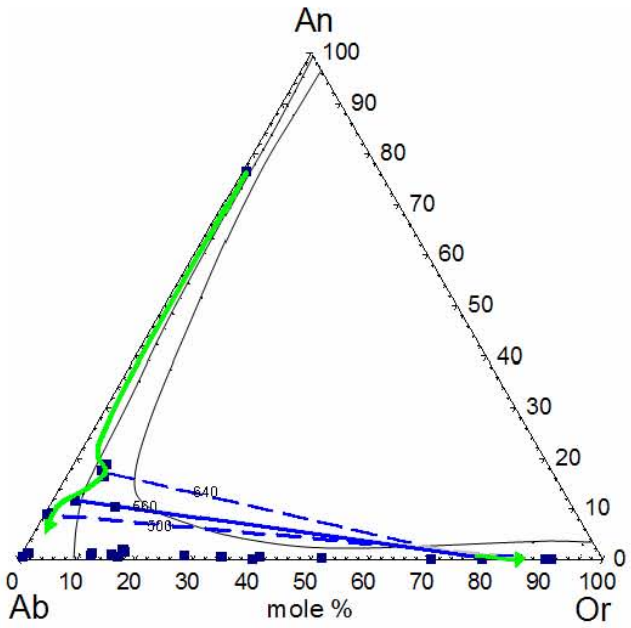

Figure 1.5. Ternary plot of melt inclusion maskelynite and alkali maskelynite compositions (blue squares). Isothermal ternary feldspar solvus sections calculated using SOLVCALC (Wen and Nekvasil, 1994) and the thermodynamic model of Nekvasil and Lindsley (1990) are shown for 800°C and 600°C at 5 kbar. This model was also used to compute the temperature of the one compositional pair found (linked by the solid blue tieline) that, based on geothermometry, appears to be in equilibrium. The higher temperature dashed tieline shows the composition of the associated alkali maskelynite if intersection of the solvus occurred at 640°C. The lower temperature dashed tieline indicates the composition of the alkali feldspar that would co-exist with the observed plagioclase at 500°C. The green line indicates a reasonable feldspar compositional path with dropping temperature based on the compositions analyzed. Further details of such "low"-temperature feldspar evolutionary paths are given in (Nekvasil, 1992a; Nekvasil, 1994; e.g., Nekvasil and Lindsley, 1990) The wide range of binary and nearly binary Ab-Or solid solution may represent micro-domains of highly albitic and potassic feldspar formed at even lower temperature during re-equilibration by a Cl-rich fluid under subsolidus conditions.

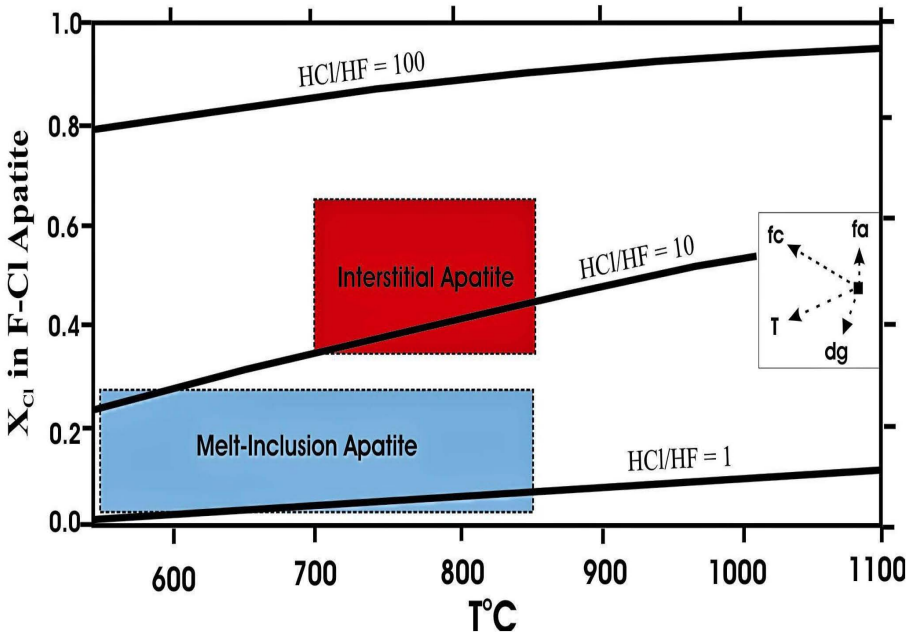

Figure 1.6. Variation in mole fraction of Cl in the X-site of F-Cl apatite as a function of the fugacity ratio of HCl to HF in a coexisting fluid and temperature, as adapted by Meurer and Boudreau (1996). Apatite from this study is plotted within respective boxes of observed Cl-component and possible temperatures of crystallization based on feldspar and pyroxene thermometry. The inset box shows possible changes in apatite Cl abundance for specific processes (fa) – fluid addition; (fc) – fractional crystallization; (T) – decreasing temperature; and (dg) – degassing adapted from Meurer and Boudreau (1996).

Table 1.1. Electron Microprobe analyses of maskelynites (shocked feldspars) from the Chassigny Meteorite

Oxide	Interstitial	Interstitial	Interstitial	Melt Inclusion	Melt Inclusion	Melt Inclusion
SiO_2	66.1 (5)	64.6 (5)	63.2 (4)	47.1 (3)	67.7 (5)	64.7 (5)
TiO_2	0.11 (2)	0.13 (2)	0.07 (2)	0.05 (2)	0.12 (2)	0.05 (2)
Al_2O_3	22.7 (1)	18.4 (1)	23.0 (1)	32.7 (2)	19.3 (1)	22.4 (1)
FeO^T	0.33 (3)	0.20 (3)	0.24 (3)	0.41 (3)	0.35 (3)	0.30 (3)
MnO	0.00	0.01 (1)	0.00	0.01 (1)	0.03 (2)	0.00
MgO	0.02 (1)	0.03 (1)	0.05 (1)	0.29 (1)	0.02 (1)	0.03 (1)
CaO	3.09 (5)	0.57 (2)	4.53 (5)	15.2 (1)	0.12 (1)	4.06 (5)
Na_2O	7.82 (9)	4.82 (7)	7.76 (9)	2.22 (4)	5.16 (7)	7.47 (9)
Na_2O*	8.60*	5.25*	8.28*	2.46*	5.58*	8.68*
K_2O	2.49 (4)	8.17 (8)	1.19 (3)	0.08 (1)	9.10 (9)	0.97 (3)
P_2O_5	0.08 (2)	0.03 (2)	0.08 (2)	0.28 (2)	0.03 (2)	0.12 (2)
Total	102.74	96.96	100.12	98.34	101.93	100.10
Structural Formulae based on 8 Oxygens						
Si	2.84	2.99	2.79	2.20	2.99	2.83
Ti	0.00	0.00	0.00	0.00	0.00	0.00
Al	1.15	1.00	1.19	1.79	1.00	1.15
Fe^T	0.01	0.01	0.01	0.02	0.01	0.01
Mn	0.00	0.00	0.00	0.00	0.00	0.00
Mg	0.00	0.00	0.00	0.02	0.00	0.00
Ca	0.14	0.03	0.21	0.76	0.01	0.19
Na	0.65	0.43	0.67	0.20	0.44	0.64
Na*	0.72	0.47	0.71	0.22	0.48	0.74
K	0.14	0.48	0.07	0.00	0.51	0.05
P	0.00	0.00	0.00	0.01	0.00	0.00
Cation Sum	4.94	4.94	4.96	5.01	4.96	4.89
Cation Sum*	5.01	4.98	5.00	5.03	5.00	4.99
Phase Comp.*	$An_{14}Ab_{72}Or_{14}$	$An_3Ab_{48}Or_{49}$	$An_{21}Ab_{72}Or_7$	$An_{77}Ab_{23}Or_0$	$An_0Ab_{48}Or_{52}$	$An_{19}Ab_{76}Or_5$

Components: Ab (Albite); An (Anorthite); Or (Sanidine)

*Represents analysis that was corrected for excess quartz (qz) and corundum (co) by addition of Na until Qz or Co was no longer present in the CIPW norm.

Numbers inside of parentheses correspond to absolute uncertainties for each measurement.

Table 1.2. Electron Microprobe analyses of apatite from the Chassigny Meteorite

Oxide	Melt Inclusion*	Melt Inclusion*	Interstitial*	Interstitial*	Interstitial*
SiO_2	0.00	0.00	0.37	0.42	0.41
Al_2O_3	0.00	0.33	0.00	0.00	0.00
FeO^T	0.77	0.48	0.53	0.56	0.33
MnO	0.07	0.10	0.04	0.06	0.04
MgO	0.01	0.00	0.06	0.08	0.05
CaO	54.6	54.7	53.7	53.9	54.6
Na_2O	0.10	0.00	0.09	0.10	0.19
K_2O	0.05	0.00	0.06	0.06	0.04
P_2O_5	41.8	41.6	41.2	41.0	40.8
F	3.45	2.84	1.90	1.33	1.98
Cl	0.82	1.5	3.64	3.92	3.13
-O = F + Cl	1.64	1.53	1.62	1.44	1.54
Total	100.03	100.02	99.97	99.99	100.03
		Structural Formulae Based on 13 Anions			
Si	0.00	0.00	0.03	0.04	0.03
Al	0.00	0.03	0.00	0.00	0.00
Fe^T	0.05	0.03	0.04	0.04	0.02
Mn	0.00	0.01	0.01	0.00	0.00
Mg	0.00	0.00	0.01	0.01	0.01
Ca	4.95	4.96	4.92	4.94	5.01
Na	0.02	0.00	0.02	0.02	0.03
K	0.01	0.00	0.01	0.01	0.00
P	2.99	2.98	2.98	2.97	2.95
F	0.92	0.76	0.51	0.36	0.53
Cl	0.12	0.19	0.53	0.57	0.45
OH**	0.00	0.05	0.00	0.07	0.02
Cation Sum	8.02	8.01	8.02	8.03	8.05
Z-Site Sum	1.04	1.00	1.04	1.00	1.00

*Apatite analysis overlapped with another phase, so appropriate phase subtraction was performed using an analysis of the overlapping phase

**OH calculated by assuming F + Cl + OH = 1

Synthesis and characterization of low-OH^- fluor-chlorapatite: A single crystal XRD and NMR spectroscopic study

Francis M. McCubbin[1], Hanna Nekvasil[1], Harris E. Mason[1], Hyunsoo Park[2], Brian L. Phillips[1], John B. Parise[1, 2], and Donald H. Lindsley[1]

[1]Department of Geosciences, Stony Brook University, Stony Brook New York, 11794-2100, U.S.A.
[2]Department of Chemistry, Stony Brook University, Stony Brook New York, 11794-3400, U.S.A.

Manuscript published in American Mineralogist, January, 2008

2.1. Introduction

The mineral apatite is of importance to a wide variety of fields, from earth science to life science, material science, and planetary science (e.g. Hughes and Rakovan, 2002). It is the major source of phosphorus on Earth, and its uses range from fertilizers to detergents to insecticides. It is the main constituent of human bone and plays an important part in regulating metabolic functions in the body. Apatite is found in sedimentary, igneous, and metamorphic rocks, and it is an important sink of rare earth elements, which are of primary importance for petrogenetic studies. Also, its ability to accommodate the radioisotopes used for age determinations makes it of major importance to geochronological studies of rocks.

Geologically occurring apatite, most commonly $Ca_5(PO_4)_3[F,Cl,OH]$, generally has either a hexagonal structure with space group $P6_3/m$, or a monoclinic structure with space group $P2_1/b$. Apatite is represented by the structural formula $A[1]_2A[2]_3(BO_4)_3X$ [adopted from White and Dong (2003)] where A[1] and [2] represent the Ca-sites, B the phosphorus site, and X the typically monovalent anion site. The X-site in apatite provides a basis for solid solution with three primary endmember components, fluorapatite $[Ca_5(PO_4)_3F]$, chlorapatite $[Ca_5(PO_4)_3Cl]$, and hydroxylapatite $[Ca_5(PO_4)_3OH]$. The

structures of these endmembers have been well studied [see summary of Hughes et al. (1989)]. The atomic arrangements of the three apatite endmembers differ principally in the positions of F^-, Cl^-, and OH^- in the [00z] anion positions. Binary solid solutions of either F^- and OH^- or Cl^- and OH^- are common (Tacker and Stormer, 1989), although not much is known regarding F^- and Cl^- binary solutions. Ternary solution of all three X-site anions in apatite does occur (e.g. Hughes et al., 1990; Piccoli and Candela, 2002), however, ternary solution requires that the [00z] columns accommodate a combination of the three different anions. This accommodation requires a structural response because of interactions among the column anions (Hughes and Rakovan, 2002). Based on a variety of studies it was concluded that miscibility of F^-, Cl^-, and OH^- in hexagonal ternary apatite results from a Markovian sequence of anions in which the occupant of a given position is dependent on the occupant of the adjacent position (Hughes and Rakovan, 2002). This accommodates the three anions in a single column without vacancies. The shift in anionic positions induced by anion mixing also affects the cation positions. It has been proposed that anionic mixing among the three X-site anions is coupled by a splitting of the single Ca[2] site into two sites (Sudarsanan and Young, 1969). Such structural adjustments have been summarized by Hughes et al. (1990). These workers, however, also reported a monoclinic variant of the ternary apatite structure in which a reduction in symmetry results from ordering in the anionic columns. As acknowledged by Hughes and Rakovan (2002) however, column anion interactions may inhibit binary solution of fluorapatite and chlorapatite because the position of the fluorine atoms, [00¼] and [00¾], deviates from that of chlorine by about 1.2 Å because of differences in ionic radii (Hughes and Rakovan, 2002). In fact, Hughes et al. (1990) suggested that in natural apatites OH^- may be an essential component in stabilizing fluorapatite-chlorapatite solid solutions.

There is some natural evidence for the stability of OH^--poor, fluor-chlorapatites. Boudreau et al. (1995) compiled extensive data on channel anion compositions of natural apatites from a variety of layered intrusions. This compilation showed the predominance of OH^--rich apatite in natural layered intrusions. However, several intrusions, for example Stillwater and Bushveld (below the PGE zones), contain Cl-rich, OH^--poor apatite. Additionally, Martian meteorites, specifically Chassigny and Nakhla, contain apatite with

reported analyses indicating low OH^- contents (e.g. Bunch and Reid, 1975; McCubbin et al., 2006a; McCubbin et al., 2007a). Lastly, evaluation of lunar apatite data from Apollo 14 basalts (Taylor et al., 2004) and Apollo 14 soils (Jolliff et al., 1993) also shows the presence of fluor-chlorapatites with computed low OH^- contents.

There is an apparent inconsistency between the structural considerations listed above and the reports of natural OH^--poor apatites. This questions the reliability of either the inferred structural characteristics of apatite or the reported analytical data. This work is aimed at evaluating this inconsistency by determining whether or not there is a previously unreported structural adjustment in OH^--poor apatite that facilitates the existence of long-range F^--Cl^- neighboring in apatite.

2.2. Analytical/Experimental Methods

2.2.1. Apatite Synthesis

The composition of synthetic apatite selected for use in this study is $Ca_5(PO_4)_3(F_{0.5}Cl_{0.5})$. This composition was achieved by mixing powdered $Ca_3(PO_4)_2$, CaF_2, and $CaCl_2$. Due to the hygroscopic nature of $CaCl_2$, steps were taken to limit, as much as possible, the amount of H_2O in the starting material. First, the mix was dried in a platinum crucible overnight at 500°C to drive off absorbed H_2O. Next, the powder was loaded into a platinum capsule and inserted in a silica glass tube, from which a capillary was pulled. The tube was then attached to a vacuum pump and placed in a pot furnace at 800°C to drive off structurally-bound H_2O. The tube was left under a pumping vacuum for 24 hours at 800°C to maximize H_2O loss. Subsequently, the evacuated silica glass tube was sealed and placed in a horizontal tube furnace at 900°C. Synthesis of apatite in vacuum was done in order to avoid the complications of O^{2-} substitution into the apatite X-site (Pan and Fleet, 2002). The synthesis duration was 14 days. This period was found to be sufficient for growing crystals large enough for single crystal diffraction at a third generation synchrotron source.

2.2.2. EPMA Analysis

Electron microprobe analyses (EPMA) of the synthetic apatite grains were performed using a Cameca Camebax electron microprobe equipped with four wavelength dispersive spectrometers, one of which was equipped with an OV-60 detector crystal necessary for obtaining accurate fluorine analyses. An accelerating voltage of 15 kV and

a nominal beam current of 10 nA were used during all analyses. Anorthite, apatite, barium apatite, and magnesium fluoride were used as standards for Ca, P, Cl, and F, respectively. The largest possible raster size was used to minimize unknown analytical problems that may occur during highly focused electron beam analyses. In order to avoid apparent anisotropic diffusion of fluorine and chlorine during EPMA analyses down the c-axis of apatite (Stormer et al., 1993), care was taken to measure down the a-axis whenever possible. Hydroxyl was not directly measured in this study; it was calculated assuming that only fluorine, chlorine, and hydroxyl populate the apatite X-site, and that the X-site sums to one when normalized to 13 anions.

2.2.3. X-ray Powder Diffraction

X-ray powder diffraction analysis was performed on a Scintag PAD X diffractometer using Cu-Kα radiation. The synthesized powder was prepared as a smear mount on a glass slide and analyzed at 40kV and 25mA using a continuous scanning procedure with a scan rate of 0.75° (2θ)/minute over the range 5°-90° (2θ). The resulting X-ray pattern was used to indicate sample purity and completeness of reaction.

2.2.4. Single crystal X-ray diffraction

Synchrotron X-ray data were collected in order to obtain a diffraction signal with sufficient peak-to-background discrimination to aid in the assignment of a correct symmetry (monoclinic vs. hexagonal) as well as to obtain precise positions of the anions along the *c* axis. Data collection and structure determination were carried out at 15-ID ChemMatCARS beamline at the Advanced Photon Source, Argonne National Laboratory. A small crystal of 0.03 x 0.03 x 0.03 mm^3 in dimension was selected and mounted on a glass fiber with Paratone oil. The data were collected at 100 K with wavelength of 0.4959(2) Å, exposure time of 1 s per frame, and a detector distance of 5.0 cm. A randomly oriented region of reciprocal space was examined to a resolution of 0.75 Å. Two major sections of frames were collected with a step size of 0.30° in ω and ϕ. The raw intensity data were collected and integrated with software packages SMART (2001) and SAINT (2002), then an empirical absorption correction was applied using SADABS (Sheldrick, 2001). The final unit cell parameters were determined from 1024 strong reflections after integration. The crystal structures were solved via the direct method and refined with the program SHELXTL (Sheldrick, 2000) assuming anisotropic

displacement parameters for all atoms except the hydroxyl O atom. Calcium and phosphorus atoms were located first, and the remaining atoms (O, Cl, F) were found from subsequent Fourier difference map synthesis.

2.2.5. NMR Spectroscopy

^{31}P Single-Pulse (SP) Magic Angle Spinning (MAS) Nuclear Magnetic Resonance (NMR), ^{19}F SP MAS NMR, ^{35}Cl SP MAS NMR, ^{31}Pmay ha Cross Polarization (CP)/MAS, $^{31}P\{^{19}F\}$ CP/MAS NMR and $^{19}F\{^{35}Cl\}$ Transfer of Population Double Resonance (TRAPDOR) NMR spectra of the synthetic apatite were collected on a 500 MHz Varian Infinity Plus spectrometer at operating frequencies of 499.78 MHz, 470.21 MHz, 204.32 MHz, and 48.97 MHz for ^{1}H, ^{19}F, ^{31}P, and ^{35}Cl respectively. For all experiments the samples were contained within 3.2 mm (o.d.) zirconium oxide rotors.

^{31}P SP MAS NMR spectra were collected at a spinning rate of 10 kHz with a 4 μs pulse and a 120 s pulse delay in order to ensure full spin lattice relaxation. $^{31}P\{^{1}H\}$ and $^{31}P\{^{19}F\}$ CP/MAS NMR spectra were collected using a radio frequency (rf) amplitude ramp for a variety of contact times and at a spinning rate of 5 kHz. All ^{31}P spectra were referenced to 85% phosphoric acid using hydroxylapatite as a secondary reference set to +2.65 ppm. ^{35}Cl SP MAS NMR spectra were collected at a spinning rate of 14 kHz using an excitation pulse of 1.5 μs and were referenced with respect to a 1M NaCl solution using reagent-grade KCl as an external reference set at +3.07 ppm (Bryce and Sward, 2006). ^{19}F SP MAS NMR were collected at a spinning rate of 24 kHz with 5 μs excitation pulses on a 3.2 mm Varian/Chemagnetics probe configured to give a low ^{19}F background signal. No ^{19}F signal was observed after several days of acquisition on an empty rotor. Using the quadrupolar frequency (ν_Q) for ^{35}Cl in the synthetic apatite obtained from the ^{35}Cl SP MAS spectrum, and a spinning rate of ν_{rot} = 16 kHz, the rf amplitude applied to the ^{35}Cl spins during the TRAPDOR experiment (ν_1) was set to 83.3 kHz so that the adiabaticity parameter (α'), calculated as $\alpha' = \nu_1^2 / \nu_{rot}\nu_Q$, would be approximately greater than one (Grey and Vega, 1995). The ^{19}F observed spectra were referenced with respect to $CFCl_3$. The ^{1}H SP MAS NMR spectra were obtained on a 400 MHz Varian Inova operating at 399.76 MHz using a Chemagnetics probe assembly configured for 4 mm (o.d.) rotors and modified to yield very low ^{1}H background signal. The probe assembly with empty rotors yields a broad ^{1}H background signal that is much lower than that from

the sample and which was not removed from the spectra. A spinning rate of 15 kHz and a 90° pulse width of 3.5 μs were used. The ^{1}H MAS NMR spectra were referenced with respect to tetramethylsilane (TMS) by setting the hydroxyl resonance in reagent-grade hydroxylapatite to +0.2 ppm. $^{31}P\{^{1}H\}$ 2-dimensional (2-d) Heteronuclear Correlation (HetCor) NMR spectra were collected on the 400 MHz spectrometer at frequencies of 162.82 MHz and 399.76 MHz for ^{31}P and ^{1}H respectively. A total of 128 hypercomplex points in t_1 were collected with a 20 μs increment, corresponding to a 50 kHz F1 spectral window. A spinning rate of 10 kHz was used and spectra collected at contact times ranging from 1.0 to 15.0 ms using a linear ramp of the ^{1}H field to optimize signal intensity. Data were processed with standard linear prediction methods to complete the signal in t_1.

2.3. Results

2.3.1. Apatite Synthesis

The above synthesis technique produced chemically homogenous apatite crystals with compositions in the range $Ca_{4.99\text{-}5.06}(PO_4)_{2.98\text{-}3.00}F_{0.51\text{-}0.48}Cl_{0.38\text{-}0.36}OH_{0.14\text{-}0.12}$ as determined by electron microprobe analysis (Table 2.1). Sample purity was tested by X-ray powder diffraction, and no phase impurities were observed within the detection limits of our scan. The crystals ranged in size from about 30-80 μm in their longest dimension with aspect ratios of about 7:1 or less. Noteworthy is the amount of calculated OH^- content even after the cumbersome drying technique. We believe this calculated OH^- value is real and reflects the extremely hygroscopic nature of $CaCl_2$.

2.3.2. Single Crystal XRD

The details of the crystal structures are given in Table 2.2. Atomic coordinates and isotropic displacement parameters are given in Table 2.3. Anisotropic displacement parameters are given in Table 2.4. Selected atomic distances are shown in Table 2.5, and bond angles are given in Table 2.6. The crystal structure of our synthesized apatite was solved and refined in the hexagonal space group $P6_3/m$. All reflections were used in the refinement of the structural model. Attempts to refine structure models in space group $P2_1/b$, were unsuccessful, because of a lack of data at positions indicative of the lower symmetry.

Fourier difference maps were synthesized with no anions along the *c*-axis and two large residual peaks were observed. The peak corresponding to lower electron density was located on the mirror plane, [0, 0, ¼], and was assigned to F. The peak with higher electron density was located at [0, 0, 0.361] and was assigned to Cl. A residual density peak corresponding to the hydroxyl oxygen could not be found, probably because of the low abundance of OH^- in the sample. When the refinement was carried out using the above anion positions and proper occupancies, Cl atoms lie closer to the mirror plane than the hydroxyl O atoms. When the hydroxyl O was forced to be at [0, 0, 0.203], that is, at the position reported by Hughes et al. (1990), the displacement parameter of the hydroxyl O atom became negative. If the hydroxyl O is placed further away from the mirror plane at [0, 0, 0.085], its displacement parameter becomes more satisfactory. The coordination environment around Ca(2) was also examined to aid the determination of the position of the hydroxyl oxygen. With the hydroxyl O at [0, 0, 0.085], the bond valence sum (Brese and O'keeffe, 1991) around Ca(2) is calculated to be 1.86, which is slightly smaller than the expected value of 2. If the hydroxyl O is at [0, 0, 0.203], then the bond valence sum around Ca(2) becomes 2.00, matching the oxidation state of Ca^{2+}. Based on the bond valence calculations, the position reported by Hughes et al. (1990) seems to be a more appropriate choice. At this point it cannot be definitively stated that the reported O(H) position in Table 2.3 is a new one because the amount of OH^- is too small to locate its position accurately with X-ray diffraction data (equivalent to one H atom). Moreover, its position is especially difficult to locate because of the rather large displacement parameters of F and Cl along the c-axis (Table 2.4). Examination of the Fourier difference maps as well as the anisotropic displacement parameters of the Cl atom did not indicate multiple Cl positions. Therefore, it appears that the Ca(2) site was not split into two distinct sites. When the Ca(2) position was forced to split into two separate sites, the refinement became unstable with negative displacement parameters. The single crystal data were visualized through the program MAX3D, which combines all diffraction frames and makes 3-D images of the reciprocal space. The program revealed the presence of spot-splitting and diffuse scattering consistent with incommensurate scattering occurring perpendicular to the a^*c^* plane (Fig. 2.1).

2.3.3. NMR Spectroscopy

^{31}P Single-Pulse (SP) MAS NMR spectra reveal a complex lineshape for the synthesized apatite that appears to contain a peak at +2.9 ppm and a shoulder at +1.7 ppm (Fig 2.2a). ^{31}P{^{19}F} CP/MAS spectra collected at a variety of contact times (Fig 2.2b-c) are all essentially identical to the SP spectrum. The ^{31}P{^{1}H} CP/MAS spectra (Fig 2.2d) contain a broad asymmetric peak that resembles the shape of the ^{31}P SP and ^{31}P{^{19}F} CP/MAS spectra. The similarity of the SP and CP/MAS spectra indicate that the structure observed in these spectra does not arise from local variations in the distribution of F, Cl, and OH in the channels. For example, ^{31}P{^{19}F} CP/MAS at short contact time would selectively enhance the signal from P near any F-rich clusters, but the data show no evidence for distinct spectral features at short (0.3 ms) contact time. The XRD results show only a single crystallographic P position. We tentatively attribute the structure in the ^{31}P peak shape to a structural modulation that was also noted in the XRD data (Fig. 2.1). Effects of non-linear structural modulations on MAS NMR spectra are described by Phillips (2000).

The ^{19}F SP MAS spectrum of the synthetic apatite sample shows a peak shape that appears to contain a peak at -103.3 ppm and a shoulder at -97.4 ppm (Fig 2.3a). The peak at -103.3 ppm is similar to those previously reported for fluorapatites (Braun et al., 1995). This spectral profile also occurs in the spinning sidebands and did not vary with relaxation delays, indicating the F species represented by these peaks are contained in the same phase.

^{19}F{^{35}Cl} TRAPDOR NMR data were collected to investigate the connectivity of the ^{19}F and ^{35}Cl spins in the apatite channels. Figure 2.3 (b-d) shows the results obtained using an echo delay of 12 rotor cycles (750 μs). The ^{19}F spin-echo spectrum (S_0; Fig 2.3b) shows all of the ^{19}F in the sample and closely resembles the SP spectrum, with two features seen at -97.4 ppm and -103.3 ppm and spinning sidebands. The TRAPDOR NMR experiment reduces the signal intensity for F located near the ^{35}Cl spins by irradiation at the ^{35}Cl frequency during the ^{19}F spin-echo, which recouples the dipolar interactions between the ^{19}F and ^{35}Cl spins. The results (S; Fig 2.3c) show a significant TRAPDOR effect, $(1 - S/S_0) \approx 0.5$ for these experimental conditions, indicating close F-Cl spatial proximity. The TRAPDOR difference spectrum (S_0-S; Fig 2.3d) contains signal only from ^{19}F species that are associated with the ^{35}Cl spins in the sample and shows no

change in the spectral profile compared to the spin-echo and SP spectra. $^{19}F\{^{35}Cl\}$. TRAPDOR data collected at irradiation periods (τ) from 0.125 to 5 ms show that the TRAPDOR fraction, $(S_0-S)/S_0$, rapidly approaches 0.94 (Fig. 2.4A). This value is consistent with a well ordered F/Cl distribution, in which 6% of the F should have two ^{37}Cl neighbors (24.47% natural abundance). These results indicate that all of the F atoms are closely associated with Cl atoms in this sample and that the asymmetric spectral profile does not arise from variations in the local Cl, F distribution.

^{35}Cl SP MAS NMR spectra (not shown) were taken to derive information needed for the $^{19}F\{^{35}Cl\}$ TRAPDOR NMR experiments. The ^{35}Cl NMR signal is easily observed and is characterized by a 2nd order quadrupolar lineshape with a chemical shift of about +115 ppm, a quadrupolar coupling constant of C_Q = 1.6 MHz. This value is somewhat larger than a previously reported measurement for chlorapatite, C_Q = 0.8 MHz (Bryce and Sward, 2006).

Simulations using the SIMPSON software package (Bak et al., 2000) were also preformed to analyze the variation in the TRAPDOR effect with ^{19}F-^{35}Cl internuclear distance. We used the internuclear distances of 2.62 and 5.31 Å derived from x-ray diffraction results corresponding to isolated F-Cl spin pairs occupying adjacent column positions and those separated by two intercolumn distances (Table 2.5). The simulations indicate that at a separation of 2.62 Å the TRAPDOR fraction, $(S_0-S)/S_0$, reaches 0.90 by 5 ms; a separation of 5.31 Å yields a TRAPDOR fraction less than 0.10 at 5 ms (Fig. 2.4B). Thus, $^{19}F\{^{35}Cl\}$ TRAPDOR spectra at τ = 5ms would contain >90% signal from any F further than one column spacing from Cl. No observable TRAPDOR fraction was found for simulations run at distances comparable to those for inter-channel separation (ca. 9 Å; not shown). These results correspond well to the TRAPDOR fractions we derived experimentally, which show a TRAPDOR fraction of 0.94 at 5 ms (Fig 2.4A). A more rapid increase in the TRAPDOR fraction is observed experimentally because the simulations used a single ^{19}F-^{35}Cl spin pair whereas 57% of the F in the apatite should have two ^{35}Cl neighbors (75.5% natural abundance). The key point is that the observed TRAPDOR effect is consistent with neighboring F and Cl within the channels as indicated by the XRD data, but could not arise from interactions of F and Cl located in adjacent anion channels. These observations are also consistent with F,Cl ordering in the

channels, which would yield a maximum TRAPDOR fraction of about 0.94 considering that 6% of the F should have two ^{37}Cl intercolumn neighbors (24.47% natural abundance). The ^{37}Cl atoms do not contribute to the $^{19}F\{^{35}Cl\}$ TRAPDOR effect. If F-rich clusters were present within the channels, the TRAPDOR fraction would be expected to be less than 0.94 because of the F atoms positioned farther than 5 Å from Cl (Fig. 2.4B). These TRAPDOR data indicate that there is no appreciable population of F atoms farther than 2.62 Å from any Cl atom.

To determine whether the synthetic apatite contained a significant hydroxyl component, ^{1}H NMR spectra were obtained. The ^{1}H SP MAS spectra of the synthetic apatite can be described by a broad resonance at +6.6 ppm, and three sharp resonances at +3.2, +1.9, and +1.1 ppm (Fig 2.5a). We do not observe any peaks in the range which would be expected for a pure hydroxylapatite, +0.2 ppm (Yesinowski and Eckert, 1987). The peak at +6.6 ppm exhibits a broad spinning sideband manifold (not shown in Fig 2.5a) that indicates it arises from rigid water molecules. The peaks at +1.9 and +1.1 ppm correspond closely to chemical shifts observed by Yesinowski and Eckert (1987) for a series of mixed fluor-hydroxylapatites. These authors assigned peaks in the range of +1.5 to +1.6 ppm to $OH^{-}\cdots F^{-}\cdots OH^{-}$ or $OH^{-}\cdots F^{-}\cdots F^{-}$ configuration and peaks in the range of +1.2 to +1.4 ppm to $OH^{-}\cdots F^{-}\cdots HO^{-}$. $^{31}P\{^{1}H\}$ HetCor NMR spectra of this sample were collected at a variety of contact times, all of which show only the peaks at +1.9 and +1.1 ppm in the ^{31}P-detected ^{1}H dimension (Fig. 2.5b). This result indicates that only the H atoms corresponding to these peaks are associated with the P in the apatite. Assignment of the peaks at +3.2 ppm and +6.6 ppm is uncertain but the HetCor data show that they are not associated with phosphate. The ^{1}H peaks at +3.2 and +6.6 ppm in this sample also exhibit spin lattice relaxation times (T_1; observed as variations in relative intensity difference with pulse delay) that differ from those of the peaks at +1.9 and +1.1 ppm. This is consistent with the occurrence of these H atoms in separate phases. These observations suggest that the peaks at +6.6 ppm and +3.8 ppm, which represent about 67% of the H in the sample, arise from unknown impurity phases in the sample, possibly unreacted $CaCl_2$.

2.4. Discussion

X-ray powder diffraction and EPMA analysis of the synthesized apatite crystals verified chemical homogeneity on the sample scale and the single crystal scale respectively (compositional range is $F_{0.51-0.48}Cl_{0.38-0.36}OH_{0.14-0.12}$); however, neither of the techniques could verify the presence or absence of fluor-rich and chlor-rich domains in the apatite crystals. Absence of such domains was verified by $^{19}F\{^{35}Cl\}$ TRAPDOR NMR experiments, which show that F and Cl atoms must be within about 3 Å of each other in order to describe the observed TRAPDOR effect. The anion position refinements indicate Cl···F inter-column distances of 2.62 Å, consistent with the $^{19}F\{^{35}Cl\}$ TRAPDOR NMR experiments.

The synthesized apatite was carefully indexed as hexagonal with space group $P6_3/m$, however the presence of incommensurate scattering suggests that the apatite may have some localized ordering with respect to anionic sequences within the hexagonal columns. This ordering was not extensive enough to induce overall monoclinic symmetry, but the presence of short-range monoclinic domains within the overall hexagonal average structure would be in agreement with the suggestions of Hughes and Rakovan (2002). Additionally, complex lineshapes in the ^{31}P and ^{19}F MAS NMR spectra were observed. $^{31}P\{^{19}F\}$ CP/MAS NMR experiments conducted at short contact times led to the conclusion that F-rich clusters are absent within the apatite channels and such clusters, therefore, cannot account for the complex lineshape in the ^{31}P MAS NMR spectra. We attribute the complex lineshapes in the ^{31}P and ^{19}F MAS NMR spectra to the presence of the incommensurate structural modulations. The $^{31}P\{^{19}F\}$ CP/MAS NMR results provide additional evidence for anionic mixing within the apatite channels because it further verifies that the channels are mixed with respect to fluorine.

The apatite synthesized for this study was not OH^--free (as determined both by difference using EPMA data, and by $^{31}P\{^1H\}$ CP/MAS and HetCor NMR), so direct implications for the stability of truly binary F-Cl apatite from this work is not possible. However, these results indicate the possible stability of binary (OH^--free) fluor-chlorapatite and warrant further concerted synthesis efforts.

2.5. Acknowledgments.

The authors thank Dr. Yu-Sheng Chen at ChemMatCARS, APS, for his assistance with single crystal X-ray diffraction. ChemMatCARS Sector 15 is principally supported

by the National Science Foundation/Department of Energy under Grant CHE-0087817. The Advanced Photon Source is supported by the U.S. Department of Energy, Basic Energy Sciences, Office of Science, under Contract No. W-31-109-Eng-38. The MAX3D image was provided by Dr. J. F. Britten at the Department of Chemistry, McMaster University. This work was partially supported by NASA Grant NNG04GM79G awarded to Hanna Nekvasil. Hyunsoo Park is grateful for support from NSF-DMR 0452444 and EAR-0510501 to John B. Parise. We would also like to thank John M. Hughes, Michael Fechtelkord, and Richard Thompson for insightful and thorough reviews of this paper, and we would like to thank Michael Fechtelkord and George Lager for the editorial handling of this paper.

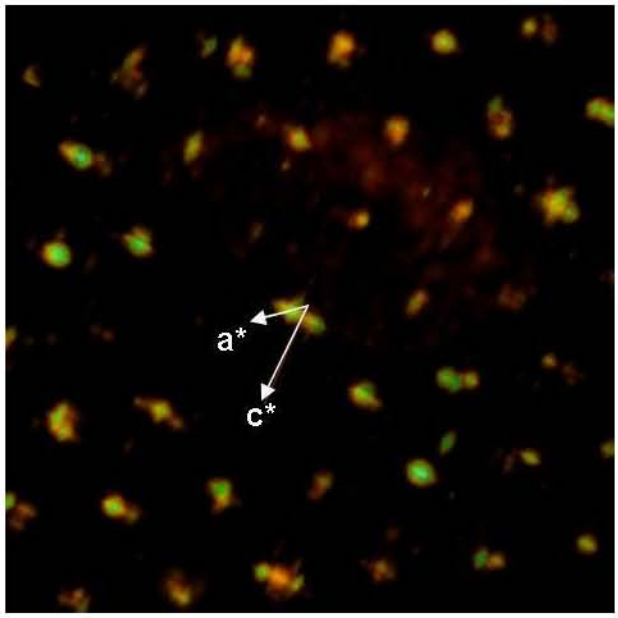

Figure 2.1. A snapshot of the single crystal X-ray diffraction data using MAX3D. The splitting of the diffraction spots suggests incommensurate scattering perpendicular to the a*c* plane.

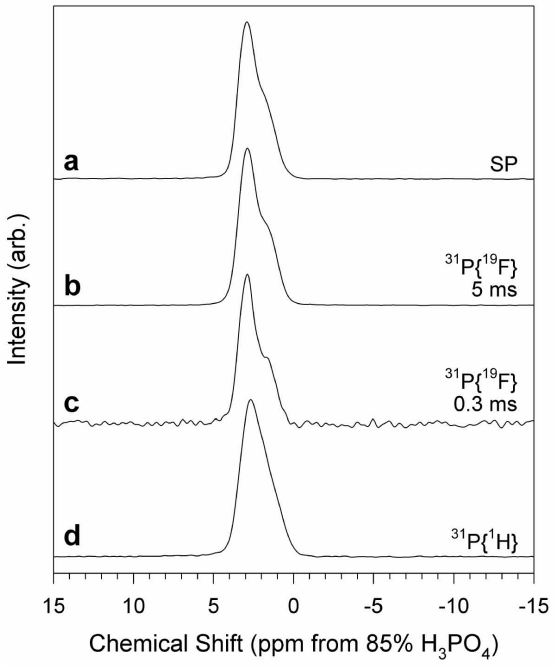

Figure 2.2. ^{31}P MAS NMR spectra of the synthesized apatite sample. **a)** ^{31}P SP spectrum (SP) at a pulse delay of 120 s. **b)** $^{31}P\{^{19}F\}$ CP/MAS spectrum at a contact time of 5 ms and a pulse delay of 60 s. **c)** $^{31}P\{^{19}F\}$ CP/MAS spectrum at a contact time of 0.3 ms and a pulse delay of 60 s. **d)** $^{31}P\{^{1}H\}$ CP/MAS spectrum at a contact time of 5 ms and pulse delay of 10 s.

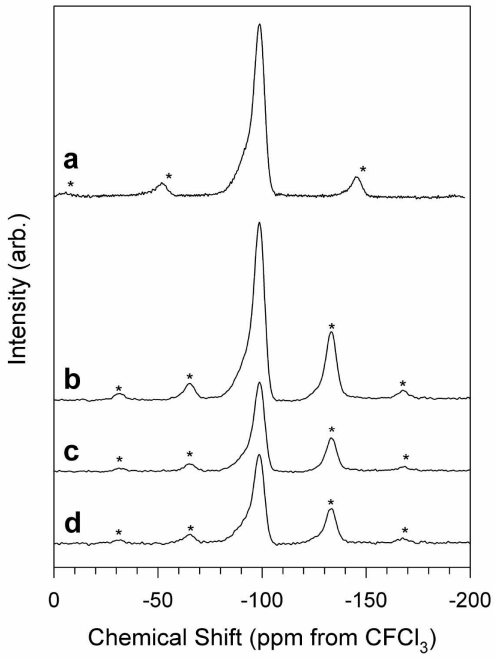

Figure 2.3. ^{19}F NMR spectra of the synthesized apatite sample **a)** ^{19}F SP MAS NMR spectrum collected at a spinning rate of 24 kHz and pulse delay of 200 s. **b-d)** $^{19}F\{^{35}Cl\}$ TRAPDOR spectral set collected at 12 rotor-cycle echo delay using a spinning rate of 16 kHz and a pulse delay of 100s. **b)** ^{19}F Echo control spectrum, S_0. **c)** ^{19}F-^{35}Cl TRAPDOR spectrum, S. **d)** Difference Spectrum, S_0-S. Spectra are scaled to reflect the absolute intensities. Asterisks denote spinning sidebands.

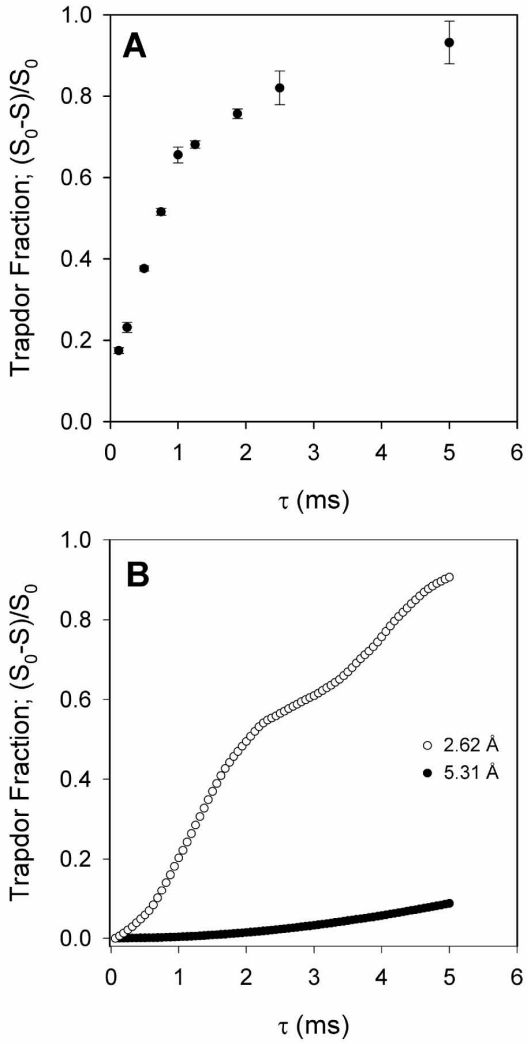

Figure 2.4. A. Experimentally measured TRAPDOR fraction, $(S_0-S)/S_0$, as a function of the irradiation period (τ) for the synthetic apatite. **B.** Calculated TRAPDOR fraction, $(S_0-S)/S_0$, as a function of irradiation period (τ) using F-Cl distances calculated from the x-ray diffraction study for the synthetic apatite corresponding to adjacent column positions (2.62 Å, open symbols) and a those separated by two column positions (5.31 Å ,closed symbols)

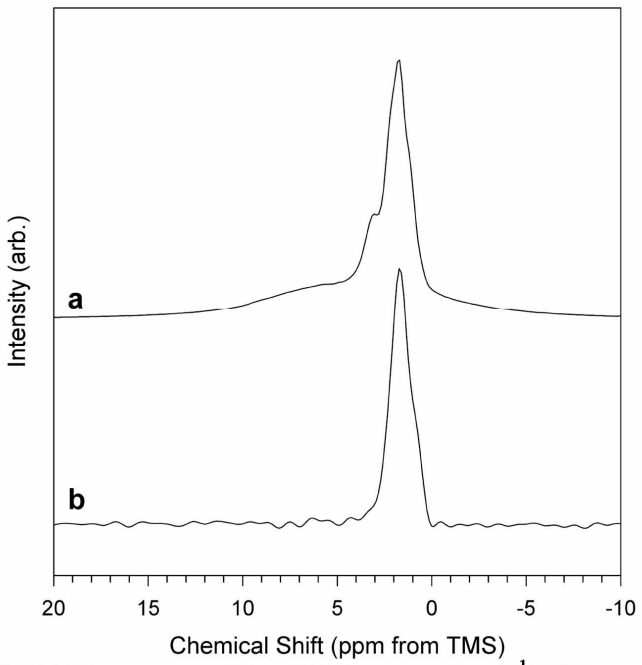

Figure 2.5. ^{1}H MAS NMR spectra of the FClAp sample **a)** ^{1}H SP spectrum collected at a 10 s pulse delay and 15 kHz spinning rate. **b)** Indirectly detected ^{1}H spectrum from $^{31}P\{^{1}H\}$ HetCor NMR spectrum of FClAp (slice taken at ^{31}P chemical shift of +2.9 ppm). A total of 128 hypercomplex increments in t1 were collected for 64 counts each at a spinning rate of 10 kHz, a pulse delay of 10s, and a contact time of 5 ms.

Table 2.1.. Electron Microprobe data of synthesized apatite

Oxide	Grain 1	Grain 2	Grain 3	Grain 4	Grain 5	Grain 5	Grain 5
CaO	55.1 (4)	55.4 (4)	55.2 (4)	54.9 (4)	55.3 (4)	54.4 (4)	54.8 (4)
P_2O_5	41.6 (3)	41.3 (3)	41.3 (3)	41.3 (3)	41.2 (3)	41.5 (3)	40.9 (3)
F	1.89 (4)	1.79 (2)	1.87 (2)	1.81 (4)	1.85 (2)	1.87 (2)	1.84 (2)
Cl	2.58 (6)	2.64 (6)	2.62 (6)	2.57 (6)	2.63 (6)	2.49 (6)	2.45 (6)
-O = F + Cl	1.38	1.35	1.38	1.34	1.37	1.35	1.33
Total	99.78	99.74	99.60	99.26	99.59	98.91	98.66
		Structural Formulae based on 13 Anions					
Ca	5.02	5.06	5.05	5.03	5.06	4.99	5.05
P	2.99	2.98	2.98	2.99	2.98	3.00	2.98
F	0.51	0.48	0.50	0.49	0.50	0.51	0.50
Cl	0.37	0.38	0.38	0.37	0.38	0.36	0.36
OH*	0.12	0.14	0.12	0.14	0.12	0.13	0.14
Cation Sum	8.01	8.04	8.03	8.02	8.04	7.99	8.03

*OH calculated by assuming F + Cl + OH = 1.

Numbers inside of parentheses correspond to absolute uncertainties in the last reported digit for each measurement.

Table 2.2. Crystallographic data for F,Cl,OH-apatite

Empirical formula*	$Ca_5Cl_{0.4}H_{0.1}F_{0.5}O_{12.1}P_3$
Formula weight (g/mol)	510.69
Collection Temp (K)	100(2)
Wavelength (Å)	0.49594
Space group	$P6_3/m$
Unit cell dimensions	a = 9.441(1)
(Å)	c = 6.835(1)
Volume (Å^3)	527.6 (2)
Z, calc. density (g/cm^3)	2, 3.214
Absorption coefficient (mm^{-1})	1.610
F(000)	506
Crystal size (mm)	0.03 x 0.03 x 0.03
θ range (°)	2.71 to 19.37
Index ranges	$-12 \leq h \leq 12$ $-12 \leq k \leq 12$ $-9 \leq l \leq 8$
Total reflections	7636
Independent reflections	454 [R(int) = 0.070]
Completeness to θ (%)	94.2
Absorption correction	SADABS
Max & min transmission	0.855 & 0.565
Refinement method	Full-matrix least-squares on F^2
Data/restraints/parameters	454/0/44
Goodness-of-fit	1.122
Final R [$I > 2\sigma(I)$]	R1 = 0.0245 wR2 = 0.0599
R (all data)	R1 = 0.0262, wR2 = 0.0606
Largest difference peak and hole (eÅ^{-3})	0.85 and -0.85

*Occupancies used for refining anion positions.

Table 2.3. Atomic coordinates and isotropic displacement parameters

	x	y	z	U (Å^2)
Ca1	2/3	1/3	0.00159(9)	0.00377(18)
Ca2	-0.00483(7)	0.24902(7)	1/4	0.00676(18)
P1	0.36958(8)	0.40062(7)	1/4	0.00156(18)
O1	0.4860(2)	0.3313(2)	1/4	0.0044(4)
O2	0.4654(2)	0.5889(2)	1/4	0.0076(4)
O3	0.2593(1)	0.3455(2)	0.0695(2)	0.0112(3)
F1	0	0	1/4	0.019(2)
Cl1	0	0	0.126(2)	0.029(2)
O4 (OH)	0	0	0.41(3)	0.26(8)

Table 2.4. Anisotropic Displacement Parameters

Atom	U_{11}	U_{22}	U_{33}	U_{23}	U_{13}	U_{12}
Ca1	0.0053(2)	0.0053(2)	0.0008(3)	0	0	0.00263(11)
Ca2	0.0025(3)	0.0120(3)	0.0021(3)	0	0	0.0009(2)
P1	0.0024(3)	0.0024(3)	0.0008(3)	0	0	0.0019(2)
O1	0.0033(8)	0.0068(9)	0.0056(9)	0	0	0.0044(7)
O2	0.0069(9)	0.0026(8)	0.0132(9)	0	0	0.0023(7)
O3	0.0095(7)	0.0229(8)	0.0074(7)	-0.0093(6)	-0.0059(5)	0.0128(6)
F1	0.007(3)	0.007(3)	0.042(6)	0	0	0.0035(16)
Cl1	0.0022(15)	0.0022(15)	0.081(7)	0	0	0.0011(7)

Table 2.5. Atomic distances

Bonds	Distance (Å)	Bonds	Distance (Å)
Ca1 – O1 x3	2.400(1)	P1 – O1	1.535(2)
Ca1 – O2 x3	2.443(1)	P1 – O2	1.540(2)
Ca1 – O3 x3	2.793(2)	P1 – O3 x2	1.528(1)
Ca2 – O2	2.339(2)		
Ca2 – O3 x2	2.333(1)		
Ca2 – O3 x2	2.510(1)	Anion ··· Anion	Distance (Å)
Ca2 – F1	2.3741(7)	F ··· OH	2.26
Ca2 – Cl1	2.520(6)	F ··· Cl	2.62
Ca2 – OH	2.60(2)	Cl ··· OH	3.05

Table 2.6. Selected bond angles (°)

O1^{i}—Ca1—O1^{ii}	75.46(5)	O3^{vi}—Ca2—Cl1^{ix}	120.9(3)
O1^{i}—Ca1—O1	75.46(5)	O3^{vii}—Ca2—Cl1^{ix}	83.3(3)
O1^{ii}—Ca1—O1	75.46(5)	O2^{viii}—Ca2—Cl1^{ix}	146.54(2)
O1^{i}—Ca1—O2^{iii}	91.89(5)	O3^{vi}—Ca2—O3^{xi}	79.21(3)
O1^{ii}—Ca1—O2^{iii}	153.37(6)	O3^{vii}—Ca2—O3^{xi}	137.15(6)
O1—Ca1—O2^{iii}	124.57(6)	O2^{viii}—Ca2—O3^{xi}	74.56(6)
O1^{i}—Ca1—O2^{iv}	153.37(6)	F1^{ix}—Ca2—O3^{xi}	81.48(4)
O1^{ii}—Ca1—O2^{iv}	124.57(6)	Cl1^{x}—Ca2—O3^{xi}	72.23(1)
O1—Ca1—O2^{iv}	91.89(5)	Cl1^{ix}—Ca2—O3^{xi}	91.50(2)
O2^{iii}—Ca1—O2^{iv}	75.91(5)	O3^{vi}—Ca2—O3	137.15(6)
O1^{i}—Ca1—O2^{v}	124.57(6)	O3^{vii}—Ca2—O3	79.21(3)
O1^{ii}—Ca1—O2^{v}	91.89(5)	O2^{viii}—Ca2—O3	74.56(6)
O1—Ca1—O2^{v}	153.37(6)	F1^{ix}—Ca2—O3	81.48(4)
O2^{iii}—Ca1—O2^{v}	75.91(5)	Cl1^{x}—Ca2—O3	91.50(2)
O2^{iv}—Ca1—O2^{v}	75.91(5)	Cl1^{ix}—Ca2—O3	72.23(1)
O1^{i}—Ca1—O3^{iii}	85.58(5)	O3^{xi}—Ca2—O3	58.90(7)
O1^{ii}—Ca1—O3^{iii}	143.16(5)	O3^{vi}—Ca2—O4^{ix}	78(4)
O1—Ca1—O3^{iii}	69.26(5)	O3^{vii}—Ca2—O4^{ix}	126(4)
O2^{iii}—Ca1—O3^{iii}	55.91(5)	O2^{viii}—Ca2—O4^{ix}	143(3)
O2^{iv}—Ca1—O3^{iii}	67.94(5)	O3^{xi}—Ca2—O4^{ix}	69.8(2)
O2^{v}—Ca1—O3^{iii}	124.66(5)	O3—Ca2—O4^{ix}	94(2)
O1^{i}—Ca1—O3^{v}	69.26(5)	O3^{vi}—Ca2—O4^{x}	126(4)
O1^{ii}—Ca1—O3^{v}	85.58(5)	O3^{vii}—Ca2—O4^{x}	78(4)
O1—Ca1—O3^{v}	143.16(5)	O2^{viii}—Ca2—O4^{x}	143(3)
O2^{iii}—Ca1—O3^{v}	67.94(5)	O3^{xi}—Ca2—O4^{x}	94(2)
O2^{iv}—Ca1—O3^{v}	124.66(5)	O3—Ca2—O4^{x}	69.8(2)
O2^{v}—Ca1—O3^{v}	55.91(5)	O3^{vi}—Ca2—O1^{xii}	70.98(4)
O3^{iii}—Ca1—O3^{v}	117.041(2)	O3^{vii}—Ca2—O1^{xii}	70.98(4)
O1^{i}—Ca1—O3^{iv}	143.16(5)	O2^{viii}—Ca2—O1^{xii}	102.95(6)
O1^{ii}—Ca1—O3^{iv}	69.26(5)	F1^{ix}—Ca2—O1^{xii}	104.66(4)
O1—Ca1—O3^{iv}	85.58(5)	Cl1^{x}—Ca2—O1^{xii}	103.79(5)
O2^{iii}—Ca1—O3^{iv}	124.66(5)	Cl1^{ix}—Ca2—O1^{xii}	103.79(5)
O2^{iv}—Ca1—O3^{iv}	55.91(5)	O3^{xi}—Ca2—O1^{xii}	150.19(3)
O2^{v}—Ca1—O3^{iv}	67.94(5)	O3—Ca2—O1^{xii}	150.19(3)
O3^{iii}—Ca1—O3^{iv}	117.041(2)	O4^{ix}—Ca2—O1^{xii}	103.2(5)
O3^{v}—Ca1—O3^{iv}	117.041(2)	O4^{x}—Ca2—O1^{xii}	103.2(5)
O3^{vi}—Ca2—O3^{vii}	138.80(8)	O1—P1—O2	111.08(1)
O3^{vi}—Ca2—O2^{viii}	86.77(4)	O1—P1—O3	111.47(8)
O3^{vii}—Ca2—O2^{viii}	86.77(4)	O2—P1—O3	107.48(8)
O3^{vi}—Ca2—F1^{ix}	102.17(4)	O3—P1—O3	107.67(1)
O3^{vii}—Ca2—F1^{ix}	102.17(4)	O3—P1—O3^{xi}	107.68(1)
O2^{viii}—Ca2—F1^{ix}	152.39(5)	O3—P1—O1	111.46(7)
O3^{vi}—Ca2—Cl1^{x}	83.3(3)	O3^{xi}—P1—O1	111.46(7)
O3^{vii}—Ca2—Cl1^{x}	120.9(3)	O3—P1—O2	107.48(8)
O2^{viii}—Ca2—Cl1^{x}	146.54(2)	O3^{xi}—P1—O2	107.48(8)

Symmetry codes: (i) 1-y, x-y, z; (ii) 1-x+y, 1-x, z; (iii) y, -x+y, -z; (iv) 1-x, 1-y, -z; (v) 1+x-y, x, -z; (vi) x-y, x, 0.5+z; (vii) x-y, x, -z; (viii) -x+y, 1-x, z; (ix) -1+x, y, z; (x) -1+x, y, 0.5-z; (xi) x, y, 0.5-z; (xii) -y, x-y, z; (xiii) 1-x, 1-y, 0.5+z; (xiv) -x+y, -x, z; (xv) 1-y, 1+x-y, z; (xvi) 1+x, y, z; (xvii) 1-x+y, -x, z; (xviii) 2-x, - y, -0.5+z; (xix) 2-x, -y, -z; (xx) 2-x, -y, 1-z; (xxi) 2-x, -y, 0.5+z.

Hydrous magmatism on Mars: A source for water on the ancient martian surface and the current martian subsurface?

F. M. McCubbin[1]*, A. Smirnov[2], H. Nekvasil[1], J. Wang[3], E. Hauri[3], and D. H. Lindsley[1]

[1]Department of Geosciences, State University of New York, Stony Brook NY 11794
[2]Geophysical Laboratory, Carnegie Institution of Science, 5251 Broad Branch Rd., N.W, Washington, DC 20015
[3]Department for Terrestrial Magnetism, Carnegie Institution of Science, 5241 Broad Branch Rd., N.W, Washington, DC 20015

3.1. Introduction

Water undoubtedly played a crucial role in Mars' geologic history and in any potential biologic history of the planet. Although evidence for surface and subsurface water is strong (Farmer et al., 1976; Glotch and Christensen, 2005; Golombek et al., 1997; Hartmann, 1979; Haskin et al., 2005; McEwen et al., 2007; Squyres et al., 2006b), the possible origin of this water from magmatic degassing of the planet remains in question. Current accepted estimates for water contents in the martian mantle range from about 1 to 37 ppm (Mysen et al., 1998; Wanke and Dreibus, 1994). Such low values appear incompatible with any significant amount of water in mantle-derived magmas and suggests that martian surface water was extra-planetary, brought in post magma-ocean by meteorites and comets (Lunine et al., 2003). In the absence of plate tectonics, such extra-planetary water would result in a shallow and short-lived Martian hydrosphere, both of which would severely inhibit the formation of a sustainable Martian biosphere (Fisk and Giovannoni, 1999; Jakosky, 1999; Sharma et al., 2002; Tosca et al., 2008a). But how well constrained is this low water content for the martian mantle? Here we re-examine the evidence for a dry martian interior using observations and analyses of minerals within the Chassigny martian meteorite.

The Chassigny meteorite is one of two known meteorites comprising the Chassignite class of SNC meteorites (Beck et al., 2006; McSween and Treiman, 1998). It

is a dunite consisting of cumulus olivine and spinel, and intercumulate pyroxene, maskelynite, apatite, ilmenite, and sulfides (Floran et al., 1978; Johnson et al., 1991; McCubbin and Nekvasil, 2008). Some of the cumulus olivine grains host polyphase "melt" inclusions (MI) containing augite, low-Ca pyroxene, kaersutite, pyrrhotite, chromite, pentlandite, Ti-biotite, apatite, rhyolitic glass, maskelynite, and ilmenite (Floran et al., 1978; Johnson et al., 1991; McCubbin and Nekvasil, 2008; Nekvasil et al., 2007; Varela et al., 2000; Wadhwa and Crozaz, 1995). Studies of this meteorite have led to two competing conclusions regarding the water budget of the magma that produced the melt inclusions. McCubbin and Nekvasil (2008) studied maskelynite (shocked feldspar) in melt inclusions and in the regions interstitial to the cumulus grains and concluded that water-rich fluids were responsible for maskelynite and alkali-maskelynite compositions in the melt inclusions, indicating the trapped melt likely had elevated water contents. Yet, Watson et al. (1994), in their SIMS study of OH- in kaersutite and Ti-biotite in Chassigny melt inclusions, obtained low water contents that are incompatible with forming from a water-rich magma.

The observation of Watson et al. (1994) that the Chassigny melt inclusion kaersutite and biotite are water-poor is of such importance that it deserves detailed evaluation. Such water contents may reflect either the water content of the original hydrous minerals that crystallized in the melt inclusion or a post-crystallization process [exclusive of shock dehydration (Minitti et al., 2008a; Minitti et al., 2008b)]. If these water contents reflect the primary water contents of kaersutite and biotite, then they should satisfy the general crystal chemical constraints of the mineral structures. However, McCubbin et al. (2007b) have shown that there are strong crystal chemical arguments indicating that the measured low water contents cannot be an inherent igneous signature. Given the importance of such measurements and the disparate conclusions regarding the water content of the melt inclusion magma, we have reanalyzed, by secondary ion mass spectrometry (SIMS), OH^-, F, and Cl in both kaersutite and Ti-biotite in Chassigny melt inclusions.

3.2. Stoichiometry of Chassigny kaersutite and biotite based on previously published chemical analyses

Kaersutite [$A_{0\text{-}1}M4_2(M1\text{-}3_{4\text{-}4.5}Ti_{0.5\text{-}1})T_8O_{23}X_1$] is a Ti-rich amphibole that typically contains at least 1 structural formula unit (sfu) of (OH + F + Cl) in the O(3)

crystallographic site (depicted as X in above structural formula). Extensive analytical work has been conducted on kaersutite from the Chassigny meteorite because of its potential implications for magmatic water within the martian interior (Floran et al., 1978; Johnson et al., 1991; Monkawa et al., 2006; Watson et al., 1994). When all of the available published data are considered, a structural formula for the Chassigny kaersutite can be calculated based on normalization to 24 anions (Table 3.1, columns 1-2), which is the best normalization scheme for a well characterized O(3) site. The resulting structural formula yields an over-occupied A-site (by ~ 11-15%) and an unreasonably high A-site calcium content for each analysis, consistent with having too much calculated O^{2-} in the O(3) site. If the poor stoichiometry is attributed to water content, then correction of the stoichiometry (to diminish the amount of O^{2-} so that the A-site is no longer over-occupied) requires the water content of the kaersutite to be between 0.5-0.6 wt.% (Table 3.1, columns 3-4). Alternatively, the F and Cl contents are underestimated or the ferric iron measurement is incorrect. Further analysis of OH^-, F, and Cl by SIMS would permit assessment of all of these possibilities.

Biotite [$IM_{2-3}\square_{1-0}T_4O_{10}A_2$] is a mica that typically contains at least 2 structural formula units (sfu) of (OH + F + Cl + O) in the A- crystallographic site. Johnson et al. (1991) and Righter et al. (2002) analyzed F and Cl by EPMA (Table 3.2) in Ti-rich biotite in melt inclusions within cumulus olivine in the Chassigny meteorite. From their analyses, Righter et al. (2002) obtained a monovalent anion sum of 0.8 sfu (OH + F + Cl). This value indicates a high oxy-component in the volatile-site of Chassigny Ti-biotite and signifies that the incorporation of OH^-, F and Cl is likely controlled structurally and is associated with a Ti-O substitution mechanism. This substitution mechanism typically occurs in biotite crystallizing from relatively low-water systems (i.e., Cesare et al., 2008). In volatile-rich systems (i.e., typical terrestrial crustal granitoids and metamorphic rocks) Ti-incorporation into biotite occurs instead via a Ti-Tschermak or Ti-vacancy substitution mechanism (Sassi et al., 2008), which allows for much higher monovalent anion sums in these Ti-rich biotites. Given the large range in possible substitution mechanisms in biotite and the degree to which the biotite structure accommodates vacancies (Mottana et al., 2002), it is impossible to assess whether the previously published Chassigny biotite analyses yield accurate structural formulae.

3.3. Analytical Procedure

Back scattered electron (BSE) imaging and energy dispersive spectroscopy (EDS) were performed at the Geophysical Lab, Washington, DC on a JEOL JSM 6500F scanning electron microscope with a field emission gun equipped with a liquid N_2-cooled sapphire Si(Li) EDS detector (EDAX) using a 15kV operating voltage. EDS was used to chemically identify kaersutite and biotite grains; these were then imaged for crystal morphology using backscattered electrons (BSE) for subsequent location within the ion microprobe.

The measurements of F, H_2O (as OH^-), Cl and S were performed on a Cameca IMS-6f ion microprobe at the Department for Terrestrial Magnetism, Washington, DC using the procedure of Hauri et al. (2002). The focused (5-10 nA) 10 kV Cs^+ primary beam was rastered on the sample to a 25 by 25 micron area. The secondary ion beam was extracted at -5 kV from a 5 micron diameter of the rastered area with a field aperture. An electron flood gun (-5 kV) was used to compensate for charge build up in the analysis area. A mass resolution of 6000 was tuned to eliminate some of the interferences. Standardization of similar minerals was performed at the beginning of the session and checked in between analyses. Each analysis lasted about 15 minutes.

3.4. Results

3.4.1. SIMS data for Chassigny kaersutite and Ti-biotite

Three kaersutite grains and one biotite grain were analyzed for H_2O, F, Cl, and S by secondary ion mass spectrometry (SIMS) on 2 thin sections of the Chassigny meteorite. The kaersutite showed a range in water content from 0.41 to 0.74 wt.% (Table 3.3). These water contents are approximately four times higher than the previously published values (Watson et al., 1994) and within the predicted range needed to satisfy amphibole stoichiometry. The kaersutite grains analyzed had fluorine abundances which ranged from 0.4-0.72 wt.%, and chlorine abundances which ranged from 0.12-0.15 wt.%, consistent with previously published EPMA analyses (Johnson et al., 1991).

The Ti-biotite analyzed contained 1.24 wt.% water, an abundance 2.5 times greater than the previous analysis (Watson et al., 1994). Fluorine and chlorine were 0.72 and 0.03 wt.% respectively, which was considerably lower than values obtained by Johnson et al. (1991) and Righter et al. (2002) by EPMA (Table 3.2); yet, due to the higher water

contents, the volatile-site sum of our analysis is the same as that reported by Righter et al. (2002) (OH + F + Cl = 0.8 sfu), indicating a high oxy-component is present in the volatile-site of all analyzed Chassigny Ti-biotite (1.2 sfu O^{2-} in the volatile site).

3.4.2. Potential reasons for disparity between new and old analyses

The large differences between our analyses and those published by Watson et al. (1994) requires some potential explanation for the disparity. The analyses performed by Watson et al. (1994) were done using a Cameca IMS-3f ion microprobe, which is two generations older than the Cameca IMS-6f used in our study. The 6f instrument is capable of much better mass resolution than the 3f instrument (6000 vs. 1200). The better mass resolution allows us to distinguish between the $^{17}OH^-$ and $^{17}O^-$ masses, which facilitates the use of an anion collection routine. On the other hand Watson et al. (1994) measured for hydrogen directly, calculating OH from the $^1H^+/^{30}Si^+$ ratio of the sample. This routine requires that the ion beam has sufficient energy to break the OH bonds as the molecule is liberated from the mineral structure. In our routine, only enough energy was needed to remove the OH^- structural unit from the mineral.

While the 6f instrument is much newer and more advanced than the 3f instrument, there were also some very important analytical studies that were published subsequent to the previous analyses that have advanced the field of secondary ion mass spectrometry, making analysis routines such as the one used here more common and systematized (e.g., Hauri, 2002; Hauri et al., 2002). One area that has not improved much between the 6f and 3f models is the imaging system. It is very difficult to find your samples, even with intimate knowledge of sample topography. For the small (<10μm) kaersutite and biotite grains in the melt inclusions of the Chassigny meteorite this difficulty boarderd on sheer impossiblility. The only way that we were able to find our grains was by sputtering our sample and imaging based on the fluorine anions. This was only possible with the anion routine that we employed, and this method was not available to Watson et al. (1994).

One other possible reason for the differences between the old and new analyses has to do with sample history. Wagner et al. has recently shown that electron beam exposure during electron microprobe analysis can damage kaersutitic amphibole, driving hydrogen out of its structure. If Watson et al used samples that had been heavily studied by electron microprobe, the analyses could have been compromised regardless of the analyticaql care

that was taken to get good SIMS analyses. We have minimized electron beam exposure to our samples, and we are the first to study our slide that came from the Vatican Observatory.

Given the number of potential explanations as to why our results differ from those of Watson et al, coupled with the fact that our analyses provide consistent kaersutite stoichiometry when all the other published analytical data for the Chassigny kaersutite are considered, we feel that our data set provides the proper values to use when discussing monovalent anion concentrations of the Chassigny kaersutite and biotite.

3.5. Discussion

The water contents of the Chassigny kaersutite measured during this study were within the range predicted by stoichiometry (Table 3.1, columns 3-4). The analyzed volatile contents satisfy the stoichiometric requirements for kaersutite, including reasonable A-site occupancy and sufficiently low calcium contents in the A-site (Table 3.1, columns 5-6). The analyzed volatile contents for biotite suggest that at least some of the Ti-biotite in Chassigny was dominated by hydroxyl, not fluorine, also indicating that water was an important magmatic volatile in the melt-inclusion magma.

3.5.1. Implications for the water content of Chassigny parental magma

Published partition coefficients for water between amphibole and silicate melt indicate that the water content of the melt must be greater than the water content of the amphibole that crystallizes from the melt by about a factor of two (i.e., $D_{H_2O}^{amphibole/silicate\ melt} \leq 0.5$) (i.e., Johnson et al., 1991; Merzbacher and Eggler, 1984; Mysen et al., 1998; Ritchey, 1980). Assuming that this holds true for the kaersutite, the range in the measured water contents for the amphibole indicates a melt water content of 0.82 to 1.48 wt% H_2O once amphibole begins to crystallize (approximately double the values from Table 3.3). With this value constrained, we then need to estimate how much crystallization had occurred before amphibole appeared in order to calculate the water content of the melt parental to the Chassigny meteorite.

The martian surface rock Humphrey (from Gellert et al., 2006) was proposed as a possible parental liquid composition for the Chassigny meteorite (Filiberto, 2008). Therefore, experimental phase equilibrium data on the Humphrey rock composition crystallized at 9.3 kbar and 1.67 wt.% water content were used to approximate the extent

of crystallization that occurred before amphibole first appeared [data from McCubbin et al. (In Press-b)]. The onset of amphibole crystallization occurred once 44% crystallization had taken place. This would imply that the minimum water content of the parental melt ranged from 0.5 to 0.8 wt% H_2O, assuming that no hydrous minerals crystallized prior to amphibole crystallization. While Humphrey is not a perfect match for the parental liquid of the Chassigny meteorite, and the amount of crystallization before amphibole appears may differ from that of the true parent, Nekvasil et al. (2004) obtained similar extents of crystallization prior to the onset of kaersutite crystallization from a terrestrial mafic hawaiite proposed to represent the type of liquid trapped as melt inclusions in the Chassigny meteorite (Nekvasil et al., 2007).

3.5.2. Implications for the water content of the martian mantle

Work by McSween et al. (2006b) and Monders et al. (2007) have suggested that the Humphrey composition is a primitive melt formed by partial melting of the martian mantle at depth. Moreover, it is thought that the parental magmas of the Chassigny meteorite are the result of partial melting of the martian mantle (Boctor et al., 2003; Mysen et al., 1998). If this is the case, then the water content of the parental magma reflects the water content of the martian mantle source region and is a function of the amount of partial melting that occurred to produce the parental liquids to the meteorite (Table 3.1). If the martian mantle produced this liquid after about 10% partial melting (after McSween and Harvey, 1993; and Mysen et al., 1998), and water behaves incompatibly, the mantle source water content must range from ~460 to 840 ppm H_2O (Table 3.1). This range is more than an order of magnitude higher than previously proposed values (1-37 ppm) for Mars and on the same order as those estimated for the terrestrial mantle (as summarized by Bolfan-Casanova, 2005).

3.5.3. Implications for surface water contributions from magmatic degassing

The amount of water that could have been contributed to the surface by magmatic processes over time is a function of two main variables, 1) total hydrous magma production through time, and 2) the percent of magmatic water that becomes surface water. The average thickness of the secondary Martian crust is considered to be 30-40 km (McCubbin et al., In Press-a; Norman, 1999; Wieczorek and Zuber, 2004). If this secondary crust formed from hydrous magmas with water contents of 0.5 to 0.8 wt%, the

amount of water that could have been added to the martian crust and surface can be computed for the range of possible secondary crustal thicknesses. Because it is difficult to constrain the amount of magmatic water that would be converted to surface water (rather than into hydrous alteration minerals within the crust), we have plotted the global water depth as a function of the conversion percentage (Figure 3.2). These calculations indicate that the equivalent of hundreds of meters of water could have been added to the martian surface and atmosphere over time by magmatic processes alone. This water could easily account for the composition of the martian atmosphere (McSween and Harvey, 1993) and may have been substantial enough to explain many of the surface features that are attributed to the presence of flowing water (McSween and Harvey, 1993). In fact, McSween and Harvey (1993) reported that the equivalent of at least 450 meters of global surface water are required to explain erosion by floods on the martian surface. This number is obtainable by magmatic processes alone. If the secondary crust formed fairly quickly, before about 4 Ga (McLennan, 2001), much of this water would have been added to the martian surface within a few hundred million years, perhaps jumpstarting an early martian hydrologic cycle, especially if magmatic input is supplemented by meteoritic and cometary water.

3.6. Conclusions

New analyses of water contents of the hydrous minerals in the Chassigny meteorite provide the first direct evidence that Mars experienced hydrous magmatism. Furthermore, based on the young crystallization age of the Chassigny meteorite (~1.3 Ga), hydrous magmatism likely occurred over much of the planet's active igneous history. The elevated water contents of the minerals found in the Chassigny melt inclusions suggest that primary melts from the martian mantle have water contents similar to those of terrestrial tholeiites (Dixon et al., 1991) and that the martian mantle contains significantly higher water contents than previously deduced. This opens up the possibility of a large magmatic contribution of water to the martian atmosphere, the martian surface, and the martian subsurface. Furthermore, these results indicate the possibility of long-lived hydrothermal activity on the surface and subsurface, environments that may have been suitable for developing and sustaining life.

3.7. Acknowledgments

We thank Guy Consolmagno of the Vatican Observatory and Robert Dodd for providing us with thin sections of the Chassigny meteorite. We would also like to thank Charles Mandeville, Darby Dyar, and Laurie Leshin for discussions about the reliability of specific published data sets. FM is thankful for funding that was provided by the GAANN fellowship.

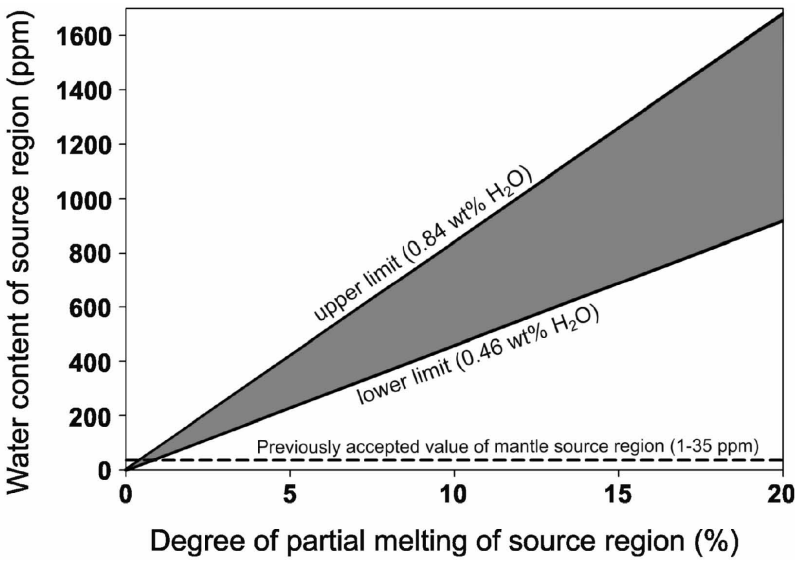

Figure 3.1. Possible range of water contents for the source region that produced the magma parental to the Chassigny meteorite as a function of the percentage of partial melting. The upper and lower lines for each range represent the possible range in parental magma water contents calculated for the Chassigny meteorite.

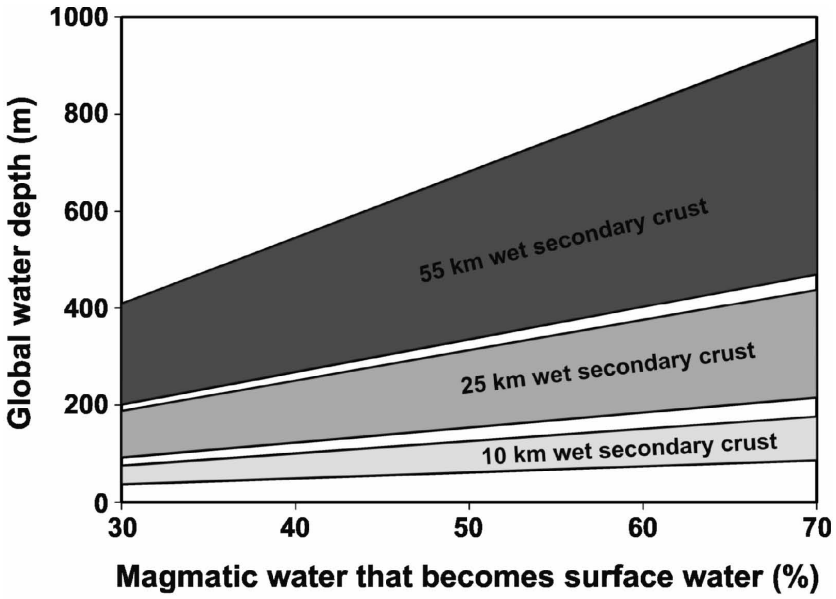

Figure 3.2. Global water depth as a function of the percentage of magmatic water that becomes surface water and total wet secondary crustal production. Water depth is computed assuming that the magmas composing the secondary crust had the same range in water contents as the parental liquids of the Chassigny meteorite. The upper and lower lines for each range represent the possible range in parental water contents calculated for the Chassigny meteorite. Secondary crust refers to any crustal material that formed after the initial crust that formed from an early magma ocean.

Table 3.1. Structural formulae of previously published Chassigny kaersutite based on normalization to 24 anions. Columns 1 and 2 represent structural formulae calculated from all the previously published data. Columns 3 and 4 represent predicted H_2O contents calculated assuming the A-site is not over-filled. Columns 5 and 6 represent structural formulae calculated using the averages of our new SIMS analyses.

Crystallographic site	Johnson* Published	Monkawa*** published	Johnson* predicted	Monkawa*** predicted	Johnson* our SIMS	Monkawa*** our SIMS
Si^{T}	5.99	5.92	5.94	5.88	5.94	5.87
Al^{T}	2.01	2.08	2.06	2.12	2.06	2.13
$Total^{T}$	8.00	8.00	8.00	8.00	8.00	8.00
Al^{M1-3}	0.53	0.61	0.46	0.56	0.46	0.54
Ti^{M1-3}	0.80	0.81	0.79	0.81	0.79	0.81
Cr^{M1-3}	-	0.02	-	0.02	-	0.02
Mg^{M1-3}	2.60	2.50	2.58	2.49	2.58	2.48
Fe^{3+M1-3}***	0.07	0.07	0.07	0.07	0.07	0.07
Fe^{2+M1-3}	0.98	0.96	1.08	1.02	1.08	1.05
Mn^{M1-3}	0.02	0.03	0.02	0.03	0.02	0.03
$Total^{M1-3}$	5.00	5.00	5.00	5.00	5.00	5.00
Fe^{M4}	0.28	0.29	0.17	0.21	0.17	0.18
Ca^{M4}	1.72	1.71	1.83	1.79	1.83	1.82
$Total^{M4}$	2.00	2.00	2.00	2.00	2.00	2.00
Ca^{A}	0.20	0.18	0.07	0.08	0.08	0.05
Na^{A}	0.88	0.88	0.87	0.88	0.87	0.87
K^{A}	0.06	0.04	0.06	0.04	0.06	0.04
$Total^{A}$	1.14	1.10	1.00	1.00	1.01	0.96
$F^{O(3)}$	0.24*	0.24*	0.24*	0.24*	0.25^{TS}	0.25^{TS}
$Cl^{O(3)}$	0.03*	0.03*	0.03*	0.03*	0.03^{TS}	0.03^{TS}
$OH^{O(3)}$	0.20**	0.20**	0.63^{C}	0.51^{C}	0.58^{TS}	0.58^{TS}
$O^{O(3)}$****	1.53	1.53	1.10	1.22	1.14	1.14
$Total^{O(3)}$	2.00	2.00	2.00	2.00	2.00	2.00

T, M1-3, M4, A, and O(3) refer to crystallographic sites shown in the generic kaersutite formula: $A_{0-1}M4_2(M1\text{-}3_{4-4.5}Ti_{0.5-1})[T_8O_{23}]O(3)_1$

* Values used from (JOHNSON et al., 1991)

** Values used from (WATSON et al., 1994)

*** Values used from (MONKAWA et al., 2006)

**** Values calculated by difference assuming F+Cl+OH+O = 2

^{C} Values calculated assuming the A-site is not over-filled

^{TS} Values are averages of the SIMS analyses from this study

Table 3.2. Previously published electron microprobe analyses of kaersutite and biotite grains from the Chassigny meteorite

Oxide	Johnson Kae*	Monkawa Kae***	Johnson Biot*	Righter Biot****
SiO_2	39.49	38.90	35.71	39.4
TiO_2	7.00	7.11	8.86	9.30
Al_2O_3	14.22	15.06	13.12	13.09
Cr_2O_3	-	0.20	-	-
FeO	9.95	9.83	12.12	9.54
Fe_2O_3	0.58***	0.58***	-	2.63[C]
MnO	0.17	0.22	0.50	0.07
MgO	11.53	11.05	14.09	13.70
CaO	11.80	11.58	0.01	0.55
Na_2O	2.99	2.99	0.17	0.37
K_2O	0.33	0.22	8.39	7.40
F	0.50	-	2.3	2.08
Cl	0.10	-	0.4	0.40
H_2O**	0.20	0.20	0.50	0.50
-O = F+Cl	0.23	-	1.06	0.97
Total	98.63	97.94	95.11	98.06

* Values used from (JOHNSON et al., 1991)
** Values used from (WATSON et al., 1994)
*** Values used from (MONKAWA et al., 2006)
**** Values used from (RIGHTER et al., 2002)
C Value was calculated by Righter et al. (2002) based on stoichiometry
The equivalent amount of oxygen was subtracted from each analysis based on its F and Cl contents

Table 3.3. Ion microprobe data for amphibole and biotite in the Chassigny meteorite

Wt%	Kae 1	Kae 2	Kae 3	Biot
H_2O	0.59	0.41	0.74	1.24
F	0.40	0.72	0.48	0.72
Cl	0.12	0.12	0.15	0.03
S	0.02	0.01	0.01	0.01

Hydrothermal jarosite and hematite in a pyroxene-hosted melt inclusion in martian meteorite MIL 03346: Implications for magmatic hydrothermal fluids on Mars

F. M. McCubbin[1]*, H. Nekvasil[1], N. J. Tosca[2], A. Smirnov[3], A. Steele[3], M. Fries[3], D. H. Lindsley[1]

[1]Department of Geosciences, State University of New York, Stony Brook NY 11794
[2]Department of Organismic and Evolutionary Biology, Harvard University, 26 Oxford St. Cambridge, MA 02138, USA.
[3]Geophysical Laboratory, Carnegie Institution of Science, 5251 Broad Branch Rd., N.W, Washington, DC 20015

4.1. Introduction

Identification of alteration assemblages in martian surface rocks containing jarosite and hematite have led to a variety of studies focused on constraining both the formation mechanism and the chemical nature of the waters involved in the precipitation of these assemblages (e.g., Glotch et al., 2004; Glotch and Rogers, 2007; Hurowitz and McLennan, 2007; King and McSween, 2005; Madden et al., 2004; McLennan et al., 2005; Navrotsky et al., 2005; Papike et al., 2006; Tosca et al., 2005; Tosca et al., 2008b). Such constraints have wide-ranging implications for understanding the history of the planet, from the timing of a functioning hydrologic cycle to the origin and sustainability of life on Mars. Thus far, much of our understanding of the formation mechanisms behind Jarosite-hematite assemblages on Mars is through low-temperature diagenetic processes; however, little is known regarding the role that high-temperature magmatic fluids may have played in producing these assemblages on Mars.

The formation of jarosite-hematite assemblages requires the presence of a highly acidic (pH <4), oxidized S- and Fe-rich brine (e.g., Papike et al., 2006). Magmatic fluids capable of producing such assemblages must also have these characteristics at low temperatures. Identification of such fluids capable of producing jarosite and hematite

upon cooling in martian samples is problematic and can only be done indirectly by studying martian meteorites that show subsolidus assemblages in melt pockets isolated from potentially infiltrating meteoric waters. Such isolated melt pockets may be best represented by mineral-hosted melt inclusions. The observation of a Cl-rich amphibole (Sautter et al., 2006) in the martian meteorite Miller Range 03346 (MIL 03346) represents a major step in the search for melt inclusions that have hosted concentrated fluids that produced subsolidus assemblages. Cl-amphibole is a non-magmatic hydrothermal amphibole (Mazdab, 2003), indicating the presence and retention of a concentrated hydrothermal fluid or saline melt into the subsolidus thermal regime. This work reports on further investigation of melt inclusions in MIL 03346 with a focus on identification and interpretation of subsolidus mineral assemblages and the nature of the fluids from which they formed.

MIL 03346 is a member of the Nakhlite class of SNC (martian) meteorites. It is a cumulate clinopyroxenite with cumulus clinopyroxene and olivine grains (Day et al., 2006; Dyar et al., 2005; Imae and Ikeda, 2007). Interstitial to these cumulus grains are skeletal titanomagnetites, small fayalitic olivines, chromite, pyrrhotite, cristobalite, apatite, chalcopyrite, and glass (Aoudjehane et al., 2006; Day et al., 2006; Dyar et al., 2005; Imae and Ikeda, 2007; Sautter et al., 2006). Some of the cumulus pyroxenes and olivines contain large (~50-100 μm) polyphase melt inclusions. These crystallized melt inclusions are reported to contain titanomagnetite, fayalitic olivine, chromite, pyrrhotite, cristobalite, apatite, chalcopyrite, glass, and Cl-rich amphibole (Aoudjehane et al., 2006; Day et al., 2006; Dyar et al., 2005; Imae and Ikeda, 2007; Sautter et al., 2006). MIL 03346 also has a low-temperature vein alteration assemblage reported to include Cl-poor smectite, iddingsite and jarosite (Herd, 2006; Sautter et al., 2006; Vicenzi et al., 2007a).

While MIL 03346 is broadly representative of the Nakhlites, in detail, it is unique in several ways. First, it is a highly oxidized rock; in fact, it has been referred to as the most oxidized martian meteorite found to date (Dyar et al., 2005). This is thought to be the result of an oxidizing magmatic environment, not a product of martian or terrestrial weathering (Dyar et al., 2005). Yet, the oxidation event appears to have occurred in the late magmatic stage since the cumulus pyroxene cores from MIL 03346 exhibit low ferric iron (Domeneghetti et al., 2007; Domeneghetti et al., 2006), which indicates that the high

ferric iron contents are concentrated in cumulus pyroxene rims and mesostasis. Aside from its oxidation state, MIL 03346 is currently the only Nakhlite known to contain Cl-rich amphibole within some of its mineral-hosted melt inclusions. Lastly, MIL 03346 is the only martian meteorite to date reported to contain jarosite among its alteration phases, albeit only in the post-crystallization vein assemblage (Herd, 2006; Vicenzi et al., 2007a; Vicenzi et al., 2007b). Collectively, these observations are central to placing constraints on the nature of fluids involved in the petrogenesis of MIL 03346.

Although the hydrothermal nature of Cl-rich amphibole found in MIL 03346 has not been questioned, the source of the Cl in the fluids is less clear. Sautter et al. (2006) suggested that the high chlorinity and oxidation state arose from magma assimilation of Cl- and ferric Fe-rich soils at or near the martian surface. However, this hypothesis is inconsistent with the low ferric iron contents of the cumulus clinopyroxene cores where the melt inclusions are found, and no mechanism has yet been proposed that would introduce such contaminated magma into melt inclusions after the formation of their pyroxene hosts.

Sautter et al. (2006) ruled out magmatic hydrothermal fluids from uncontaminated magma as a source of the Cl-amphibole based on the observed low temperature alteration vein assemblages (which were consistent with formation via water-rich, chlorine-poor fluid/rock interactions). However, there is no evidence that the Cl-amphibole and the low temperature vein assemblages must have formed from the same fluid, since vein-hosted low-temperature assemblages can be produced by meteoric waters at a variety of post-magmatic stages. For example, apatite from the Chassigny meteorite records high temperature (> 700 °C) Cl-rich fluid-rock interaction (McCubbin and Nekvasil, 2008); however, low-temperature [≤ 150 °C (Bridges et al., 2001)] alteration products within the meteorite record the presence of a fluid that did not contain high Cl. Given the potential importance of magmatic fluids in assessing the geologic history of martian magmatic systems, it is vital to search for subsolidus assemblages that could constrain the nature of such fluids.

The development of a magmatic fluid-mediated subsolidus assemblage requires an environment in which fluids are retained long enough for precipitation to occur. In rocks with fine-grained mesostasis, magmatic fluid retention into the subsolidus thermal

regime may only have been possible in melt inclusions. Therefore, we investigated melt inclusions in MIL 03346 for subsolidus mineral assemblages. However, because melt inclusion rupture does occur, we focused only on those inclusions that appear to have remained sealed over a significant period of their thermal history.

4.2. Analytical Techniques

4.2.1. Image Acquisition

Back scattered electron (BSE) imaging and energy dispersive spectroscopy (EDS) were performed at the Geophysical Laboratory, (Washington, DC) on a JEOL JSM 6500F scanning electron microscope with a field emission gun equipped with a liquid N_2-cooled sapphire Si(Li) EDS detector (EDAX) using a 15kV operating voltage.

4.2.2. Raman Spectroscopy

Raman micro-spectroscopy was performed at the Geophysical Laboratory, (Washington, DC) using a WITec-SNOM AFM instrument customized to accommodate confocal imaging geometry. A frequency-doubled solid-state YAG laser operating at 0-50 mW output power was used as the excitation source. The resolvable spot size for this technique is approximately 360 nm^2.

4.2.3. EPMA Analysis

Electron probe microanalysis (EPMA) of Cl-amphibole from a thin section (MIL 03346, 114 provided by NASA JSC) was performed at Stony Brook University (Stony Brook, NY) using a Cameca Camebax electron microprobe. An accelerating voltage of 15 kV and a nominal beam current of 10 nA were used during all analyses. A beam diameter of 3-10 μm was used for all analyses of Cl-rich amphibole. All other mineral phases were analyzed on a JEOL JXA-8800L microprobe at the Geophysical Laboratory (Washington, DC). An accelerating voltage of 15 kV and a nominal beam current of 10 nA were used for all analyses with a beam diameter ranging from ~2 to 10 μm.

4.3. Results / Data Reduction

4.3.1. Petrographic observations

Determining which melt inclusions have been breached and which ones have not is an important criterion for petrogenetic interpretation. For MIL 03346, melt inclusions that remained sealed at least into the high temperature hydrothermal regime can be

distinguished by the presence of Cl-amphibole. Because this amphibole requires a fluid or saline melt, it would only be present within areas of the meteorite where such a phase had remained trapped. It is recognized, however, that its absence does not fully imply rupture because each melt inclusion represents only a two-dimensional slice through a three-dimensional system. Melt inclusions that have clearly ruptured have a texture and mineralogy identical to the mesostasis. Neither the fayalitic olivine nor silica of the mesostasis were found in the Cl-amphibole-bearing melt inclusions investigated, so the presence of these phases in a melt inclusion likely indicates melt inclusion rupture. More than half of the melt inclusions observed appeared to have ruptured. Olivine-hosted melt inclusions, which do not rupture as easily as pyroxene hosted melt inclusions due to lack of cleavage (Veksler, 2006), were not observed in the thin-section we analyzed.

Petrographic descriptions of the mineral assemblages of MIL 03346 have been reported by Treiman (2005), Dyar et al. (2005), Day et al. (2006), Sautter et al. (2006), Imae and Ikeda (2007) and a number of abstracts. Our study of the cumulus and mesostasis mineral phases has yielded observations broadly consistent with previous studies, with one important new finding – the presence of jarosite, finely intergrown with hematite ± minor goethite in a clinopyroxene-hosted melt inclusion. This assemblage was conclusively identified by Raman micro-spectroscopy (Figures 4.1, 4.2) in a 10-15 μm^2 area surrounding a magmatic pyrrhotite grain within a Cl-rich amphibole-bearing melt inclusion. Other phases within this melt inclusion include titanomagnetite and two intergrown amorphous Fe-Si-rich phases containing submicron phosphate. Of the observed minerals, the Cl-amphibole, jarosite, and hematite ± minor goethite, clearly formed in the subsolidus thermal regime; the former two specifically require the presence of an aqueous phase (or perhaps a saline melt in the case of the Cl-amphibole).

4.3.2. Crystal chemistry of the Cl-rich amphibole

EPMA analyses of two Cl-rich amphiboles are shown in Table 4.1. The crystal-chemical formulae of the amphibole analyses were calculated based on 24 anions, 15 cations and 13 cations in order to assess the reliability of calculated values for ferric iron (Table 4.2). Recalculating the normalization scheme on the basis of 15 cations was found to be the most accurate formulaic representation because the 24-anion normalization

resulted in significant over population of the A-site, and the 13-cation normalization required atypical tetrahedral-site substitutions (i.e., Si + Al < 8 atoms).

The resulting amphibole stoichiometry (ideally: $A_{0\text{-}1}M4_2M(1\text{-}3)_5[T_8O_{22}]O3_2$) is presented at the bottom of Table 4.2. From our normalization scheme, we calculated $Fe^{3+}/\sum Fe$ values ranging from 0.09-0.14, which is significantly less ferric iron than calculated previously for the Cl-rich amphibole. Although the ferric iron contents were not directly measured, it must be noted that the high ferric iron contents implied by the stoichiometric computations conducted by previous investigators can arise from their use of a normalization scheme based on 13 cations (Sautter et al., 2006) and not necessarily reflect the actual ferric/ferrous ratio of the mineral (see Table 4.2 for an example of this). The chlorine contents of this amphibole are very high (~1.8 sfu), and the A-site is dominated by potassium (~0.7 sfu), therefore these are potassic-chlorohastingsites according to the nomenclature of Leake et al. (1978; 1997).

4.3.3. Crystal chemistry of melt inclusion jarosite

Raman spectroscopy revealed that the jarosite in Figure 4.1 was actually a fine-grained mixture of jarosite, hematite, and goethite. Additionally, during EPMA analysis, a portion of the beam extended into the neighboring region of a Fe-Si-rich phase, into the titanomagnetite phase, and into a phosphate phase. This necessitated mass balance correction of the analysis (Table 4.1, Column 1) in order to obtain the composition of the pure jarosite (Table 4.1, Column 2). For this correction, first, a sufficient amount of Fe-Si-rich phase was linearly subtracted from each analysis to remove all silica. Next, titanomagnetite was subtracted to remove all Ti. Finally, Ca was removed by apatite subtraction. Overall, the sum of overlapping phases comprised less than 10% of each analysis.

The structural formulae of the resulting compositions were then computed based on normalization to 14 anions with hematite subtraction until Fe + Al + Mg + Cr + Mn filled the M-sites in the jarosite structural formula. The amount of hematite subtraction required for each analysis ranged from about 20-50 wt%. Using the constraint of three M-site cations in a perfectly stoichiometric jarosite $[A_1M_3T_2O_8Z_6]$, our structural formulae resulted in a T-site sum of 2.02 and an A-site sum of 1.02. The amount of H_2O was

calculated such that OH^- + Cl filled the Z-site. The resulting composition was then normalized to 100 percent.

Deconvolution of electron microprobe data for the jarosite revealed that the A-site is occupied by only K and Na (0.84 and 0.18 structural formula units [sfu], respectively). Because these abundances fully occupy the A-site, no hydronium (H_3O^+) component is required. The T-sites are predominantly occupied by SO_4 (1.92 sfu) with minor PO_4 substitution (0.10 sfu). The M-sites are dominated by Fe^{3+} (2.85 sfu) with minor Al (0.10 sfu), and lesser Mg, Cr, and Mn (collectively 0.05 sfu).

Although jarosite has been found previously in MIL 03346 (Herd, 2006; Vicenzi et al., 2007a), it is commonly associated with fine grained goethite and occurs within small veins and fractures (Herd, 2006; Vicenzi et al., 2007a). Based on D/H isotopic ratios and textural evidence, Vincenzi et al. (2007b) concluded that the vein jarosite is likely Martian in origin and associated with aqueous alteration on the Martian surface. The presence of goethite rather than hematite in the veins suggests jarosite formation in the presence of low-temperature (< 100 °C) acidic oxidizing aqueous fluids (Cornell and Schwertmann, 2003) in a process similar to that invoked for the jarosite found at Meridiani Planum (SQUYRES et al., 2004; SQUYRES et al., 2006c). This vein jarosite is distinct from the melt inclusion jarosite identified in our study, which is confined to the melt inclusion and clearly represents a different set of chemical conditions.

4.4. Discussion

4.4.1. High-temperature Hydrothermal History of MIL 03346

Chlorine-rich potassic-hastingsite typically forms from hydrothermal or metasomatic fluids below the solidus temperature of the silicate melt (i.e., Kullerud and Erambert, 1999; Leger et al., 1996; Polovina et al., 2004; Sato et al., 1997; Vanko, 1986), although pinpointing the maximum thermal stability is hindered by a paucity of experimental data. In fact, Mazdab (2003) reported that potassic-chlorohastingsite (> 2 wt.% Cl) is typical of alkali-halide metasomatism associated with various types of ore-mineralization. The fluid could have either formed from the trapped melt during crystallization once fluid-saturation was attained (endogenous fluid), or from elsewhere in the magma plumbing system, becoming trapped along with surrounding melt by the

growing pyroxene crystals (exogenous fluid). Importantly, the high chlorine/hydroxyl ratio of the potassic-chlorohastingsite (9:1) indicates that chlorine activity was very high in the fluid, and the possibility of the fluid having been an alkali-halide melt cannot be excluded (Mazdab, 2003).

The presence of pyrrhotite and titanomagnetite in the melt inclusion indicates that the melt and/or fluid was elevated in iron, sulfur and titanium at the time of entrapment. Given the large collective area occupied by the potassic-chlorohastingsite, pyrrhotite, and titano-magnetite in Figure 4.1, it seems likely that the oxide and sulfide were included with melt at the time of entrapment (hence the melt was saturated with respect to these phases). Alternatively, an exogenous fluid was trapped with melt in the inclusion, and the fluid was responsible for precipitating the potassic-chlorohastingsite, titano-magnetite and pyrrhotite. Regardless of which is the case, the hydrothermal fluid was elevated in the volatiles Cl and S.

Water-bearing fluids high in NaCl- and/or KCl-components are likely to undergo phase separation (into L+V) even at elevated pressure and temperature ($\leq$1500 bars and 800°C (Liebscher, 2007)). Moreover, the presence of additional components in the fluid (e.g., S-species) would widen the immiscible vapor-liquid region to even higher temperatures and pressures (Webster and Mandeville, 2007). The vapor phase will be enriched in HCl and H_2S (and potentially HF, Si, B, and Cu) while the aqueous liquid would become enriched in alkalis, alkaline earths, and Fe-chlorides and sulfates (Baker et al., 2004; Bischoff et al., 1996; Hedenquist and Lowenstern, 1994; Shmulovich et al., 2002; Shmulovich et al., 1995). If this process were occurring in the melt interstitial to the cumulus clinopyroxene grains, the vapor phase could readily separate and leave the system. With potentially significant partitioning of H_2S into the vapor relative to SO_2 (Ohmoto and Rye, 1979) this vapor loss could increase the oxidation state of the magma as a whole, causing it to become increasingly oxidized as cooling proceeds. This may have been the mechanism behind the late oxidation of the cumulus pyroxene rims and the mesostasis.

Within a melt inclusion, however, both aqueous liquid and vapor could coexist. The overpressure induced by the phase separation may have been responsible for the extensive melt inclusion rupture observed. Any melt inclusions that remained sealed

were, in part, protected from the pervasive magmatic oxidation outside of the cumulus grains due to the redox capacity of the hosting cumulus pyroxene grains, shown to be at an oxygen fugacity of IW+2.2 (Domeneghetti et al., 2006). However, diffusive hydrogen loss from the sealed melt inclusions would have been driven by the over-pressure induced by phase separation, which would, in turn, oxidize the melt inclusion as a function of the degree of molecular dissociation of water.

Given the calculated low ferric iron content of the potassic-chlorohastingsite, the fluid was probably not very oxidized at the time of amphibole precipitation (i.e., King et al., 2000). However, this could be a result of the redox capacity of the hosting cumulus pyroxene grains. Therefore, even if vapor loss were responsible for the extensive late magmatic oxidation observed in the mesostasis and cumulus pyroxene rims, we cannot determine whether or not the potassic-chlorohastingsite precipitated before or after L+V separation occurred.

4.4.2. Low-temperature Hydrothermal History of MIL 03346

The absence of H_3O from the A-site of the jarosite studied here is consistent with jarosite formation under hydrothermal conditions (Brophy and Sheridan, 1965; Stoffregen, 1993) since H_3O-subsitution in jarosite is ubiquitous at low temperatures and pressures, but it does not occur above 100°C. The partitioning of sulfate into the liquid phase during L+V separation suggests that the aqueous liquid likely played the dominant role in jarosite formation. Because jarosite precipitation requires the presence of oxidized liquids, this oxidation must have occurred after precipitation of the potassic-chlorohastingsite. Existing thermochemical data can be used to constrain the hydrothermal redox conditions of the liquid during jarosite formation. Figure 4.3 shows a calculated stability diagram for pure K-jarosite, hematite, and pyrrhotite at 200°C (assuming that oxidation was rapid enough to prevent the formation of secondary sulfide). At this temperature, a log fO_2 of at least -34 must be attained before jarosite precipitates. Importantly, although an external oxidation event may have occurred as implied by the oxidized rims of the pyroxene cumulus grains, the oxygen fugacity required for Jarosite precipitation can be attained simply by decreasing the temperature of the liquid without the need for additional oxidation processes. Although the precise formation temperature cannot be determined, this lower redox boundary for jarosite may

be plotted as a function of temperature in order to obtain a range of possible oxygen fugacities (Figure 4.4).

The composition of the jarosite provides important constraints on the chemical nature of this liquid phase. The jarosite composition is largely potassic (K^+ fills 83% of the A-site) suggesting that the K^+/Na^+ activity ratio of the aqueous liquid at this stage was too high to incorporate abundant Na into the jarosite structure (Alpers et al., 1989; Stoffregen et al., 2000). The potassic nature of the aqueous phase is consistent with the potassic nature of the amorphous phases found in the melt inclusion.

Complete solid solution exists between the iron and aluminum endmembers of jarosite-alunite compositions (Stoffregen et al., 2000). The melt-inclusion jarosite analyzed in this study contains significant Fe and only a small proportion of Al (0.10 sfu) in the M-site in spite of the presence of significant available Al (as evidenced by the presence of the aluminous Fe-Si phases). This suggests that the parental liquids were dominated by Fe and that the pH of the parental aqueous phase was too low to facilitate hydrolysis of Al. Hydrolysis of aluminum would result in either significant Al incorporation into the jarosite structure or, at high Al and SO_4 activity, the precipitation of an alunite phase.

The association of jarosite with other minerals can also provide insights into reactions between the aqueous liquid and the melt inclusion minerals below the temperature of initial saturation with jarosite. Both goethite and hematite are found with jarosite in the melt inclusion and this association aids in constraining the pH of the fluid (Alpers et al., 1989). Figure 4.3 shows that the coexistence of jarosite and hematite would require the pH of the fluid to remain close to the jarosite/hematite boundary (approximately 1.2 at 200 °C). The low pH required for jarosite precipitation was likely obtained by oxidation of the pyrrhotite as it interacted with the cooling, increasingly oxidizing liquid.

The presence of goethite in the sample indicates that the parental liquid cooled to a temperature below 100 °C (the goethite-hematite transition) and remained at this temperature long enough to precipitate goethite (Figure 4.5). At 25 °C, goethite is more likely to be initially formed (Cornell and Schwertmann, 2003), requiring a pH of approximately 1.9 to result in goethite-jarosite co-precipitation (Figure 4.5). The jarosite

within the melt inclusions then, is likely to have precipitated continuously over a range of temperatures.

4.4.3. Implications for wide-scale Martian alteration enviornments

The discovery of jarosite, hematite, and goethite in a melt inclusion within MIL 03346 provides the first direct evidence that martian magmatic fluids have evolved to produce aqueous phases responsible for precipitating low-temperature alteration assemblages that have also been seen on the surface of Mars. The strong textural evidence for the formation of the melt inclusion jarosite by oxidation of a primary magmatic sulfide represents the first documented evidence for such a jarosite formation pathway on Mars [although it has been previously suggested (Burns, 1986; Burns, 1987; Burns, 1988; Burns and Fisher, 1990a; Burns and Fisher, 1990b). Jarosite formation by sulfide oxidation is not limited to high temperatures or pressures and would likely occur wherever liquid water interacts with sulfides in Martian rocks. On Earth, in mine waste environments, sulfide mineral oxidation is a common pathway for the formation of jarosite, goethite and hematite (Alpers et al., 1989). Such terrestrial environments also commonly host a rich and diverse community of microorganisms which thrive in the acidic, oxidizing fluids produced during the process (Alpers et al., 1989), although the ability to withstand acidity and salinity stress are the result of evolutionary mechanisms possibly requiring prolonged geological timescales. In addition, coupling of these environments with potentially high chlorine activities and, by inference, low water activity, may limit the chances that these environments were, in fact, cradles for life at the martian subsurface (Tosca et al., 2008a).

4.4.4. Implications for Ore Formation on Mars

MIL 03346 is the second martian meteorite to show definitive evidence for interaction with Cl-rich hydrothermal fluids (i.e., McCubbin and Nekvasil, 2008). Hydrothermal alteration of martian rocks by Cl-rich fluids has implications for potential ore-deposition. Ore bodies on Earth are largely correlated to chlorine "hot-spots", which are typically indicated by the presence of chlorapatite and chlor-amphiboles (i.e., BOUDREAU, 1993; BOUDREAU and MCCALLUM, 1989; BOUDREAU and MCCALLUM, 1992; MAZDAB, 2003; MEURER and BOUDREAU, 1996; WEBSTER, 1997b). Apatite from all martian meteorites have been identified as predominantly Cl-rich (Greenwood, 2005),

suggesting the possibility that high-Cl hydrothermal fluids may be widespread in martian igneous systems. However, if all the martian meteorites came from one geographically limited area, we could be seeing a limited slice of what martian magmatism has to offer. Because we lack sufficiently detailed geologic context for martian meteorites, and we have no way of assessing whether these rocks are representative or recording rare magmatic processes, sample return is a necessary next step in furthering our understanding of martian magmatism.

4.5. Acknowledgments

We thank the Meteorite curatorial staff at the Lyndon B. Johnson Space Center in Houston, TX for providing us with a thin section of MIL 03346 (#114). Finnancial support for this work was provided by NASA grant NNG04GM79G from the Mars Fundamental Research Program awarded to Hanna Nekvasil and Andrew Steele acknowledges financial support from the NASA SERLIDA program. Francis McCubbin is grateful for a Graduate Assistance in Areas of National Need (GAANN) Fellowship. Nicholas Tosca was supported by an Origins Postdoctoral Fellowship. Alexander Smirnov acknowledges fellowship support from the Carnegie Institution of Washington, Geophysical Laboratory and NASA Astrobiology Institute during this study.

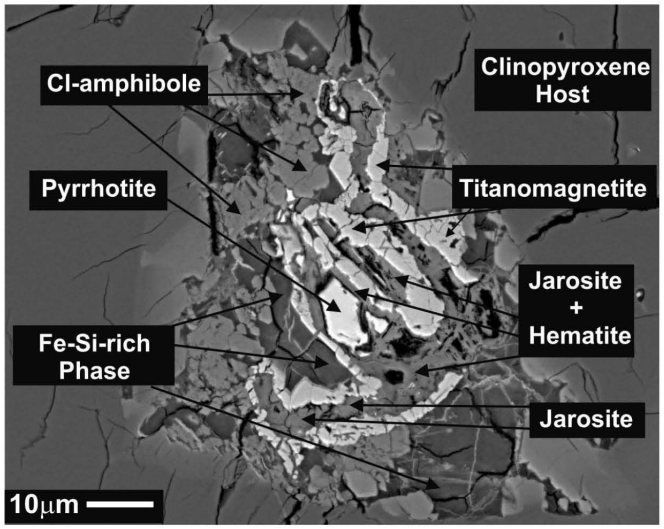

Figure 4.1. Back-scattered electron image of jarosite-bearing clinopyroxene-hosted melt inclusion in Martian meteorite MIL 03346. Phases and scale as indicated in image.

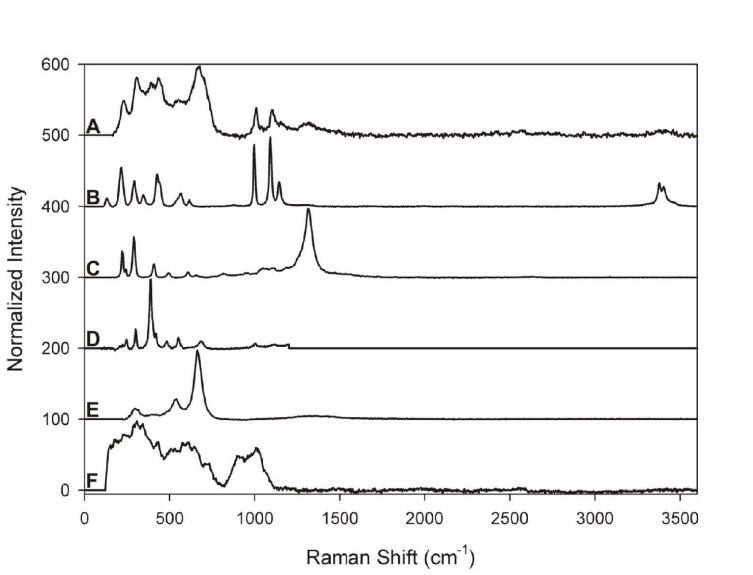

Figure 4.2. Raman spectra of phases within the jarosite-bearing melt inclusion. A) mixture of jarosite, hematite, and goethite collected at the edge of a titanomagnetite grain. B) jarosite C) hematite [from RRuff spectral library (DOWNS, 2006)] D) goethite [spectrum provided by Alian Wang from Washington University, St. Louis, MO] E) titanomagnetite E) Fe-Si rich phase.

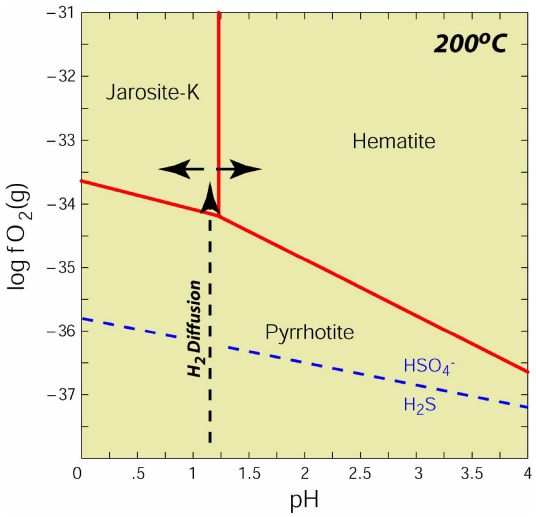

Figure 4.3. Computed jarosite stability diagram for 200°C and 100 bars (after Stoffregen (1993)). Thermodynamic data for endmember K-jarosite were obtained from Stoffregen et al. (2000). Data for pyrrhotite and hematite were taken from Robie & Hemingway, (ROBIE and HEMINGWAY, 1995). The diagram was constructed with log a_{SO4} = -0.5 and log a_K = -0.5. The dashed black line indicates the probable reaction pathway of H_2 diffusion in pH-logfO_2 space. The HSO_4^--H_2S equilibrium curve under these conditions is indicated in blue. The two black arrows in the jarosite and hematite stability fields represents the possible range in pH that jarosite-hematite co-precipitation is known to occur.

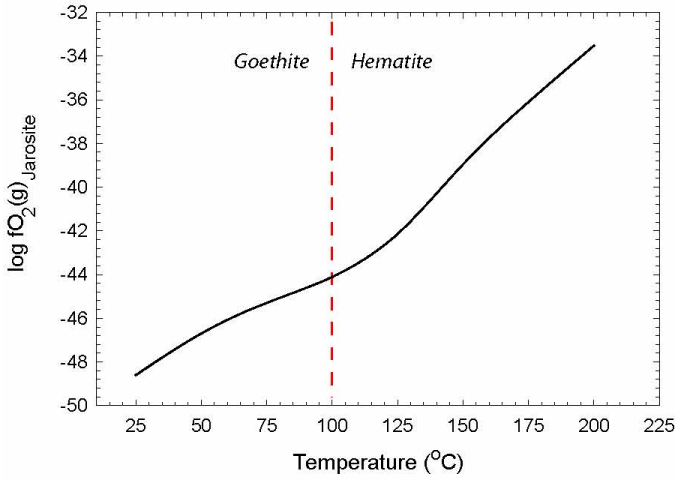

Figure 4.4. Calculated minimum oxygen fugacities ($fO_2(g)$) required for jarosite formation as a function of temperature. The dashed line indicates the temperature of the goethite-hematite transition.

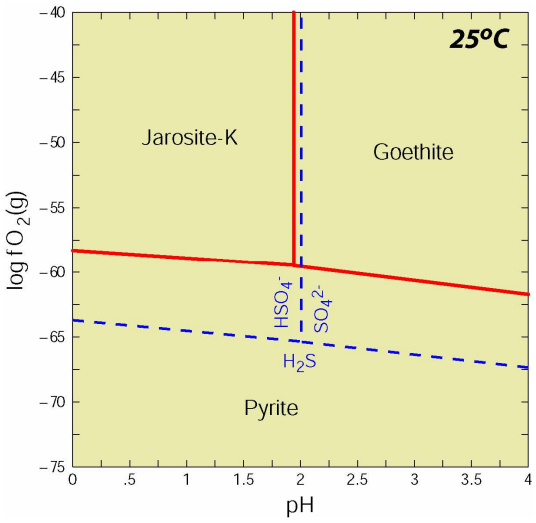

Figure 4.5. Computed jarosite stability diagram for 25°C and 1 bars (after Stoffregen (1993)). Thermodynamic data for endmember K-jarosite were obtained from Stoffregen et al. (2000). Data for pyrite and goethite were taken from Robie and Hemingway (ROBIE and HEMINGWAY, 1995). The diagram was constructed with log a_{SO4} = -0.5 and log a_K = -0.5. The HSO_4^--H_2S-SO_4^{2-} equilibrium curves under these conditions are indicated in blue.

Table 4.1. Electron microprobe data for phases identified within the jarosite-bearing melt inclusion.

Oxide	Jarosite*	Jarosite**	Fe-Si Phase	Cl-Fe-Si-Phase	Ti-Magnetite***	Cl-Amphibole	Cl-Amphibole	Pyrrhotite
SiO_2	2.32	0	45.3	45.3	0.22	35.6	35.3	-
TiO_2	0.28	0	0.19	0.07	16.6	0.24	0.24	-
Al_2O_3	0.97	0.94	8.76	3.62	3.15	10.4	9.48	-
Cr_2O_3	0.02	0.04	0.02	0.02	0	0.02	0.02	-
Fe^T	-	-	-	-	-	-	-	58.5
$Fe_2O_3^T$	65.3	48.85	28.8	38.8	32	-	-	-
FeO^T	-	-	-	-	46.1	32.7	34.1	-
MnO	0.12	0.18	0.23	0.14	0.53	0.21	0.21	-
Co	-	-	-	-	-	-	-	0.15
Ni	-	-	-	-	-	-	-	0.02
Cu	-	-	-	-	-	-	-	0.04
MgO	0.22	0.21	1.71	2.68	0.15	0.71	0.77	-
CaO	0.66	0	2	0.65	0.03	10.1	9.6	-
Na_2O	0.66	1.15	0.18	0.07	0.01	0.94	0.87	-
K_2O	4.82	8.44	1.19	0.76	0.06	3.27	3.23	-
P_2O_5	1.42	1.48	3.6	0.15	0.03	0.5	0.49	-
Cl	0.21	0.35	0.07	0.78	0	6.23	5.99	-
S^T	-	-	-	-	-	-	-	37.9
SO_3^T	18.5	32.73	0.86	0.76	0.04	-	-	-
Sb	-	-	-	-	-	-	-	0.03
H_2O	-	5.70***	-	-	-	-	-	-
-O = Cl	0.05	0.08	0.02	0.18	0	1.41	1.35	-
Total	95.5	100	92.9	93.6	98.9	99.5	99.0	96.6

*** Composition represents average of seven raw microprobe analyses of jarosite + mineral mixture**

**** Composition represents the average deconvolved jarosite composition**

***** Value was calculated based on stoichiometry**

^{T} Element measured as one oxidation state per analysis

Table 4.2. Amphibole structural formulae based on 24 anions, 15 cations, and 13 cations respectively.

Normalization to 24 Anions				***Normalization to 15 Cations***				***Normalization to 13 Cations***			
Si^{T}		6.14	6.16	Si^{T}		6.08	6.07	Si^{T}		6.01	5.96
Al^{T}		1.79	1.77	Al^{T}		1.85	1.86	Al^{T}		1.91	1.89
P^{T}		0.07	0.07	P^{T}		0.07	0.07	P^{T}		0.07	0.07
Fe^{3+T}		0.00	0.00	Fe^{3+T}		0.00	0.00	Fe^{3+T}		0.00	0.08
	$Total^{T}$	8.00	8.00		$Total^{T}$	8.00	8.00		$Total^{T}$	8.00	8.00
Al^{M1-3}		0.31	0.18	Al^{M1-3}		0.24	0.06	Al^{M1-3}		0.15	0.00
Ti^{M1-3}		0.03	0.03	Ti^{M1-3}		0.03	0.03	Ti^{M1-3}		0.03	0.03
Fe^{2+M1-3}		4.45	4.56	Fe^{2+M1-3}		4.08	4.02	Fe^{2+M1-3}		3.65	3.30
$Fe^{3+M1-3**}$		0.00	0.00	$Fe^{3+M1-3**}$		0.44	0.66	$Fe^{3+M1-3**}$		0.96	1.45
Mg^{M1-3}		0.18	0.20	Mg^{M1-3}		0.18	0.20	Mg^{M1-3}		0.18	0.19
Mn^{M1-3}		0.03	0.03	Mn^{M1-3}		0.03	0.03	Mn^{M1-3}		0.03	0.03
	$Total^{M1-3}$	5.00	5.00		$Total^{M1-3}$	5.00	5.00		$Total^{M1-3}$	5.00	5.00
Fe^{M4}		0.26	0.42	Fe^{M4}		0.15	0.23	Fe^{M4}		0.00	0.00
Ca^{M4}		1.74	1.58	Ca^{M4}		1.85	1.77	Ca^{M4}		1.83	1.74
Na^{M4}		0.00	0.00	Na^{M4}		0.00	0.00	Na^{M4}		0.17	0.26
	$Total^{M4}$	2.00	2.00		$Total^{M4}$	2.00	2.00		$Total^{M4}$	2.00	2.00
Ca^{A}		0.13	0.22	Ca^{A}		0.00	0.00	Ca^{A}		0.00	0.00
Na^{A}		0.31	0.29	Na^{A}		0.31	0.29	Na^{A}		0.14	0.02
K^{A}		0.72	0.72	K^{A}		0.71	0.71	K^{A}		0.71	0.70
	$Total^{A}$	1.16	1.23		$Total^{A}$	1.02	1.00		$Total^{A}$	0.85	0.72
$Cl^{O(3)}$		1.82	1.77	$Cl^{O(3)}$		1.80	1.75	$Cl^{O(3)}$		1.78	1.72
$OH^{O(3)*}$		0.18	0.23	$OH^{O(3)*}$		0.20	0.25	$OH^{O(3)*}$		0.22	0.28
	$Total^{O(3)}$	2.00	2.00		$Total^{O(3)}$	2.00	2.00		$Total^{O(3)}$	2.00	2.00

Amphibole formula: $(K_{0.71}Na_{0.30})(Ca_{1.81}Fe^{2+}_{0.19})(Fe^{2+}_{4.05}Fe^{3+}_{0.55}Mn_{0.03}Mg_{0.19}Al_{0.15}Ti_{0.03})[Si_{6.08}Al_{1.85}P_{0.07}O_{22}](Cl_{1.78}(OH)_{0.22})$

*Based on stoichiometry assuming OH + Cl = full O(3) site

**Based on charge balance

Compositional diversity and stratification of the Martian crust: Inferences from crystallization experiments on the picrobasalt Humphrey from Gusev Crater, Mars.

Francis M. McCubbin[1]*, Hanna Nekvasil[1], Andrea D. Harrington[1], Stephen M. Elardo[1], and Donald H. Lindsley[1]

[1]Department of Geosciences, Stony Brook University, Stony Brook NY, 11794-2100

Manuscript published in Journal of Geophysical Research- Planets, November, 2008

5.1. Introduction

Much of our understanding of the nature and timing of the formation of the Martian crust comes from isotopic and trace element investigations of the shergottite meteorites. Various short- and long-lived isotope systems (^{146}Sm-^{142}Nd, ^{147}Sm-^{143}Nd, ^{182}Hf-^{182}W, ^{87}Rb-^{87}Sr, ^{187}Re-^{187}Os) confirm that Mars experienced a major silicate differentiation early (~4.5 Ga) and did not experience "major melting" after this time (Borg et al., 1997; Borg et al., 2003; Brandon et al., 2000; Foley et al., 2005; Harper et al., 1995; Kleine et al., 2004; Kleine et al., 2002; Lee and Halliday, 1997; Yin et al., 2002). As summarized by McLennan (2001; 2003) and Wieczorek and Zuber [2004], this early differentiation resulted in a primary Martian crust that was enriched in large-ion lithophile (LIL) elements and isotopically isolated from the depleted mantle. After formation of the primary crust, a secondary crust formed upon input of magmas from the depleted Martian mantle (Taylor, 2001; Wieczorek and Zuber, 2004); the extent of this secondary magmatism was likely dictated by the budget of heat-producing elements in the depleted mantle (McLennan, 2001).

Relative thickness estimates for the primary and secondary crusts are under-constrained; however, upper and lower limits have been established. Wieczorek and

Zuber (2004) reported that the Martian crust likely ranges in thickness from 33-81 km, although the nominal value of 57 km is typically used (Taylor et al., 2006; i.e., Wieczorek and Zuber, 2004). Norman (1999) estimated on the basis of rare earth elements (REE's) and Nd isotope concentrations (in SNC meteorites) that the thickness of the primary crust ranges from 10-45 km, although 20-30 km is most likely. When these ranges are considered, the average thickness of the secondary Martian crust is 27-37 km with a possible range of 0-71 km; however, the upper and lower limits of this range are unreasonable when the young crystallization ages of the SNC meteorites (Nyquist et al., 2001) and the budget of heat producing elements in the mantle after planetary differentiation (McLennan, 2001; McLennan, 2003) are considered, respectively.

Given that the Martian crust is composed of at least some post-magma ocean igneous lithologies, the possibility exists for a compositionally diverse crust. In fact, some lithologic diversity has been observed on the Martian surface. Bandfield et al. (2004) and Christensen et al. (2005) have shown using various infrared instruments (Thermal Emission Imaging System [THEMIS] and Thermal Emission Spectrometer [TES]) that silica-rich lithologies exist on the Martian surface that deviate greatly from the basaltic materials that have been analyzed by the MER rovers (Clark et al., 2005; Gellert et al., 2006). In order to understand the extent of crustal diversity on Mars, comparison with terrestrial magmatic processes that give rise to such diversity on Earth can be very useful. Because of both the thick crust and the lack of evidence for plate tectonics (Breuer and Spohn, 2003 and references therein), cratonic intraplate magmatism is a good terrestrial analogue for the processes dictating lithologic diversity on the Martian surface.

It has been accepted for many years that igneous compositional diversity on Earth can arise by fractionation of mantle-derived magmas at depth (within or at the base of the crust) and subsequent ascent of residual liquids into the upper crust at various stages of fractionation (e.g., Albarede et al., 1997; Cox, 1972; MacDonald, 1968; Naumann and Geist, 1999; Nekvasil et al., 2004; Whitaker et al., 2007; Wright, 1970). In intraplate regions of thick crust on Earth, fractionation of tholeiite at the base of the crust and ascent of residual liquids has been called upon to produce lithologies as diverse as Fe-Ti-P-enriched ferrobasalts and anorthosites (along with their associated ferrodiorites,

syenites, and potassic granites) (Scoates et al., 1999; Thompson, 1975; Whitaker et al., 2007), sodic silica-saturated alkalic suites that produce hawaiite, tristanite, trachyte, and sodic rhyolite (Nekvasil et al., 2004), and nepheline (*ne*) normative hawaiites and phonolites (Filiberto and Nekvasil, 2003). The nature of the magmatic diversity arising in this manner likely varies not only with bulk silicate composition but with differing amounts of bulk water in the parental magma. Whitaker et al. (2005) have shown that terrestrial tholeiite having a bulk water content < ~0.4 wt% fractionating at 9.3 kbar, will give rise to a silica-depletion trend in the residual liquids, resulting in Fe-rich and Si-poor evolved magmas. In contrast, when bulk water contents were above this value, a silica-enrichment trend was observed in the residual liquids. While fractional crystallization is accepted as a magmatic process on Earth, there is little consensus regarding how important a role fractional crystallization has played for martian magmas (Christensen et al., 2005; McSween and Harvey, 1993; McSween et al., 2006a; Nekvasil et al., 2007; Rogers and Christensen, 2007; Taylor et al., 2006; Whitaker et al., 2005).

Fractional crystallization taking place at the base of or within the lower crust has major implications for the development of igneous stratigraphy and retention of such stratigraphy in the absence of subduction-related tectonics. Figure 5.1 shows schematically the crustal stratigraphy that would arise from fractionation of a magma at the base of the crust followed by emplacement of the residual melt at shallow levels or eruption onto the surface. But what is the extent of the lithologic diversity that can be produced solely by this process, and what are the compositional differences and volume relationships between the ascending residual magmas and the crystalline phases accumulating at the base of the crust?

The goal of this work is to provide constraints on the compositions and volumetric abundances of evolved magmas that could have contributed to the current Martian surface upon crystallization of a "primary" mantle-derived magma at the base of a thick Martian crust (chosen as ~70 km depth or 9.3 kbar pressure) by experimentally determining the nature of the residual liquids and fractionating mineral assemblages for both "wet" (1.67 wt%) and "dry" (0.07 wt%) compositions. The composition chosen for this study is that of the rock Humphrey, which is one of the Adirondack-class basalts analyzed by the MER rover Spirit in Gusev Crater, Mars (Squyres et al., 2006a). The

Adirondack-class basalts are picro-basalts that are believed to represent "near-primary" Martian melts (Monders et al., 2007). Texturally, Humphrey is a fine-grained vesicular basalt with up-to 25% megacrystic olivine (McSween et al., 2006b). Some debate exists as to whether or not the megacrystic olivine represents grains crystallized in situ or grains that were accumulated (if the grains were accumulated, then the reported composition for Humphrey would be displaced from a liquid composition); however, for the purposes of this study, it is assumed that Humphrey is representative of a liquid composition (after the view of McSween et al. (2006b), Monders et al. (2007) and Filiberto (2008)). Because the magmatic volatiles fluorine and chlorine are also likely constituents in Martian basalts (i.e., Gellert et al., 2006; Greenwood, 2005; McCubbin and Nekvasil, 2008), some fluorine and chlorine were added to the Humphrey composition so that the effect of water could be understood in the presence of such volatiles.

5.2. Analytical/Experimental Methods

5.2.1. Strategy

Crystallization experiments in which the starting material was melted before cooling to the temperature of interest were conducted at a range of temperatures at a pressure of 9.3 kbar to assess the compositions of the minerals and melts at various potential stages of melt separation. Relative abundances of all phases at each potential stage of liquid separation were computed by mass balance using analyses of residual liquids (i.e., the quenched glass of any given experiment) and all crystalline phases. Starting water contents of 0.07 wt% and 1.67 wt% were chosen in order to assess the effect of bulk water contents on liquid evolution.

5.2.2. Experimental methods

5.2.2.1. Starting materials

A mix was designed based on the Humphrey Rat 1 composition reported by Gellert et al. (2006) (reported in Table 5.1) but with 1500 ppm chlorine and 5000 ppm fluorine added. The mix was created by first accurately weighing oxide, Fe^0, CaF_2, and NaCl powders in the proportions needed for obtaining the desired composition. Next, the powders were mechanically mixed sequentially by volume in an automatic agate mortar/pestle grinder for a total of 3.5 hours. The $Fe^{3+}/\sum Fe$ value in the mixture was 0.16.

Because NaCl is soluble in ethanol, it was added to the mix subsequent to drying. The composition of this synthetic Humphrey mixture (Hsynth Dry) is reported in Table 5.1.

5.2.2.2. Piston-cylinder experiments

For each experiment conducted under "dry" conditions, the Humphrey powder was loaded into a graphite capsule and dried under vacuum at 800°C in a tube furnace in the presence of a Fe° oxygen getter for 20 minutes to remove structurally bound and adsorbed water. Subsequent to drying, the capsule was loaded into a $BaCO_3$ cell using the same cell assembly reported by Whitaker et al. (2007). The assembled cell was then placed within a ½ inch [1.27 cm.] piston-cylinder apparatus (using the piston-out method) and pressurized immediately to prevent water adsorption. Next the temperature was raised to a melting temperature of 1372°C. After melting for 2.5 hours, the temperature was rapidly dropped to the desired crystallization temperature and left to crystallize for a minimum of 2.5 days. The temperature of each experiment was both controlled and monitored by a Pt-$Pt_{90}Rh_{10}$ thermocouple. At the end of each experiment, the run was rapidly quenched isobarically.

For experiments run under hydrous conditions, synthesis of a hydrous glass was required. This was done by first loading water into a graphite-lined Pt-capsule before adding the synthetic Humphrey powder. Once the powder was loaded, the capsule's lid was welded on, and the capsule was inserted into a talc cell. The talc cell was then placed within a ¾ inch [1.90 cm.] piston-cylinder apparatus and pressurized to 9.3 kbar. The temperature was then raised to 1330°C and left to melt for 2.5 hours before rapidly quenching isobarically. The water content of the resulting glass was determined by micro-FTIR to be 3.31 wt. %. This hydrous glass was then mixed with dried synthetic Humphrey powder in order to obtain the desired starting water content of 1.67 wt. %. This mixture (Hsynth Wet, reported in Table 5.1) was used for all hydrous experiments reported for this work.

Experiments using the hydrous Humphrey powder were conducted in the same manner as the "dry" experiments with two exceptions. Instead of drying at 800°C, the loaded capsule was dried in a drying oven under vacuum at 130-150°C for 90 minutes to remove adsorbed water only. Secondly, the melting temperature for the "wet" experiments was 1330°C.

Since the experiments were performed in graphite capsules, the fO_2 was partially controlled by the graphite-CO-CO_2 (GCO) buffer. However, because no direct evidence was observed for the presence of a fluid, the GCO buffer provides only an upper limit to fO_2 (Eugster and Skippen, 1967). Whitaker et al. (2007) used the same experimental technique and reported that the fO_2 at 9.3 kbar typically ranged from 1.5-2.5 log units below the fayalite-magnetite-quartz (FMQ) buffer (using the QUILF routine of (Andersen et al., 1993)). None of our phase assemblages were appropriate for using QUILF to estimate fO_2, but we assume that it was similar to that reported by Whitaker et al. (2007)

5.2.3. Analytical Methods

5.2.3.1. EPMA Analysis

Electron probe microanalysis (EPMA) (exclusive of fluorine in glass and amphibole) was performed using a Cameca Camebax electron microprobe (EMP) equipped with four wavelength dispersive spectrometers. An accelerating voltage of 15 kV and a nominal beam current of 10 nA were used during analysis. For Na-bearing phases, the largest possible raster size was used to minimize unknown analytical problems that occur during highly focused electron beam analysis on such matrices. However, this alone did not prevent apparent Na-loss. Adopting the correction technique of McCubbin and Nekvasil (2008), Na was added back into the analysis such that normative corundum was no longer present for any Na-bearing phase. The IgPet Program Suite (Carr, 2002) was used to conduct mass-balance calculations using a least-squares routine. This was done to verify that no phase was overlooked during EPMA analysis, and to quantitatively estimate phase abundances. The computed phase abundances were used to calculate the bulk solid composition of the fractionating mineral assemblage at each temperature.

EMP analysis of the fluorine-bearing phases glass and amphibole were conducted with a Cameca SX100 microprobe at the American Museum of Natural History. Major element analyses were conducted with a 2 nA beam current, 15 kV accelerating voltage, and 10 μm beam diameter for Na. All other elements were measured using 10 nA and 15 kV with a 10 μm beam diameter.

5.2.3.2. Micro-FTIR Spectroscopy

Quantitative infrared spectroscopic measurements were conducted on experimental glass products at room-temperature in transmittance mode with a Thermo Nicolet 20SXB FTIR spectrometer attached to a Spectra Tech IR Plan microscope located in the Department of Earth and Planetary Sciences at the American Museum of Natural History. Both the spectrometer and the IR objective were purged with dry nitrogen gas at a rate of 15 l/min. Transmittance IR spectra were collected from doubly polished wafers of the run products over the mid-IR (1400-4000 cm^{-1}) to near-IR regions (3700-6500 cm^{-1}) using a KBr beam splitter, MCT/A detector, and globar source. Total dissolved water concentrations were determined for each glass from the intensity of the broad band at 3570 cm^{-1} after the calculation scheme of Mandeville et al. (2002). Approximately 1024 scans were performed for each IR spectrum acquired at a resolution of 4 cm^{-1}. All spots were first assessed optically to ensure that only glass was being measured during each analysis.

5.3. Experimental Results

5.3.1. "Dry" experiments

Experiments on the synthetic Humphrey mix under "dry" conditions at 9.3 kbar were conducted over the temperature interval 1270-1100°C. The run products of the experiments contained variable amounts of mineral phases and glass. Micro-FTIR analysis of residual glass indicates a starting water content of 0.07 wt%.

5.3.1.1. Mineral Phases

Compositions of mineral phases that formed during "dry" crystallization of Humphrey (Hsynth Dry) are presented in Table 5.2. Figure 5.2 shows the computed phase abundances from the experimental run products. Olivine and Cr-spinel are on the liquidus, and the next phase to appear is pigeonite at 1200°C, followed by plagioclase at 1150°C, and eventually augite at 1100°C. Once each phase enters the assemblage, it persists throughout the entire range of investigated temperatures.

Figure 5.3 shows olivine and pyroxene compositions projected into the pyroxene quadrilateral through QUILF (Andersen et al., 1993). Wollastonite components (Wo) of pigeonite range from Wo_{14}-Wo_{25}, while the single augite has an apparent Wo content of 23 mol%. The higher Wo-content of some pigeonite compositions compared with the

augite is an artifact of the QUILF projection scheme, arising from overcorrection of Wo in pigeonite and undercorrection in augite resulting from non-quadrilateral components in those phases. Although the plotted compositions look unusual, they have very little thermodynamic consequence because they lie near the crest of the augite solvus [personal communication from DHL]. Olivine ranges in composition from Fo_{70}-Fo_{46}.

5.3.1.2. Liquid Evolution

For the "dry" Humphrey composition, the liquidus temperature at 9.3 kbar is between 1250°C and 1270°C; the solidus temperature is below 1100°C (Fig. 5.2). Table 5.3 and Figure 5.4 illustrate the compositional evolution of residual liquids (i.e., glass product analyzed for each run and re-cast on a volatile-free basis in Fig. 5.4) and bulk solids (Table 5.4) along the "dry" crystallization path with decreasing temperature. As seen in Figure 5.3, the residual liquids exhibit a silica-depletion trend having strong K-, Ti-, P-, and Fe-enrichment with dropping temperature. Both Al and Na show initial enrichment but decrease towards starting values once plagioclase becomes stable. Ca remains relatively constant for much of the temperature interval investigated with the exception of the 1100°C experiment in which Ca increases by ~20%. Mg follows a depletion trend throughout the investigated temperature interval. The bulk liquid starts out hypersthene (*hy*)-normative but becomes nepheline (*ne*)-normative between 1200°C and 1150°C. The liquid remains *ne*-normative as crystallization proceeds.

The magmatic volatiles fluorine and chlorine increase incompatibly throughout the temperature interval investigated. Chlorine abundance was likely well below that needed to form either an immiscible chloride melt or a Cl-bearing fluid. Fluorine contents approached high values and loss of an F-rich fluid phase (while unlikely) could have occurred; therefore, the computed fluorine contents presented in Table 5.3 are upper limits.

5.3.2. "Wet" experiments

Experiments on the synthetic Humphrey mix under "wet" conditions at 9.3 kbar were conducted over the temperature interval 1250-980°C. The run products of the experiments contained variable amounts of mineral phases and glass. Micro-FTIR analysis of residual glass indicates a bulk (initial) water content of 1.67 wt%.

5.3.2.1. Mineral Phases

Compositions of mineral phases that formed during "wet" crystallization of Humphrey (Hsynth Wet) are presented in Tables 5.5 and 5.6. Figure 5.5 shows the computed phase abundances from these experiments. While Cr-spinel appears to be the liquidus phase, it is likely metastable as it formed during hydrous glass synthesis and, because of its refractory nature, did not dissolve during the experiments. Therefore, the liquidus is likely represented by the appearance of olivine at 1200°C (at which point Cr-spinel may also be stable). Orthopyroxene then appears at 1150°C, and at 1100°C orthopyroxene is replaced by pigeonite. Augite enters the assemblage at 1050°C, followed by amphibole at 1030°C. At 1000°C, augite is no longer present, and plagioclase and apatite appear. At 980°C olivine is no longer part of the assemblage.

Figure 5.6 shows olivine and pyroxene compositions projected into the pyroxene quadrilateral through QUILF (Andersen et al., 1993). Amphibole is also projected into the quadrilateral by summing the ternary components (Ca, Mg, and Fe) and normalizing to one atom. Projection of amphibole into the quadrilateral was necessary for understanding the evolution of the ferromagnesian mineral phases since augite and olivine were likely reacting with melt to form amphibole. Wo-components of pigeonite range from Wo_{13}-Wo_{18}, while the single orthopyroxene has Wo_4. Augite ranges from Wo_{23}-Wo_{29}, and amphibole ranges from "Wo_{21}-Wo_{23}." Olivine ranges in composition from Fo_{70}-Fo_{46}.

5.3.2.2. Liquid Evolution

Compositions of residual liquids are presented in Table 5.7. As seen in Figure 5.5, the liquidus for this composition at 9.3 kbar is > 1250°C; however, as discussed above, the apparent liquidus phase (Cr-spinel) is likely metastable, therefore the "true" (equilibrium) liquidus is likely closer to 1200°C. The solidus for this composition is < 980°C. Figure 5.7 illustrates the compositional evolution of residual liquids (Table 5.7) and bulk solids (Table 5.8) along the "wet" crystallization path. The residual liquids follow a silica-enrichment trend, which is coupled with strong alkali- and Al-enrichment and strong Mg- and Fe-depletion. Both Ca and Ti increase initially, but both elements are depleted beyond the starting values once augite and amphibole stabilize respectively. The residual liquid starts out *hy*-normative and remains so throughout the investigated temperature interval.

It has been our experience that once a water-rich fluid phase forms it escapes through the graphite capsule walls. The computed water values assume that formation and loss of a fluid phase did not occur; however, because fluid saturation may have been attained, the water contents presented in Table 5.7 are upper limits. Fluorine and chlorine increased incompatibly in the liquid until amphibole entered the assemblage at 1030°C; however, because chlorine is not easily incorporated into such amphiboles (Morrison, 1991), it continued to increase nearly incompatibly until apatite entered the assemblage at 1000°C. Neither fluorine nor chlorine reached abundances in the melt that were consistent with fluid saturation, nor were their abundances sufficient to greatly enhance formation of a water-rich fluid (i.e., Webster et al., 1999; Webster and Rebbert, 1998).

5.4. Discussion

5.4.1. Lithologic diversity on the Martian surface

Although traditionally petrologists ascribe variations in rock chemistry to different mantle compositions and/or different degrees of partial melting, the experiments reported here illustrate the great range in compositional diversity of lavas on the Martian surface that could arise simply from a single stage of fractional crystallization of a Humphrey-like basaltic magma at the base of a thick crust. As has been observed for terrestrial rocks, the nature of the fractionation-induced compositional diversity is dependent upon differences in the bulk water content of the parental magma. Figure 5.8 shows that liquids evolving along the "dry" path change from basalt to basanite (an alkalic *ne*-normative basalt) and become progressively lower in silica with increasing degrees of fractionation. This contrasts greatly with liquids evolving along the "wet" path which progress from basalt to trachyandesite (an alkali-rich andesite according to the LeBas classification (Lebas et al., 1986)). The opposing behavior of silica content with decreasing temperature in these two paths is perhaps most readily seen via the magnesium number (mg#) (Figure 5.9). Once Humphrey-like magmas evolve to a mg# of 30, "dry" liquids would have silica contents close to 42 wt% while those starting from a melt with a water content of 1.67 wt% would have silica contents of 51 wt%.

Importantly, evolution of "dry" magmas along the silica-depletion path is coupled with strong iron-enrichment of the residual liquids (Fig. 5.10). By the time ~90% fractionation has taken place, the residual liquid would have over 22 wt% total iron. In

contrast, the wetter starting material undergoing the same degree of fractionation would be depleted in total iron to a value below 12 wt%.

The evolution of Humphrey along the "wet" or "dry" paths also has implications for the Al/Si ratio of the lavas representing liquids residual to deep fractionation. The Al/Si vs. Mg/Si ratios of the residual liquids for the "wet" Humphrey compositions evolve in a similar fashion to terrestrial olivine tholeiite, increasing at low degrees of fractionation before decreasing at the later stages (Fig. 5.11). These general characteristics also hold true for the "dry" path, but it shows more restricted variability in Mg/Si ratio. This trend shows that residual liquids evolving along both the "wet" and "dry" paths have higher Al/Si ratios than their respective parental liquids for any given degree of fractionation; therefore, Al/Si ratios of fractionally crystallized lavas on the Martian surface will have higher Al/Si ratios than those of their parental liquids.

5.4.2. Lithologic diversity at the base of the Martian crust

The variability in the surface lavas that arise from deep fractionation as a function of water content is also mirrored by variability in the nature of the cumulate lithologies left behind in the lower crust. The cumulate lithologies (represented by the bulk solids for each experiment) for both the "wet" and "dry" paths range from ultramafic to mafic in composition; however, the "wet" path crosses over from ultramafic to mafic (at the onset of feldspar crystallization) at a much higher degree of fractionation (~75%) than along the "dry" path (~45%) (Fig. 5.12). The mg#'s of the residual solids start out at ~70 and 68 for the "wet" and "dry" paths, respectively, and steadily decrease towards the bulk mg# with increasing degrees of fractionation. The rocktypes added to the base of the martian crust via fractionation of a Humphrey-like primary magma are highly dependent on both the bulk starting water content of the parental melt and the extent of crystallization prior to liquid separation. Figure 5.12 shows the relationship between degree of fractionation and the nature of the lithology added to the base of the martian crust for both the "dry" and "wet" paths (Fig. 5.12A and B, respectively). The rocktypes indicated in Figure 5.12 represent the bulk modal mineralogy; they do not preclude the formation of monomineralic cumulus layering within the deep magma chambers.

5.4.3. Time-dependent stratification in the upper and lower martian crust

The earliest post-magma ocean magmatism on Mars is likely represented by the most hydrous magmatism because any water remaining in the depleted mantle would partition strongly into melt. Without a mechanism for re-hydration (i.e., plate subduction), continued tapping of the same mantle source would result in a general dehydration trend in the magmas as the water is depleted in the source region upon repeated melt generation. Because of the major differences in liquid-line-of-descent between "wet" versus "dry" parental liquids, there could have been a dramatic shift in surface lithology compositions over time. This implies that any lithologies on the Martian surface today that are the product of fractional crystallization are more likely to represent lithologies along the "dry" trend, which means that the current Martian surface is more likely composed of basaltic to basanitic lithologies, which is consistent with mission-based observations of the martian surface. Importantly, this does not preclude the existence of silica-rich lithologies below the surface, especially if Mars had a wet mantle early in its history. The relative thicknesses of the "wet-path" layer versus the "dry-path" layer would largely be a function of the water budget of the mantle at the respective mantle source and the degree of crystallization that took place before residual liquid separation.

The lower martian crust would also undergo stratification because of the change in water budget over time. During the period of extensive hydrous magmatism, ultramafic rocks are likely added to the base of the crust, and, if sufficient fractionation took place before residual liquid separation, amphibole will be present in the lower crust. This amphibole could undergo dehydration melting upon the passage of younger, hotter, drier magmas and contribute Ca-Mg-Ti-rich hydrous melt to the surface or subsurface. The youngest portion of the lower crust, represented by the residual solids produced during fractionation of "dry" magmas, would likely be a mixture of mafic and ultramafic material, and instead of amphibole, plagioclase would be present if sufficient crystallization occurred prior to loss of residual liquid.

The results of these experiments suggest that if drier magmas dominated the latest stages of magmatic activity of the planet, the present-day surface would be characterized by high Fe and low silica basaltic compositions. These compositions would be evolved with low mg#'s and would not reflect primary magmas or source regions with similarly

low mg#'s. The variability in Al/Si ratio, iron-content, and silica-content of the evolving liquids during deep-seated fractionation points out the potential problems of using compositional data from surface rocks to access information about primitive liquid compositions and magmatic source regions. Such information may be further obscured by additional processes such as wallrock assimilation and mixing with the products of dehydration melting as the residual liquids ascend towards the surface.

5.5. Acknowledgments

We thank Dr. Charles Mandeville of the American Museum of Natural History for hours of assistance in using both the electron microprobe and the micro-FTIR instrument. Financial support for this work was provided by NASA grant NNG04GM79G from the Mars Fundamental Research Program, awarded to Hanna Nekvasil, and Francis McCubbin was partially supported by a Graduate Assistance in Areas of National Need (GAANN) Fellowship.

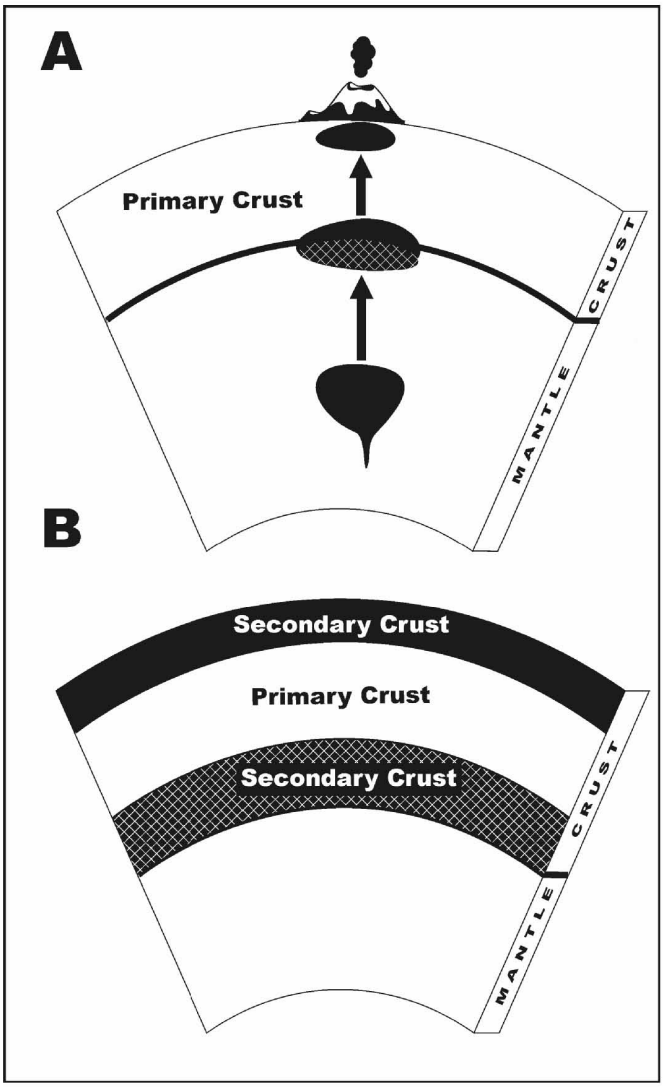

Figure 5.1. Schematic illustrating the process of single-stage fractional crystallization at the base of a thick crust in which liquids residual to fractionation ascend to the surface or subsurface (A). The residual liquids become part of the secondary, post-magma-ocean upper crust, while the cumulus minerals left at depth contribute to the formation of a deep, dense secondary lower crust (B.)

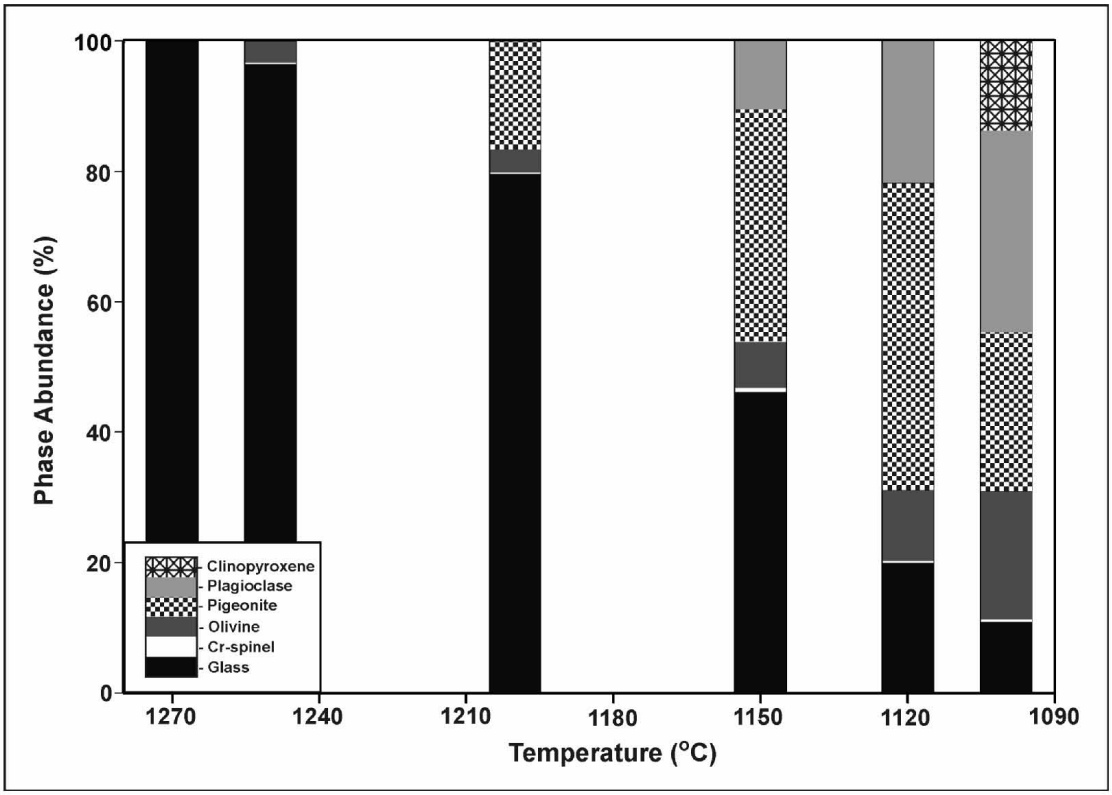

Figure 5.2. Abundances of phases formed in crystallization experiments on Humphrey composition liquid with 0.07 wt% bulk water at 9.3 kbar. Abundances were calculated using the least squares mass balance routine of the IgPet software suite (CARR, 2002).

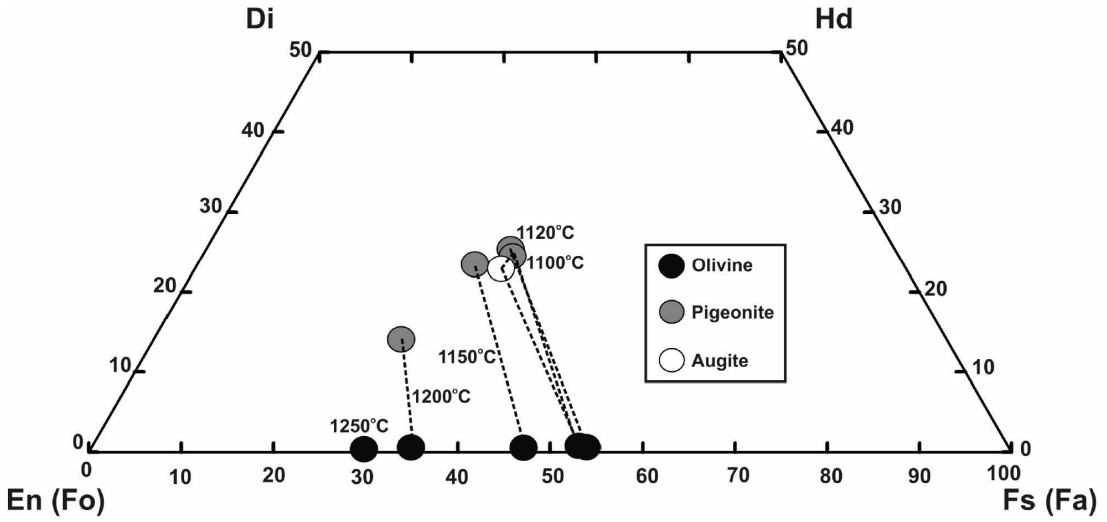

Figure 5.3. Projected compositions of ferromagnesian phases crystallized from experiments on Humphrey with 0.07 wt% bulk water. Phases plotted using the projection scheme of the program QUILF (ANDERSEN et al., 1993). Dashed lines connect phases co-existing at the indicated temperatures. See text for explanation of apparent inconsistencies between augite and pigeonite compositions.

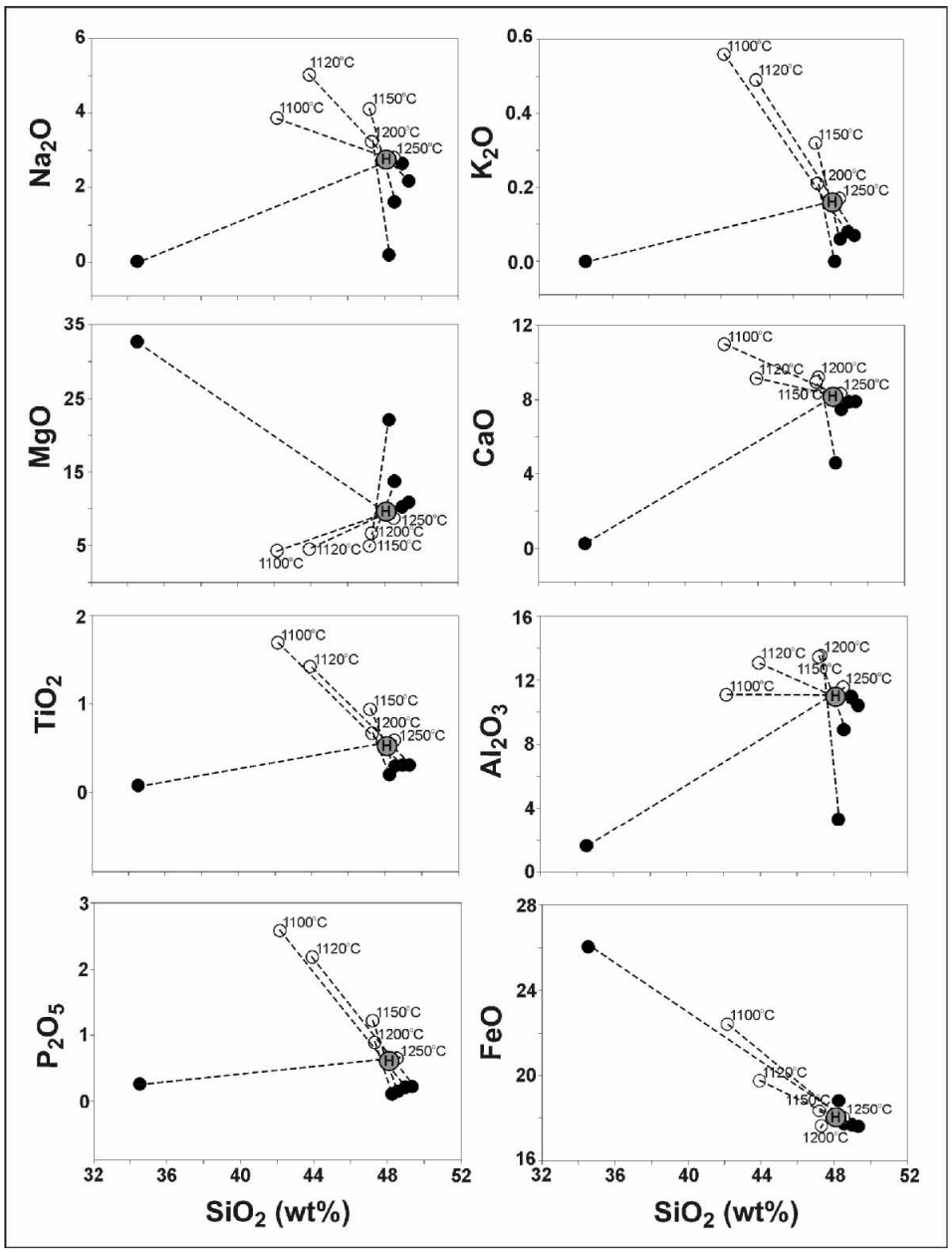

Figure 5.4. Harker-variation diagram for residual liquids (open circles) and bulk solids (black circles) from experiments on Humphrey (H) with 0.07 wt% bulk water at 9.3 kbar. Coexisting phases at each temperature are connected by dashed lines.

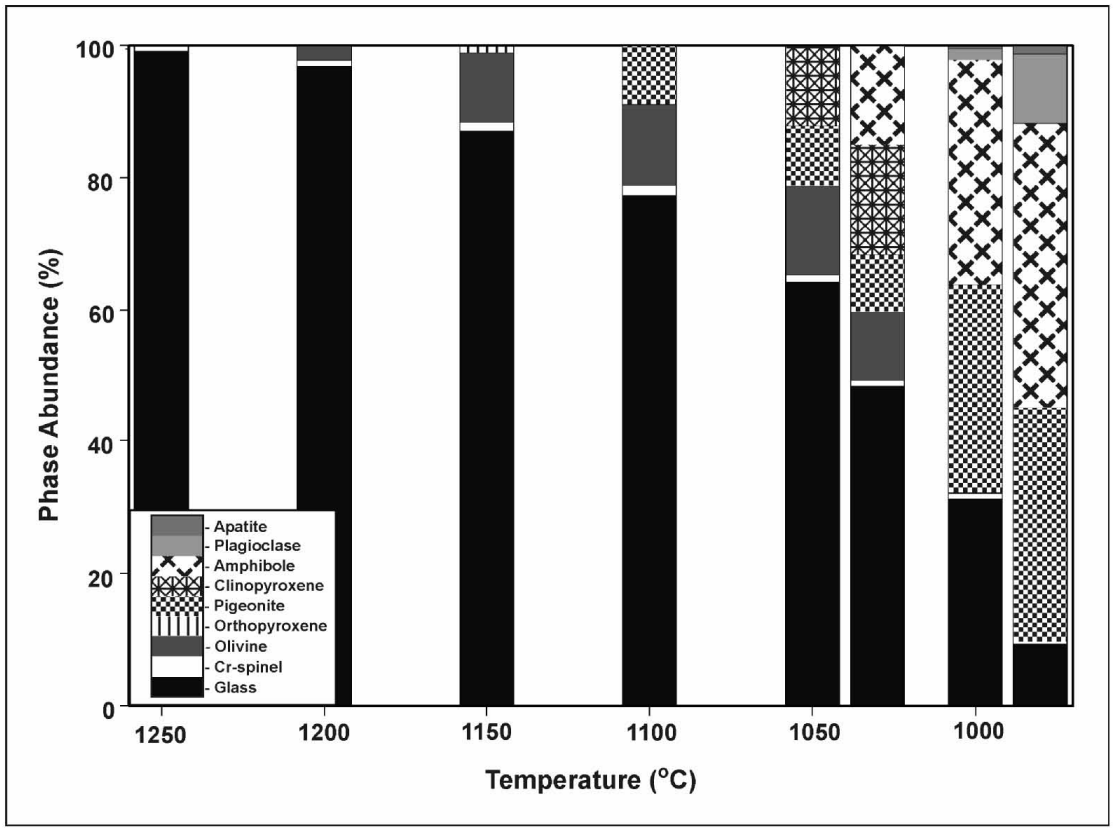

Figure 5.5. Abundances of phases formed in crystallization experiments on Humphrey composition liquid with 1.67 wt% bulk water at 9.3 kbar. Abundances were calculated using the least squares mass balance routine of the IgPet software suite (CARR, 2002).

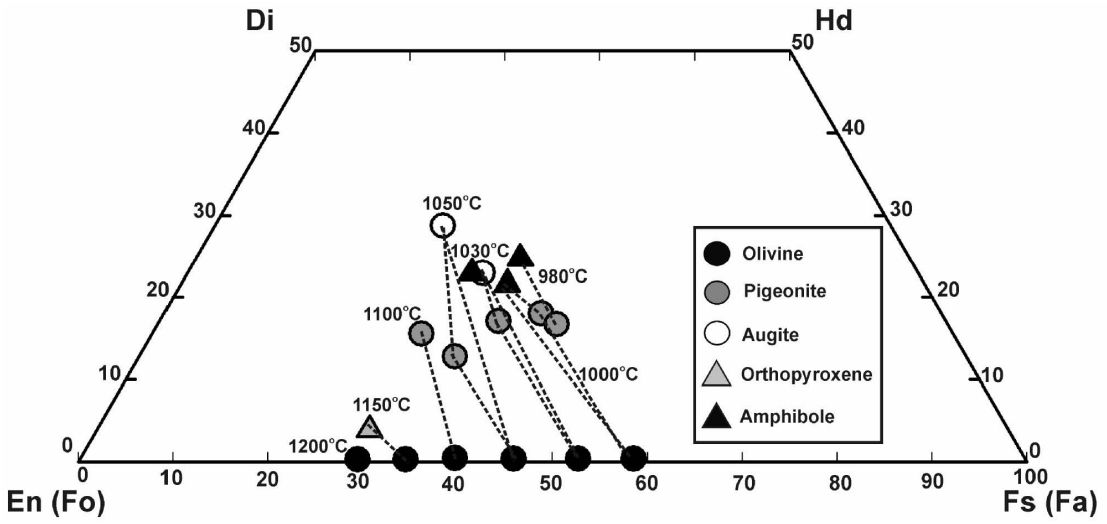

Figure 5.6. Projected compositions of ferromagnesian phases crystallized from experiments on Humphrey with 1.67 wt% bulk water at 9.3 kbar. Pyroxene and olivine compositions plotted using the projection scheme of the program QUILF (ANDERSEN et al., 1993). For amphiboles, Ca + Mg + Fe were normalized to one atom. Dashed lines connect phases co-existing at the indicated temperatures.

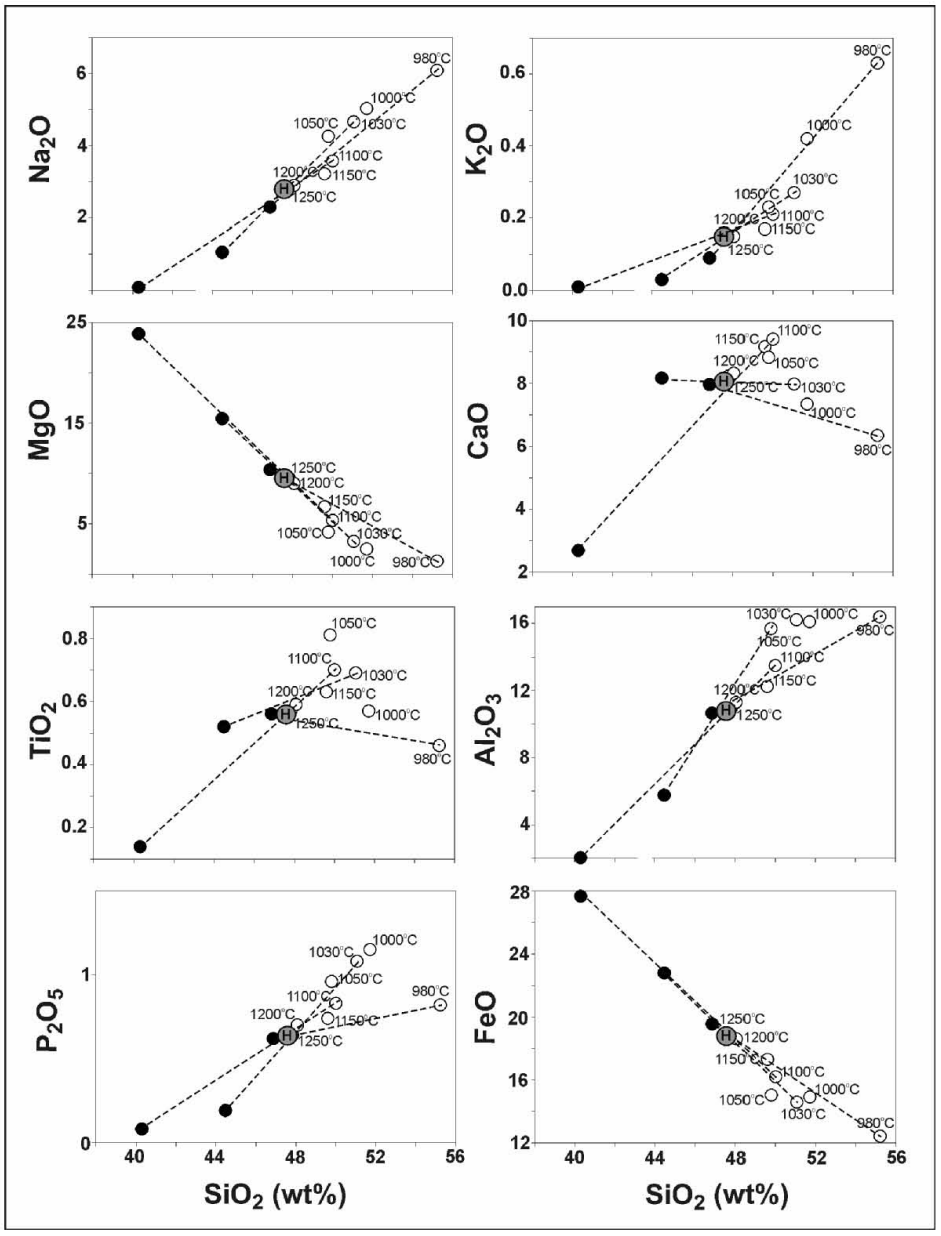

Figure 5.7. Harker-variation diagram for residual liquids (open circles) and bulk solids (black circles) from experiments on Humphrey (H) with 1.67 wt% BULK WATER at 9.3 kbar. Coexisting phases at each temperature are connected by dashed lines.

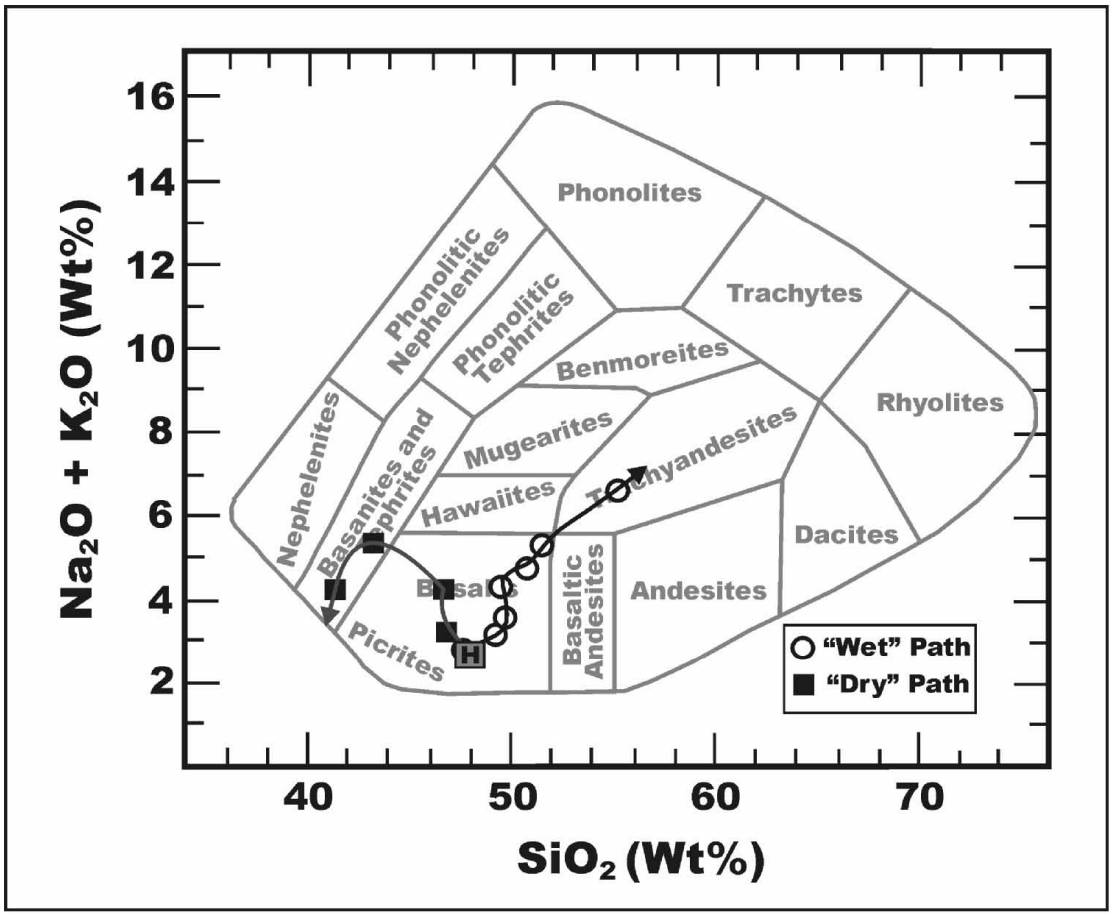

Figure 5.8. Variation in total alkalis vs. silica in experimental residual liquids produced from Humphrey composition (H) liquid at 9.3 kbar under both "dry" (0.07 wt% bulk water; black squares) and "wet" (1.67 wt% bulk water; open circles) conditions. Arrows indicate the down-temperature direction. The rock classification scheme of Cox et al. (1984) is shown in the background.

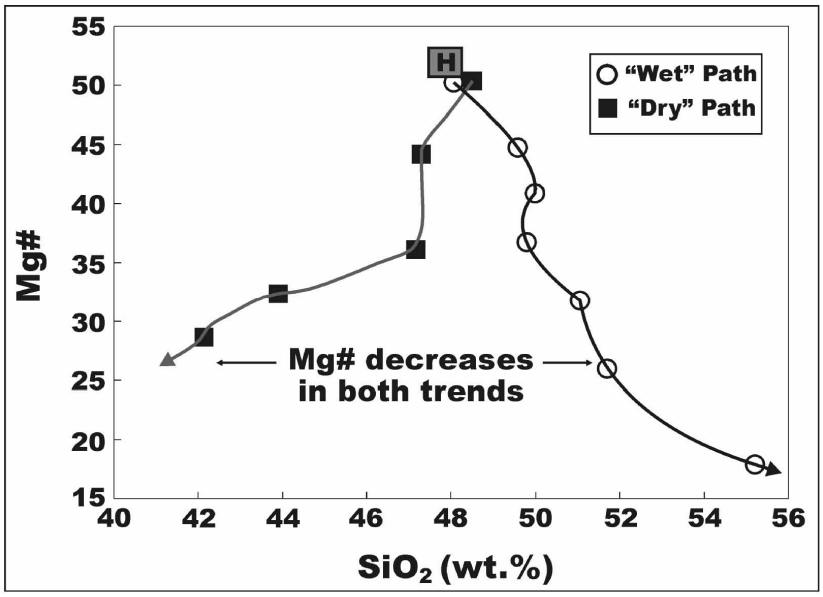

Figure 5.9. Variation in mg# (as defined in Tables 5.3 & 5.7) vs. silica in experimental residual liquids produced from Humphrey composition (H) liquid at 9.3 kbar under both "dry" (0.07 wt% bulk water; black squares) and "wet" (1.67 wt% bulk water; open circles) conditions. Arrows indicate the down-temperature direction.

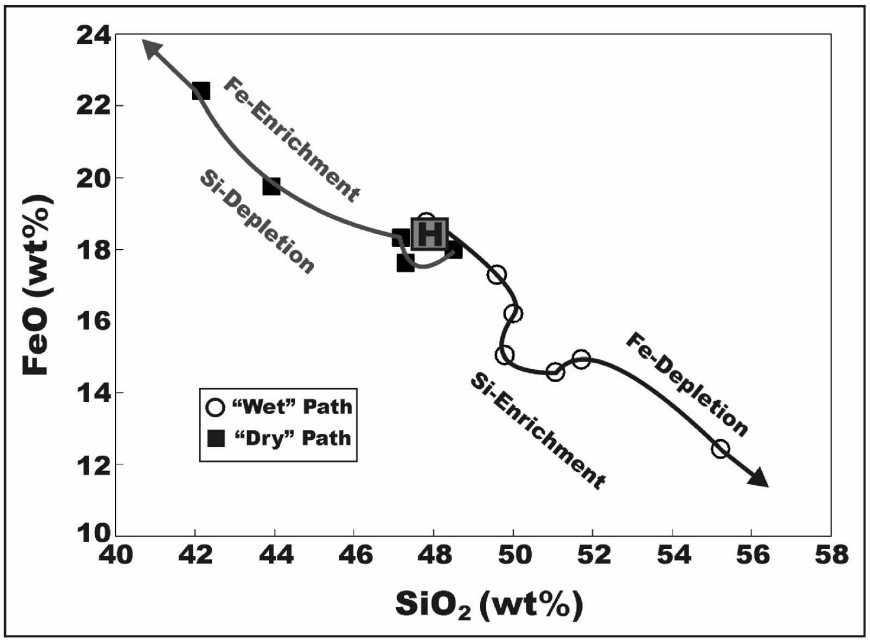

Figure 5.10. Variation in total iron (as FeO_T) vs. silica in experimental residual liquids produced from Humphrey composition (H) liquid at 9.3 kbar under both "dry" (0.07 wt% bulk water; black squares) and "wet" (1.67 wt% bulk water; open circles) conditions. Arrows indicate the down-temperature direction.

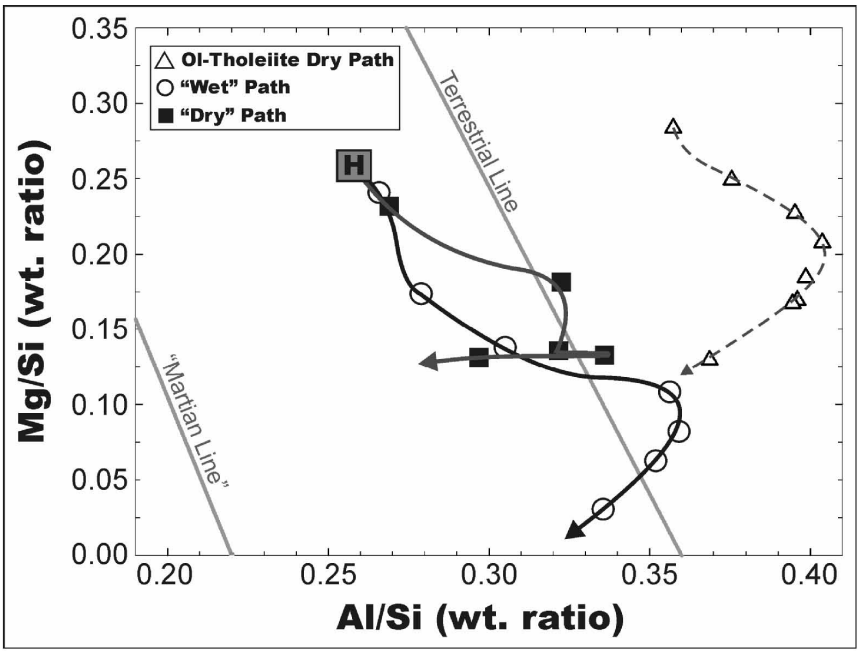

Figure 5.11. Mg/Si vs. Al/Si weight ratios of experimental residual liquids (adopted from Filiberto et al. (2006) produced from Humphrey composition (H) liquid at 9.3 kbar under both "dry" (0.07 wt% bulk water; black squares) and "wet" (1.67 wt% bulk water; open circles) conditions. Arrows indicate the down-temperature direction. Residual liquids from crystallization of a terrestrial olivine tholeiite (open triangles) with 0.05 wt% bulk water and at 9.3 kbar pressure are shown for comparison. The geochemical fractionation line of Jagoutz et al. (1979) for Earth and from Wänke et al. (1986) for Mars are also shown for comparison.

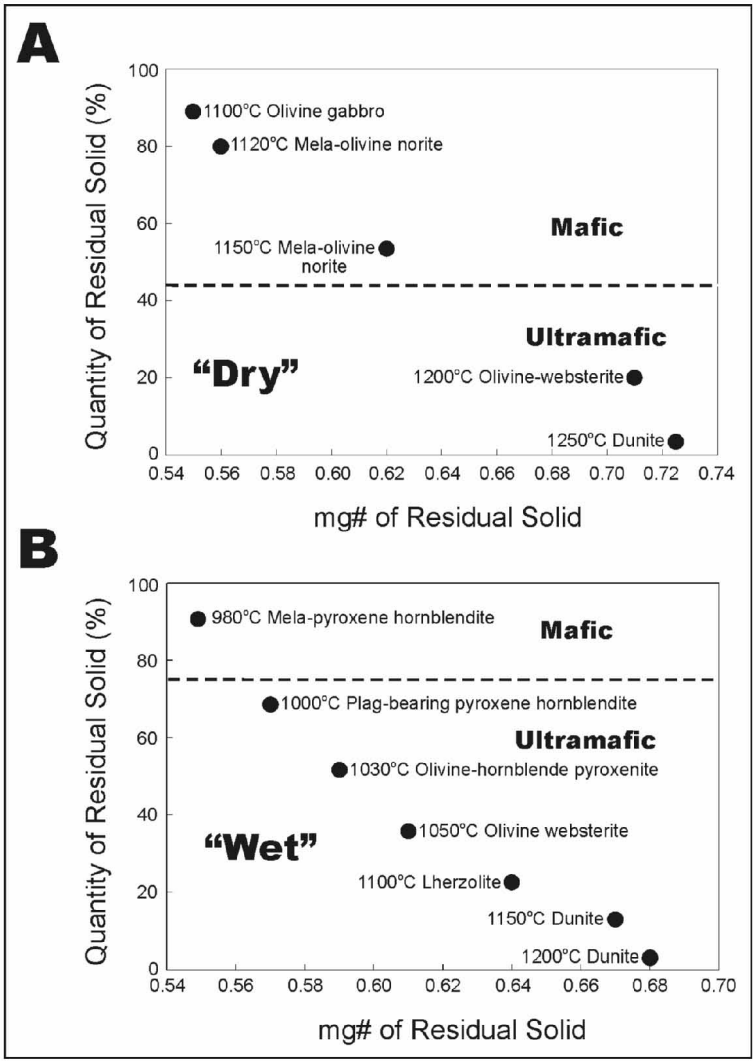

Figure 5.12. Abundance of residual solid (wt% of system, where the system consists of residual liquid + crystallized solid) vs. bulk mg# of the residual solids from experiments on the Humphrey composition at 9.3 kbar. Rock names are from the IUGS classification of ultramafic rocks and gabbroic rocks. (Pigeonite was recast into 2/3 orthopyroxene and 1/3 augite.) Boundaries (dashed lines) between mafic and ultramafic cumulate lithologies were placed where the cumulus assemblage was estimated to contain 10 modal % plagioclase. Rock types were determined from the mineral modes in tables 5.3 and 5.7. (A) For experiments conducted with 0.07 wt% bulk water. (B) For experiments conducted with 1.67 wt% bulk water.

Table 5.1. Published Humphrey compositions and synthetic compositions used in this study

Oxide	Hbrush*	HRAT 1*	HRAT 2*	Hsynth Dry‡	Hsynth Wet‡
SiO_2	45.9	46.3	45.9	47.7	45.8
TiO_2	0.54	0.58	0.55	0.53	0.54
Al_2O_3	11.2	10.8	10.7	10.9	10.4
Cr_2O_3	0.60	0.68	0.60	0.67	0.63
FeO	17.9	18.6	18.8	17.9	18.1
MgO	8.82	9.49	10.4	9.57	9.19
CaO	7.76	8.19	7.84	8.09	7.77
Na_2O	3.00	2.80	2.50	2.72	2.70
K_2O	0.18	0.13	0.10	0.16	0.14
MnO	0.39	0.41	0.41	0.38	0.41
P_2O_5	0.62	0.57	0.56	0.61	0.62
F	*n.d.*	*n.d.*	*n.d.*	0.56	0.55
Cl	0.62	0.57	0.56	0.15	0.21
-O = F + Cl	0.11	0.07	0.06	0.27	0.28
Total	97.4	99.1	98.9	99.7	96.8
mg#[a]	0.51	0.52	0.54	0.53	0.52
H_2O in synthetic glass (wt. %)				0.07[b]	1.67[b]

* Gellert et al. [*2006*]

‡ Synthetic composition used for this study

[a] mg# = Molar Mg/(Mg + Fe^{2+}) assuming an Fe^{2+}/Fe_{Tot} ratio of 0.85.

[b] Measured by FTIR (not included in total).

Table 5.2. Mineral phase compositions from experiments on Hsynth Dry (0.07 wt. % bulk H_2O[a]) at 9.3 kbar

Phase	Cr-Spinel					Olivine
Experiment	3.025	3.008	3.009	3.011	3.010	3.025
Temperature (°C)	1250	1200	1150	1120	1100	1250
SiO_2	0.00	0.00	0.00	0.00	0.00	37.0
TiO_2	0.77	0.94	1.91	2.12	3.23	0.02
Al_2O_3	19.8	22.3	20.5	27.6	20.2	0.07
Cr_2O_3	45.1	44.00	40.4	31.7	35.1	0.60
FeO	23.1	24.7	28.6	31.8	32.7	25.9
MnO	0.15	0.14	0.22	0.17	0.21	0.29
MgO	8.42	7.59	5.25	5.09	4.19	34.3
CaO	0.11	0.25	0.23	0.16	0.29	0.27
Na_2O	0.05	0.03	0.05	0.03	0.01	0.03
K_2O	0.01	0.01	0.03	0.03	0.01	0.00
P_2O_5	0.01	0.02	0.02	0.04	0.01	0.27
Total	98.6	100.0	97.2	98.7	96.0	98.7
Phase Comp. (mol %)	$Ul_2Mt_1Cr_{58}Hy_{38}$	$Ul_2Mt_0Cr_{56}Hy_{42}$	$Ul_3Mt_1Cr_{54}Hy_{41}$	$Ul_5Mt_2Cr_{40}Hy_{52}$	$Ul_8Mt_4Cr_{47}Hy_{41}$	$Fo_{70}(La_{0.39})$

Phase	Olivine				Pigeonite	
Experiment	3.008	3.009	3.011	3.010	3.008	3.009
Temperature (°C)	1200	1150	1120	1100	1200	1150
SiO_2	36.4	34.3	34.2	33.9	50.4	48.8
TiO_2	0.03	0.05	0.05	0.06	0.22	0.39
Al_2O_3	0.06	0.08	0.05	0.06	3.68	5.20
Cr_2O_3	0.29	0.19	0.12	0.19	1.63	0.76
FeO	29.9	39.2	43.8	42.7	16.1	17.9
MnO	0.50	0.47	0.41	0.41	0.51	0.48
MgO	31.4	24.7	20.9	21.0	19.9	15.4
CaO	0.42	0.37	0.41	0.44	5.44	8.45
Na_2O	0.03	0.08	0.05	0.03	0.23	0.54
K_2O	0.01	0.03	0.01	0.00	0.00	0.03
P_2O_5	0.09	0.11	0.22	0.16	0.11	0.14
Total	99.1	99.6	100.2	98.9	98.2	98.1
Phase Comp. (mol %)	$Fo_{65}(La_{0.62})$	$Fo_{53}(La_{0.56})$	$Fo_{46}(La_{0.64})$	$Fo_{46}(La_{0.71})$	$En_{39}Wo_{14}$	$En_{47}Wo_{23}$

Phase	Pigeonite		Plagioclase			Augite
Experiment	3.011	3.010	3.009	3.011	3.010	3.010
Temperature (°C)	1120	1100	1150	1120	1100	1100
SiO_2	49.1	49.7	57.3	57.4	59.3	45.9
TiO_2	0.48	0.47	0.04	0.05	0.05	0.87
Al_2O_3	5.51	2.58	26.5	25.6	25.9	8.06
Cr_2O_3	1.13	0.84	0.05	0.02	0.00	2.10
FeO	19.2	20.1	0.43	0.67	0.60	14.1
MnO	0.31	0.34	0.03	0.01	0.01	0.27
MgO	13.6	13.9	0.09	0.06	0.08	10.4
CaO	9.55	9.95	8.95	8.06	7.75	15.0
Na_2O	0.55	0.33	6.44* (6.13)	6.75* (6.38)	7.20* (6.95)	0.58
K_2O	0.01	0.00	0.16	0.22	0.24	0.00
P_2O_5	0.26	0.13	0.21	0.16	0.15	0.55
Total	99.7	98.3	100.2	99.0	101.3	97.8
Phase Comp. (mol %)	$En_{42}Wo_{25}$	$En_{42}Wo_{25}$	$An_{42}(Or_1)$	$An_{38}(Or_1)$	$An_{36}(Or_1)$	$En_{44}Wo_{23}$

[a] measured by FTIR.

* Value corrected for Na-loss; measured value listed parenthetically

Table 5.3. Residual liquid compositions from experiments on Hsynth Dry (0.07 wt. % bulk H_2O^a) at 9.3 kbar

Experiment (No.)	3.025	3.008	3.009	3.011	3.010
Mode (wt%)	Gl 96.5, Ol 3.2, Sp 0.3	Gl 79.7, Ol 3.5, Sp 0.2, Pig 16.6	Gl 46.3, Ol 7.0, Sp 0.7, Pig 35.6, Pl 10.4,	Gl 20.0, Ol 10.8, Sp 0.4, Pig 47.1, Pl 21.7	Gl 10.9, Ol 19.7, Sp 0.4, Pig 24.4, Pl 30.9, Cpx 13.7
Temperature (°C)	1250	1200	1150	1120	1100
SiO_2	47.5	46.2	45.2	42.8	40.2
TiO_2	0.57	0.65	0.90	1.38	1.62
Al_2O_3	11.3	13.2	12.9	12.7	10.6
Cr_2O_3	0.46	0.26	0.15	0.10	0.08
FeO	17.6	17.2	17.6	19.3	21.4
MnO	0.21	0.41	0.36	0.40	0.27
MgO	8.53	6.67	4.75	4.40	4.10
CaO	8.15	9.21	8.58	8.91	10.5
Na_2O^*	2.76	*n.c.*	*n.c.*	4.90	*n.c.*
Na_2O	2.38	3.16	3.94	3.69	3.69
K_2O	0.17[b]	0.21[b]	0.31	0.48	0.54
P_2O_5	0.64	0.89	1.17	2.12	2.46
F[b]	0.58	0.70	1.21	2.80	5.14
Cl[b]	0.16	0.19	0.32	0.75	1.38
-O = F + Cl	0.28	0.34	0.58	1.35	2.48
Total	98.4	98.6	96.8	99.7	99.5
mg#	0.50	0.44	0.36	0.32	0.29
H_2O in Glass (wt. %)[b]	0.07	0.09	0.15	0.35	0.64
Crystallinity (wt. %)	3.5	20.2	53.6	80.0	89.1
S.S.R.	0.13	0.20	0.01	0.02	0.06

* Value corrected for Na-loss

[a] measured by FTIR.

[b] calculated based on degree of crystallinity assuming component increases incompatibly (H_2O value not included in total).

mg# = Molar Mg/(Mg + Fe^{2+}) assuming an Fe^{2+}/Fe_{Tot} ratio of 0.85.

Table 5.4. Computed[†] bulk residual solid compositions from experiments on Hsynth Dry (0.07 wt. % bulk H_2O[a]) at 9.3 kbar

Experiment (No.)	3.025	3.008	3.009	3.011	3.010
Temperature (°C)	1250	1200	1150	1120	1100
SiO_2	34.5	48.2	48.5	49.3	49.0
TiO_2	0.08	0.20	0.30	0.31	0.31
Al_2O_3	1.65	3.32	8.91	10.4	11.0
Cr_2O_3	4.17	1.89	1.09	0.85	0.75
FeO	26.0	18.8	17.7	17.6	17.7
MnO	0.28	0.51	0.39	0.24	0.23
MgO	32.7	22.1	13.7	10.9	10.3
CaO	0.26	4.60	7.48	7.91	7.89
Na_2O	0.03	0.20	1.62[*]	2.18[*]	2.65[*]
K_2O	0.00	0.00	0.06	0.07	0.08
P_2O_5	0.26	0.11	0.15	0.22	0.21
Total	99.9	99.9	99.9	100.0	100.1
mg#	0.73	0.71	0.62	0.56	0.55

[†] Computed from phase abundances

[*] Value calculated from plagioclase that was corrected for Na-loss

[a] measured by FTIR.

mg# = Molar Mg/(Mg + Fe^{2+}) assuming an Fe^{2+}/Fe_{Tot} ratio of 0.85.

Table 5.5. Compositions of silicate minerals from experiments on Hsynth Wet (1.67 wt% bulk H_2O^a) at 9.3 kbar

Phase	Olivine					
Experiment	3.029	3.022	3.023	3.027	3.028	3.030
Temperature (°C)	1200	1150	1100	1050	1030	1000
SiO_2	37.6	37.5	36.4	35.1	34.9	33.3
TiO_2	0.02	0.01	0.02	0.00	0.01	0.04
Al_2O_3	0.05	0.02	0.03	0.01	0.01	0.02
Cr_2O_3	0.14	0.09	0.12	0.09	0.06	0.02
FeO	26.4	30.5	34.0	38.3	42.9	46.8
MnO	0.30	0.52	0.31	0.40	0.40	0.40
MgO	35.6	32.6	29.0	25.4	21.6	18.6
CaO	0.21	0.19	0.31	0.22	0.24	0.21
Na_2O	0.00	0.00	0.02	0.01	0.02	0.02
K_2O	0.01	0.00	0.01	0.00	0.00	0.02
P_2O_5	0.05	0.05	0.06	0.08	0.19	0.10
Total	100.4	101.5	100.3	99.6	100.3	99.5
Phase Comp. (mol %)	$Fo_{70}(La_{0.30})$	$Fo_{65}(La_{0.28})$	$Fo_{60}(La_{0.46})$	$Fo_{54}(La_{0.34})$	$Fo_{47}(La_{0.38})$	$Fo_{46}(La_{0.71})$

Phase	Orthopyroxene	Pigeonite	Pigeonite			
Experiment	3.022	3.023	3.027	3.028	3.030	3.032
Temperature (°C)	1150	1100	1050	1030	1000	980
SiO_2	52.9	52.0	51.1	50.7	49.8	49.5
TiO_2	0.10	0.12	0.20	0.28	0.14	0.05
Al_2O_3	1.93	2.37	2.85	3.82	2.82	2.63
Cr_2O_3	0.79	0.65	0.58	0.45	0.34	0.31
FeO	18.0	18.3	20.3	21.6	24.7	26.7
MnO	0.28	0.37	0.38	0.34	0.45	0.64
MgO	23.6	19.7	18.5	16.0	14.2	13.6
CaO	1.86	6.33	5.12	6.93	6.85	5.22
Na_2O	0.07	0.20	0.16	0.24	0.26	0.21
K_2O	0.00	0.00	0.00	0.01	0.01	0.01
P_2O_5	0.02	0.11	0.10	0.14	0.17	0.08
Total	99.6	100.2	99.3	100.5	99.7	99.0
Phase Comp. (mol %)	$En_{67}Wo_4$	$En_{56}Wo_{16}$	$En_{54}Wo_{13}$	$En_{47}Wo_{17}$	$En_{42}Wo_{18}$	$En_{42}Wo_{17}$

Phase	Augite		Plagioclase		Spinel	
Experiment	3.027	3.028	3.030	3.032	3.026	3.029
Temperature (°C)	1050	1030	1000	980	1250	1200
SiO_2	50.1	50.5	56.6	58.0	0.00	0.00
TiO_2	0.25	0.29	0.02	0.04	0.45	0.41
Al_2O_3	3.32	3.82	27.9	27.1	9.14	9.85
Cr_2O_3	0.82	0.63	0.00	0.01	56.0	53.3
FeO	14.1	16.9	0.85	0.83	25.6	26.3
MnO	0.27	0.29	0.01	0.00	0.19	0.18
MgO	14.2	13.9	0.05	0.02	7.02	6.90
CaO	15.6	13.1	9.65	8.63	0.25	0.21
Na_2O	0.38	0.40	5.99	7.12* (6.83)	0.04	0.03
K_2O	0.00	0.00	0.07	0.07	0.00	0.01
P_2O_5	0.25	0.21	0.15	0.17	0.02	0.05
Total	99.3	100.0	101.3	102.0	98.7	97.3
Phase Comp. (mol %)	$En_{47}Wo_{29}$	$En_{46}Wo_{23}$	$An_{46}(Or_{0.4})$	$An_{41}(Or_{0.4})$	$Ul_1Mt_4Cr_{76}Hy_{18}$	$Ul_1Mt_5Cr_{73}Hy_{20}$

[a] measured by FTIR.

* Value corrected for Na-loss; measured value listed parenthetically

Table 5.5. contd.: Compositions of silicate minerals from experiments on Hsynth Wet (1.67 wt% bulk H_2O[a]) at 9.3 kbar

Phase	**Spinel**					
Experiment	3.022	3.023	3.027	3.028	3.030	3.032
Temperature (°C)	1150	1100	1050	1030	1000	980
SiO_2	0.00	0.00	0.00	0.00	0.00	0.00
TiO_2	1.19	1.33	1.03	0.48	0.41	0.40
Al_2O_3	16.4	17.4	15.3	10.1	9.02	8.78
Cr_2O_3	43.2	40.4	41.8	52.8	51.5	51.7
FeO	29.7	31.9	31.4	30.7	31.5	30.8
MnO	0.20	0.20	0.23	0.17	0.32	0.38
MgO	6.37	5.63	4.35	3.35	3.15	2.76
CaO	0.20	0.28	0.29	0.21	0.23	0.12
Na_2O	0.00	0.04	0.04	0.02	0.02	0.03
K_2O	0.01	0.00	0.00	0.00	0.00	0.01
P_2O_5	0.01	0.00	0.03	0.00	0.00	0.02
Total	97.3	97.2	94.5	97.8	96.2	95.0
Phase Comp. (mol %)	$Ul_3Mt_7Cr_{58}Hy_{33}$	$Ul_3Mt_8Cr_{54}Hy_{35}$	$Ul_3Mt_7Cr_{58}Hy_{32}$	$Ul_1Mt_4Cr_{74}Hy_{21}$	$Ul_1Mt_6Cr_{74}Hy_{19}$	$Ul_1Mt_5Cr_{75}Hy_{19}$

[a] measured by FTIR.

Table 5.6. Compositions of oxide and phosphate minerals from experiments on Hsynth Wet (1.67 wt% bulk H_2O[a]) at 9.3 kbar

Phase	**Amphibole**			**Apatite**	
Experiment	3.028	3.030	3.032	3.030	3.032
Temperature (°C)	1030	1000	980	1000	980
SiO_2	43.1	42.6	42.1	0.31	0.50
TiO_2	1.23	1.18	1.09	*n.d.*	*n.d.*
Al_2O_3	13.4	11.7	12.5	*n.d.*	*n.d.*
Cr_2O_3	0.61	0.24	0.54	*n.d.*	*n.d.*
FeO	15.1	17.3	17.3	1.20	1.59
MnO	0.36	0.27	0.29	*n.d.*	*n.d.*
MgO	13.3	12.4	11.6	*n.d.*	*n.d.*
CaO	8.97	8.47	9.72	53.7	53.8
Na_2O	3.42	2.82	2.72	0.08	0.01
K_2O	0.08	0.14	0.11	*n.d.*	*n.d.*
P_2O_5	0.02	0.03	0.06	41.6	41.1
F	1.45	1.42	1.10	2.85	3.13
Cl	0.06	0.07	0.08	0.40	0.59
-O = F + Cl	0.62	0.61	0.48	1.29	1.45
Total	100.5	98.0	98.8	98.0	99.3
Phase Comp. (mol %)	$En_{47}Wo_{23}$	$En_{44}Wo_{22}$	$En_{41}Wo_{25}$	$F_{0.77}Cl_{0.13}$	$F_{0.84}Cl_{0.19}$
H_2O Wt%[b]	1.40	1.36	1.44	0.18	0.00

[a] measured by FTIR.

[b] Calculated assuming only F, Cl, and OH populate the volatile sites.

Table 5.7. Residual liquid compositions from experiments on Hsynth Wet (with 1.67 wt. % bulk H_2O[a]) at 9.3 kbar

Experiment (No.)	3.026	3.029	3.022	3.023	3.027	3.028	3.030	3.032
Mode (wt%)	Gl 99.2, Sp 0.8	Gl 96.9, Sp 0.9, Ol 2.2	Gl 87.1, Sp 1.3, Ol 10.5, Opx 1.1	Gl 77.4, Sp 1.4, Ol 12.3, Pig 8.9	Gl 64.3, Sp 1.1, Ol 13.4, Pig 9.1, Cpx 12.1	Gl 48.6, Sp 0.8, Ol 11.0, Pig 7.2, Cpx 18.6, Amph 13.9	Gl 30.4, Sp 0.9, Ol 1.1, Pig 29.6, Amph 34.0, Plag 3.2, Ap 0.8	Gl 9.4, Sp 0.3, Pig 35.5, Amph 43.1, Plag 10.4, Ap 1.3
Temperature (°C)	1250	1200	1150	1100	1050	1030	1000	980
SiO_2	46.3	45.0	47.6	48.5	47.8	48.7	49.4	53.3
TiO_2	0.55	0.56	0.61	0.68	0.78	0.66	0.54	0.44
Al_2O_3	10.6	10.6	11.8	13.1	15.1	15.5	15.4	15.8
Cr_2O_3	0.22	0.10	0.06	0.04	0.02	0.04	0.05	0.05
FeO	18.2	17.4	16.6	15.7	14.5	13.9	14.3	12.0
MnO	0.27	0.25	0.22	0.20	0.19	0.15	0.19	0.26
MgO	9.24	8.40	6.41	5.19	4.02	3.09	2.39	1.25
CaO	7.98	7.79	8.81	9.13	8.49	7.62	7.02	6.13
Na_2O^*	2.73	2.70	3.08	3.46	4.09	4.44	4.80	5.88
Na_2O	2.51	2.54	2.87	3.20	3.49	3.62	4.20	4.53
K_2O	0.15	0.14	0.17	0.20	0.22	0.26	0.40	0.61
P_2O_5	0.62	0.65	0.71	0.81	0.92	1.03	1.10	0.79
F	0.55[b]	0.57[b]	0.63[b]	0.71[b]	0.86[b]	0.80	0.81	0.52
Cl	0.21[b]	0.22[b]	0.24[b]	0.27[b]	0.33[b]	0.44	0.74	1.22
-O = F + Cl	0.10	0.29	0.32	0.36	0.43	0.44	0.51	0.49
Total	97.3	94.1	96.6	97.6	96.9	96.2	96.6	97.8
mg#	0.52	0.50	0.45	0.41	0.37	0.32	0.26	0.18
H_2O in Glass (wt. %)[b]	1.68	1.72	1.92	2.15	2.60	3.26	4.85	10.0
Crystallinity (wt. %)	0.8	3.1	12.9	22.6	35.7	51.5	68.6	90.6
S.S.R.	0.040	0.052	0.035	0.082	0.038	0.035	0.042	0.097

* value corrected for Na-loss

[a] measured by FTIR

[b] calculated based on degree of crystallinity and composition of volatile-bearing minerals if present

mg# = Molar Mg/(Mg + Fe^{2+}) assuming an Fe^{2+}/Fe_{Tot} ratio of 0.85.

Table 5.8. Computed[†] bulk residual solid compositions from experiments on Hsynth Wet (1.67 wt. % bulk H_2O[a]) at 9.3 kbar

Experiment (No.)	3.026	3.029	3.022	3.023	3.027	3.028	3.030	3.032
Temperature (°C)	1250	1200	1150	1100	1050	1030	1000	980
SiO_2	0.00	26.3	34.5	40.3	43.5	44.2	45.6	46.2
TiO_2	0.45	0.14	0.14	0.14	0.17	0.50	0.66	0.60
Al_2O_3	9.26	3.05	1.90	2.03	2.36	5.87	7.86	10.1
Cr_2O_3	56.7	16.4	4.67	2.82	1.79	1.27	0.87	0.54
FeO	25.9	26.5	29.1	27.7	25.5	22.5	20.5	19.0
MnO	0.20	0.26	0.46	0.33	0.35	0.34	0.35	0.39
MgO	7.11	27.0	28.8	23.9	19.3	15.4	12.8	10.9
CaO	0.25	0.21	0.33	2.69	6.72	7.98	8.03	8.41
Na_2O	0.04	0.01	0.01	0.09	0.18	1.15	1.66	2.18[•]
K_2O	0.00	0.01	0.00	0.01	0.00	0.03	0.08	0.07
P_2O_5	0.02	0.05	0.04	0.08	0.15	0.14	0.44	0.65
H_2O	0.00	0.00	0.00	0.00	0.00	0.40[b]	0.68[b]	0.68[b]
F	0.00	0.00	0.00	0.00	0.00	0.42	0.73	0.56
Cl	0.00	0.00	0.00	0.00	0.00	0.02	0.04	0.05
-O = F + Cl	0.00	0.00	0.00	0.00	0.00	0.18	0.31	0.23
Total	99.9	99.9	100.0	100.1	100.0	100.1	100.0	100.1
mg#	0.36	0.68	0.67	0.64	0.61	0.59	0.57	0.55

[†] Computed from phase abundances

[•] Value calculated from plagioclase that was corrected for Na-loss

[a] measured by FTIR

[b] calculated based on crystal chemistry

mg# = Molar $Mg/(Mg + Fe^{2+})$ assuming an Fe^{2+}/Fe_{Tot} ratio of 0.85.

Examples of structural formulae calculations used for this work.

F. M. McCubbin[1]

[1]Department of Geosciences, State University of New York, Stony Brook NY 11794

6.1. Preface

Calculated structural formulae for minerals must take into account the requirements that (i) the abundance of cations and anions must lead to charge balanced stoichiometries and (ii) discrete crystallographic sites must be filled or the ratio of vacancy to occupancy known. They are most simply calculated based on either a fixed number of oxygens (for example 6 for the augite $Ca(Mg_{50}Fe_{50})Si_2O_6$) or on fixed total cation occupancies of specific sites (e.g., 1 for M1, 1 for M2, 2 for the tetrahedral site in this augite).

6.2. Anion/Oxygen Normalizations

Commonly, anion normalizations are based on the number of oxygens (or the number of -2 charges) in one stoichiometric unit. If monovalent anions are also present, normalization to a fixed number of oxygens can still be done when there is an even number of monovalent anions in the structure and oxygen and monovalent anions do not occupy the same crystallographic site. A sample anion normalization is provided in Figure 6.1.

In cases where oxygen and monovalent anions substitute on the same crystallographic site (i.e., kaersutite), the number of cations must be well constrained including the abundance of multivalent cations (e.g,. ferrous and ferric iron) before the structural formula can be calculated. Moreover, because oxygen is typically calculated by difference, the structural formulae of these minerals must be calculated iteratively until the sum of the monovalent anions and the oxygens completely fills the respective crystallographic site.

6.3. Cation Normalizations

Cation normalizations are based on a defined number of cations. Therefore, a structural formulae calculation based on cations assumes knowledge of the typical occupancies and site-assignments for cations within the mineral. In some cases, the valence state of one or more of the cations is unknown (i.e. ferrous/ferric ratio). Most typically, the valence state of iron is in question, and all other cations have one oxidation state. In these cases, the ferrous/ferric ratio can be calculated if the user has knowledge as to the total amount of negative charge within the respective mineral. A sample cation normalization is provided in Figure 6.2.

Cl-rich Amphibole 1 from Table 4.1												
Oxide		**Wt%**	**Mol wt oxide**	**Wt% / Mol wt**		**moles Oxygen unnorm**		**normalization to Oxygen**		**Amphibole formula**		
SiO_2		35.59	60	0.593167		1.186333		12.2867		Si	6.14	
TiO_2		0.24	79.87	0.003005		0.00601		0.062242		Ti	0.03	
Al_2O_3		10.37	102	0.101667		0.305		3.158844		Al	2.11	
Cr_2O_3		0.02	152	0.000132		0.000395		0.004088		Cr	0.00	
FeO		32.67	71.85	0.454697		0.454697		4.709239		Fe^{2+}	4.71	
Fe_2O_3		0.00	159.7	0		0		0		Fe^{3+}	0.00	
MnO		0.21	70.94	0.00296		0.00296		0.030659		Mn	0.03	
MgO		0.71	40.31	0.017613		0.017613		0.182421		Mg	0.18	
CaO		10.09	56	0.180179		0.180179		1.866085		Ca	1.87	
Na_2O		0.94	62	0.015161		0.015161		0.157023		Na	0.31	
K_2O		3.27	94	0.034787		0.034787		0.360287		K	0.72	
P_2O_5		0.5	141.94	0.003523		0.017613		0.182416		P	0.07	
Cl		6.23	35.45	0.17574		0.17574		1.820121				
Cl = -O		1.41										
	Total	99.43			Total	2.220749		23			16.18	
				normalization factor		10.35687						
				23	Oxygens							

Figure 6.1. Example calculation of amphibole structural formula based on a 23 oxygen normalization scheme. The amphibole used is the first amphibole analysis in Table 4.1.

Cl-rich Amphibole 1 from Table 4.1

Oxide		Wt%	Mol wt oxide	Wt% / Mol wt		moles of cations unnorm	normalization to cations	Raw formula	Charge test	Ferric calc	amphibole formula	
SiO_2		35.59	60	0.593167		0.593167	6.084747	6.08	24.33899	24.33899	Si	6.08
TiO_2		0.24	79.87	0.003005		0.003005	0.030824	0.03	0.123297	0.123297	Ti	0.03
Al_2O_3		10.37	102	0.101667		0.203333	2.085808	2.09	6.257425	6.257425	Al	2.09
Cr_2O_3		0.02	152	0.000132		0.000263	0.002699	0.00	0.008098	0.008098	Cr	0.00
FeO		32.67	71.85	0.454697		0.454697	4.664318	4.66	9.328636	8.451064	Fe^{2+}	4.23
Fe_2O_3		0.00	159.7					0.00	0	1.316359	Fe^{3+}	0.44
MnO		0.21	70.94	0.00296		0.00296	0.030366	0.03	0.060733	0.060733	Mn	0.03
MgO		0.71	40.31	0.017613		0.017613	0.180681	0.18	0.361361	0.361361	Mg	0.18
CaO		10.09	56	0.180179		0.180179	1.848285	1.85	3.69657	3.69657	Ca	1.85
Na_2O		0.94	62	0.015161		0.030323	0.311051	0.31	0.311051	0.311051	Na	0.31
K_2O		3.27	94	0.034787		0.069574	0.7137	0.71	0.71	0.7137	K	0.71
P_2O_5		0.5	141.94	0.003523		0.007045	0.07227	0.07	0.361352	0.361352	P	0.07
Cl		6.23	35.45	0.17574		0.17574	1.802759					
Cl = -O		1.41							-46	-46		
					Total	1.462263	15.95248	16.02				
	Total	99.43							-0.43879	0		16.02
					normalization factor for 15 Cat	10.25807						

Figure 6.2. Example calculation of amphibole structural formula based on a 15 cation normalization scheme. The amphibole used is the first amphibole analysis in Table 4.1. For this calculation, it was assumed that Si, Ti, Al, Cr, Fe, Mg, Mn, Cr, Ca and P should sum to 15 cations based on stoichiometry and substitution capabilities into the tetrahedral and octahedral sites (i.e., ionic radii and ionic charge). The A-site is not considered at this point. After the raw amphibole formula is obtained, we then sum the total positive charge for all cations, including those in the A-site. We then add the total negative charge to this value and calculate the residual charge (-0.44). This value was then used to calculate the amount of ferric iron in the amphibole and finally, the amphibole formula (The cation sum of 16.02 reflects the fact that we normalized the tetrahedral and octahedral sites to 15 cations, but there were additional cations in the A-site).

Bibliography

Albarede, F., Luais, B., Fitton, G., Semet, M., Kaminski, E., Upton, B. G. J., Bachelery, P., and Cheminee, J. L., 1997. The geochemical regimes of piton de la fournaise volcano (reunion) during the last 530,000 years. *Journal of Petrology* **38**, 171-201.

Alpers, C. N., Nordstrom, D. K., and Ball, J. W., 1989. Solubility of jarosite solid solutions precipitated from acid mine waters, iron mountain, california, USA. *Sciences Geologique. Bulletin.* **42**, 281-298.

Andersen, D. J., Lindsley, D. H., and Davidson, P. M., 1993. Quilf - a pascal program to assess equilibria among fe-mg-mn-ti oxides, pyroxenes, olivine, and quartz. *Computers & Geosciences* **19**, 1333-1350.

Aoudjehane, H. C., Jambon, A., and Boudouma, O., 2006. A cathodoluminescence study of cristobalite and k-feldspar in the nakhlite mil 03346. *Meteoritics & Planetary Science* **41**, A37-A37.

Bai, T. B. and van Groos, A. F. K., 1999. The distribution of na, k, rb, sr, al, ge, cu, w, mo, la, and ce between granitic melts and coexisting aqueous fluids. *Geochimica et Cosmochimica Acta* **63**, 1117-1131.

Baker, T., Van Achterberg, E., Ryan, C. G., and Lang, J. R., 2004. Composition and evolution of ore fluids in a magmatic-hydrothermal skarn deposit. *Geology* **32**, 117-120.

Bandfield, J. L., Hamilton, V. E., Christensen, P. R., and McSween, H. Y., 2004. Identification of quartzofeldspathic materials on mars. *Journal of Geophysical Research-Planets* **109**.

Beck, P., Barrat, J. A., Gillet, P., Wadhwa, M., Franchi, I. A., Greenwood, R. C., Bohn, M., Cotten, J., de Moortele, B. V., and Reynard, B., 2006. Petrography and geochemistry of the chassignite northwest africa 2737 (nwa 2737). *Geochimica Et Cosmochimica Acta* **70**, 2127-2139.

Bischoff, J. L., Rosenbauer, R. J., and Fournier, R. O., 1996. The generation of hcl in the system cacl2-h2o: Vapor-liquid relations from 380-500 degrees c. *Geochim. Cosmochim. Ac.* **60**, 7-16.

Boctor, N. Z., Alexander, C. M. O., Wang, J., and Hauri, E., 2003. The sources of water in martian meteorites: Clues from hydrogen isotopes. *Geochimica Et Cosmochimica Acta* **67**, 3971-3989.

Bolfan-Casanova, N., 2005. Water in the earth's mantle. *Mineralogical Magazine* **69**, 229-257.

Borg, L. E., Nyquist, L. E., Taylor, L. A., Wiesmann, H., and Shih, C. Y., 1997. Constraints on martian differentiation processes from rb-sr and sm-nd isotopic analyses of the basaltic shergottite que 94201. *Geochimica Et Cosmochimica Acta* **61**, 4915-4931.

Borg, L. E., Nyquist, L. E., Wiesmann, H., Shih, C. Y., and Reese, Y., 2003. The age of dar al gani 476 and the differentiation history of the martian meteorites inferred from their radiogenic isotopic systematics. *Geochimica Et Cosmochimica Acta* **67**, 3519-3536.

Boudreau, A. E., 1993. Chlorine as an exploration guide for the platinum-group elements in layered intrusions. *Journal of Geochemical Exploration* **48**, 21-37.

Boudreau, A. E., Love, C., and Prendergast, M. D., 1995. Halogen geochemistry of the great dyke, zimbabwe. *Contributions to Mineralogy and Petrology* **122**, 289-300.

Boudreau, A. E. and McCallum, I. S., 1989. Investigations of the stillwater complex: Part v. Apatites as indicators of evolving fluid composition. *Contributions to Mineralogy and Petrology* **102**, 138-153.

Boudreau, A. E. and McCallum, I. S., 1992. Infiltration metasomatism in layered intrusions -- an example from the stillwater complex, montana. *Journal of Volcanology and Geothermal Research* **52**, 171-183.

Brandon, A. D., Walker, R. J., Morgan, J. W., and Goles, C. G., 2000. Re-os isotopic evidence for early differentiation of the martian mantle. *Geochimica Et Cosmochimica Acta* **64**, 4083-4095.

Braun, M., Hartmann, P., and Jana, C., 1995. ^{19}f and ^{31}p nmr-spectroscopy of calcium apatites. *Journal of Materials Science-Materials in Medicine* **6**, 150-154.

Brese, N. E. and O'keeffe, M., 1991. Bond-valence parameters for solids. *Acta Crystallographica Section B-Structural Science* **47**, 192-197.

Breuer, D. and Spohn, T., 2003. Early plate tectonics versus single-plate tectonics on mars: Evidence from magnetic field history and crust evolution. *Journal of Geophysical Research-Planets* **108**.

Bridges, J. C., Catling, D. C., Saxton, J. M., Swindle, T. D., Lyon, I. C., and Grady, M. M., 2001. Alteration assemblages in martian meteorites: Implications for near-surface processes. *Space Science Reviews* **96**, 365-392.

Brophy, G. P. and Sheridan, M. F., 1965. Sulfate studies iv. Jarosite-natrojarosite-hydronium jarosite solid solution series. *American Mineralogist* **50**, 1595.

Bryce, D. L. and Sward, G. D., 2006. Solid-state nmr spectroscopy of the quadrupolar halogens: Chlorine-35/37, bromine-79/81, and iodine-127. *Magnetic Resonance in Chemistry* **44**, 409-450.

Bunch, T. and Reid, A., 1975. The nakhlites, part 1. Petrography and mineral chemistry. *Meteoritics* **10**, 303-315.

Burnham, C. W., 1994. Development of the burnham model for prediction of h_2o solubility in magmas, *Volatiles in magmas*.

Burnham, C. W. and Nekvasil, H., 1986. Equilibrium properties of granite pegmatite magmas. *American Mineralogist* **71**, 239-263.

Burns, R. G., 1986. Terrestrial analogs of the surface rocks of mars. *Nature* **320**, 55-56.

Burns, R. G., 1987. Ferric sulfates on mars. *Journal of Geophysical Research-Solid Earth and Planets* **92**, E570-E574.

Burns, R. G., 1988. Gossans on mars*Proceedings of the 18th Lunar and Planetary Science Conference*. LPI, Houston, TX.

Burns, R. G. and Fisher, D. S., 1990a. Evolution of sulfide mineralization on mars. *Journal of Geophysical Research-Solid Earth and Planets* **95**, 14169-14173.

Burns, R. G. and Fisher, D. S., 1990b. Iron-sulfur mineralogy of mars - magmatic evolution and chemical-weathering products. *Journal of Geophysical Research - Planets* **95**, 14415-14421.

Candela, P. A., 1986a. The evolution of aqueous vapor from silicate melts - effect on oxygen fugacity. *Geochimica et Cosmochimica Acta* **50**, 1205-1211.

Candela, P. A., 1986b. Toward a thermodynamic model for the halogens in magmatic systems - an application to melt vapor apatite equilibria. *Chemical Geology* **57**, 289-301.

Candela, P. A. and Piccoli, P. M., 1995. Model ore-metal partitioning from melts into vapor and vapor/brine mixtures., *Magmas, fluids, and ore deposits. Thompson, j. F. H., ed.* Mineralogical Association of Canada.

Carmichael, I. S. E., 1965. Trachytes and their feldspar phenocrysts. *Mineralogical Magazine and Journal of the Mineralogical Society* **34**, 107-125.

Carr, M. J., 2002. Igpet for windows. Terra Softa Inc., Somerset, NJ.

Carroll, M. R. and Webster, J. D., 1994. Solubilities of sulfur, noble-gases, nitrogen, chlorine, and fluorine in magmas, *Volatiles in magmas*.

Cesare, B., Satish-Kumar, M., Cruciani, G., Pocker, S., and Nodari, L., 2008. Mineral chemistry of ti-rich biotite from pegmatite and metapelitic granulites of the kerala khondalite belt (southeast india): Petrology and further insight into titanium substitutions. *Am. Mineral.* **93**, 327-338.

Christensen, P. R., McSween, H. Y., Bandfield, J. L., Ruff, S. W., Rogers, A. D., Hamilton, V. E., Gorelick, N., Wyatt, M. B., Jakosky, B. M., Kieffer, H. H., Malin, M. C., and Moersch, J. E., 2005. Evidence for magmatic evolution and diversity on mars from infrared observations. *Nature* **436**, 504-509.

Clark, B. C., Morris, R. V., McLennan, S. M., Gellert, R., Jolliff, B., Knoll, A. H., Squyres, S. W., Lowenstein, T. K., Ming, D. W., Tosca, N. J., Yen, A., Christensen, P. R., Gorevan, S., Bruckner, J., Calvin, W., Dreibus, G., Farrand, W., Klingelhoefer, G., Waenke, H., Zipfel, J., Bell, J. F., Grotzinger, J., McSween, H. Y., and Rieder, R., 2005. Chemistry and mineralogy of outcrops at meridiani planum. *Earth and Planetary Science Letters* **240**, 73-94.

Cornell, R. M. and Schwertmann, U., 2003. *The iron oxides: Structure, properties, reactions, occurrences and uses*. Wiley, Weinheim.

Cox, K. G., 1972. The karoo volcanic cycle. *Journal of the Geological Society, London* **128**, 311-336.

Cox, K. G., Bell, J. D., and Pankhurst, R. J., 1984. *The interpretation of igneous rocks*. George Allen & Unwin, London.

Danyushevsky, L. V., Leslie, R. A. J., Crawford, A. J., and Durance, P., 2004. Melt inclusions in primitive olivine phenocrysts: The role of localized reaction processes in the origin of anomalous compositions. *Journal of Petrology* **45**, 2531-2553.

Danyushevsky, L. V., Sokolov, S., and Falloon, T. J., 2002. Melt inclusions in olivine phenocrysts: Using diffusive re-equilibration to determine the cooling history of a crystal, with implications for the origin of olivine-phyric volcanic rocks. *Journal of Petrology* **43**, 1651-1671.

Day, J. M. D., Taylor, L. A., Floss, C., and McSween, H. Y., 2006. Petrology and chemistry of mil 03346 and its significance in understanding the petrogenesis of nakhlites on mars. *Meteoritics & Planetary Science* **41**, 581-606.

Dixon, J. E., Clague, D. A., and Stolper, E. M., 1991. Degassing history of water, sulfur, and carbon in submarine lavas from kilauea volcano, hawaii. *Journal of Geology* **99**, 371-394.

Domeneghetti, M. C., Fioretti, A. M., Camara, F., Carraro, A., McCammon, C., and Tazzoli, V., 2007. Constraints on the thermal history of martian meteorites alh84001 and mil03346 by single crystal xrd, electron mcroprobe and mossbauer analyses of ortho- and clinopyroxene*7th International Conference on Mars*, Pasadena, CA.

Domeneghetti, M. C., Fioretti, A. M., Camara, F., Molin, G., and McCammon, C., 2006. Constraints on the thermal history and oxidation state of mil03346 martian meteorite: Single-crystal xrd, electron microprobe and mossbauer analyses of clinopyroxene*Proceedings of the 37th Lunar and Planetary Science Conference*, Houston, TX.

Downs, R. T., 2006. The rruff project: An integrated study of the chemistry, crystallography, raman and infrared spectroscopy of minerals.*19th General Meeting of the International Mineralogical Association* Kobe, Japan.

Dyar, M. D., Treiman, A. H., Pieters, C. M., Hiroi, T., Lane, M. D., and O'Connor, V., 2005. Mil03346, the most oxidized martian meteorite: A first look at spectroscopy, petrography, and mineral chemistry. *Journal of Geophysical Research-Planets* **110**.

Eugster, H. P. and Skippen, G. B., 1967. Igneous and metamorphic reactions involving gas equilibria. In: Abelson, P. H. (Ed.), *Researches in geochemistry*. John Wiley, New York.

Farmer, C. B., Davies, D. W., and Laporte, D. D., 1976. Mars - northern summer ice cap - water-vapor observations from viking 2. *Science* **194**, 1339-1341.

Filiberto, J., 2008. Experimental constraints on the parental liquid of the chassigny meteorite: A possible link between the chassigny meteorite and a martian gusev basalt. *Geochimica Et Cosmochimica Acta* **72**, 690-701.

Filiberto, J. and Nekvasil, H., 2003. Linking tholeiites and silica-undersaturated alkalic rocks: An experimental study. *GSA Abstracts with Programs* **34**, 258-16.

Filiberto, J., Nekvasil, H., and Lindsley, D. H., 2006. The mars/earth dichotomy in mg/si and al/si ratios: Is it real? *American Mineralogist* **91**, 471-474.

Fisk, M. R. and Giovannoni, S. J., 1999. Sources of nutrients and energy for a deep biosphere on mars. *Journal of Geophysical Research-Planets* **104**, 11805-11815.

Floran, R. J., Prinz, M., Hlava, P. F., Keil, K., Nehru, C. E., and Hinthorne, J. R., 1978. Chassigny meteorite - cumulate dunite with hydrous amphibole-bearing melt inclusions. *Geochimica et Cosmochimica Acta* **42**, 1213-1229.

Foley, C. N., Wadhwa, M., Borg, L. E., Janney, P. E., Hines, R., and Grove, T. L., 2005. The early differentiation history of mars from w-182-nd-142 isotope systematics in the snc meteorites. *Geochimica Et Cosmochimica Acta* **69**, 4557-4571.

Gaetani, G. A. and Watson, E. B., 2002. Modeling the major-element evolution of olivine-hosted melt inclusions. *Chemical Geology* **183**, 25-41.

Gellert, R., Rieder, R., Bruckner, J., Clark, B. C., Dreibus, G., Klingelhofer, G., Lugmair, G., Ming, D. W., Wanke, H., Yen, A., Zipfel, J., and Squyres, S. W., 2006. Alpha particle x-ray spectrometer (apxs): Results from gusev crater and calibration report. *Journal of Geophysical Research-Planets* **111**.

Glotch, T. D. and Christensen, P. R., 2005. Geologic and mineralogic mapping of aram chaos: Evidence for a water-rich history. *Journal of Geophysical Research-Planets* **110**.

Glotch, T. D., Morris, R. V., Christensen, P. R., and Sharp, T. G., 2004. Effect of precursor mineralogy on the thermal infrared emission spectra of hematite: Application to martian hematite mineralization. *Journal of Geophysical Research-Planets* **109**.

Glotch, T. D. and Rogers, A. D., 2007. Evidence for aqueous deposition of hematite- and sulfate-rich light-toned layered deposits in aureum and iani chaos, mars. *Journal of Geophysical Research-Planets* **112**.

Golombek, M. P., Cook, R. A., Economou, T., Folkner, W. M., Haldemann, A. F. C., Kallemeyn, P. H., Knudsen, J. M., Manning, R. M., Moore, H. J., Parker, T. J., Rieder, R., Schofield, J. T., Smith, P. H., and Vaughan, R. M., 1997. Overview of the mars pathfinder mission and assessment of landing site predictions. *Science* **278**, 1743-1748.

Greenwood, J. P., 2005. Chlorine-rich apatites in sncs: Evidence for magma-brine interactions on mars? *Meteoritics & Planetary Science* **40**, A60-A60.

Grey, C. P. and Vega, A. J., 1995. Determination of the quadrupole coupling-constant of the invisible aluminum spins in zeolite hy with $^{1}h/^{27}al$ trapdor nmr. *Journal of the American Chemical Society* **117**, 8232-8242.

Gurov, E. P. and Koeberl, C., 2004. Shocked rocks and impact glasses from the el'gygytgyn impact structure, russia. *Meteoritics & Planetary Science* **39**, 1495-1508.

Halter, W. E. and Webster, J. D., 2004. The magmatic to hydrothermal transition and its bearing on ore-forming systems - preface. *Chemical Geology* **210**, 1-6.

Harper, C. L., Nyquist, L. E., Bansal, B., Wiesmann, H., and Shih, C. Y., 1995. Rapid accretion and early differentiation of mars indicated by nd-142 nd-144 in snc meteorites. *Science* **267**, 213-217.

Hartmann, W., 1979. Watery past of mars. *New Scientist* **82**, 1083-1085.

Haskin, L. A., Wang, A., Jolliff, B. L., McSween, H. Y., Clark, B. C., Des Marais, D. J., McLennan, S. M., Tosca, N. J., Hurowitz, J. A., Farmer, J. D., Yen, A., Squyres, S. W., Arvidson, R. E., Klingelhofer, G., Schroder, C., de Souza, P. A., Ming, D. W., Gellert, R., Zipfel, J., Bruckner, J., Bell, J. F., Herkenhoff, K., Christensen, P. R., Ruff, S., Blaney, D., Gorevan, S., Cabrol, N. A., Crumpler, L., Grant, J., and Soderblom, L., 2005. Water alteration of rocks and soils on mars at the spirit rover site in gusev crater. *Nature* **436**, 66-69.

Hauri, E., 2002. Sims analysis of volatiles in silicate glasses, 2: Isotopes and abundances in hawaiian melt inclusions. *Chemical Geology* **183**, 115-141.

Hauri, E., Wang, J. H., Dixon, J. E., King, P. L., Mandeville, C., and Newman, S., 2002. Sims analysis of volatiles in silicate glasses 1. Calibration, matrix effects and comparisons with ftir. *Chemical Geology* **183**, 99-114.

Hedenquist, J. W. and Lowenstern, J. B., 1994. The role of magmas in the formation of hydrothermal ore-deposits. *Nature* **370**, 519-527.

Herd, C. D. K., 2006. An occurrence of jarosite in mil 03346: Implications for conditions of martian aqueous alteration. *Meteoritics & Planetary Science* **41**, A74-A74.

Holland, H. D., 1972. Granites, solutions, and base metal deposits. *Economic Geology* **67**, 281-301.

Hughes, J. M., Cameron, M., and Crowley, K. D., 1989. Structural variations in natural f, oh, and cl apatites. *American Mineralogist* **74**, 870-876.

Hughes, J. M., Cameron, M., and Crowley, K. D., 1990. Crystal-structures of natural ternary apatites - solid-solution in the $ca_5(po_4)_3x$ (x= f, oh, cl) system. *American Mineralogist* **75**, 295-304.

Hughes, J. M. and Rakovan, J., 2002. The crystal structure of apatite, $ca_5(po_4)_3(f,oh,cl)$, *Phosphates: Geochemical, geobiological, and materials importance.*

Hurowitz, J. A. and McLennan, S. M., 2007. A similar to 3.5 ga record of water-limited, acidic weathering conditions on mars. *Earth and Planetary Science Letters* **260**, 432-443.

Imae, N. and Ikeda, Y., 2007. Petrology of the miller range 03346 nakhlite in comparison with the yamato-000593 nakhlite. *Meteoritics & Planetary Science* **42**, 171-184.

Jagoutz, E., Palme, H., Baddenhausen, H., Blum, K., Cendales, M., Dreibus, G., Spettel, B., Lorenz, V., and Wanke, H., 1979. The abundances of major, minor, and trace elements in the earth's mantle as derived from primitive ultramafic nodules. *Proceedings of the 10th Lunar and Planetary Science Conference*, 2031-2050.

Jakosky, B. M., 1999. Mars - water, climate, and life. *Science* **283**, 648-649.

Johnson, M. C., Rutherford, M. J., and Hess, P. C., 1991. Chassigny petrogenesis - melt compositions, intensive parameters, and water contents of martian (questionable) magmas. *Geochimica et Cosmochimica Acta* **55**, 349-366.

Jolliff, B. L., Haskin, L. A., Colson, R. O., and Wadhwa, M., 1993. Partitioning in ree-saturating minerals - theory, experiment, and modeling of whitlockite, apatite, and evolution of lunar residual magmas. *Geochimica Et Cosmochimica Acta* **57**, 4069-4094.

Kilinc, I. A. and Burnham, C. W., 1972. Partitioning of chloride between a silicate melt and coexisting aqueous phase from 2 to 8 kilobars. *Economic Geology* **67**, 231-235.

King, P. L., Hervig, R. L., Holloway, J. R., Delaney, J. S., and Dyar, M. D., 2000. Partitioning of fe3+/fe-total between amphibole and basanitic melt as a function of oxygen fugacity. *Earth Planet. Sc. Lett.* **178**, 97-112.

King, P. L. and McSween, H. Y., 2005. Effects of h2o, ph, and oxidation state on the stability of fe minerals on mars. *Journal of Geophysical Research-Planets* **110**.

Kleine, T., Mezger, K., Munker, C., Palme, H., and Bischoff, A., 2004. Hf-182-w-182 isotope systematics of chondrites, eucrites, and martian meteorites: Chronology of core formation and early mantle differentiation in vesta and mars. *Geochimica Et Cosmochimica Acta* **68**, 2935-2946.

Kleine, T., Munker, C., Mezger, K., and Palme, H., 2002. Rapid accretion and early core formation on asteroids and the terrestrial planets from hf-w chronometry. *Nature* **418**, 952-955.

Kullerud, K. and Erambert, M., 1999. Cl-scapolite, cl-amphibole, and piagioclase equilibria in ductile shear zones at nusfjord, lofoten, norway: Implications for fluid compositional evolution during fluid-mineral interaction in the deep crust. *Geochimica Et Cosmochimica Acta* **63**, 3829-3844.

Leake, B. E., 1978. Nomenclature of amphiboles. *Am. Mineral.* **63**, 1023-1052.

Leake, B. E., Woolley, A. R., Arps, C. E. S., Birch, W. D., Gilbert, M. C., Grice, J. D., Hawthorne, F. C., Kato, A., Kisch, H. J., Krivovichev, V. G., Linthout, K., Laird,

J., Mandarino, J. A., Maresch, W. V., Nickel, E. H., Rock, N. M. S., Schumacher, J. C., Smith, D. C., Stephenson, N. C. N., Ungaretti, L., Whittaker, E. J. W., and Guo, Y. Z., 1997. Nomenclature of amphiboles: Report of the subcommittee on amphiboles of the international mineralogical association, commission on new minerals and mineral names. *Can. Miner.* **35**, 219-246.

Lebas, M. J., Lemaitre, R. W., Streckeisen, A., and Zanettin, B., 1986. A chemical classification of volcanic-rocks based on the total alkali silica diagram. *Journal of Petrology* **27**, 745-750.

Lee, D. C. and Halliday, A. N., 1997. Core formation on mars and differentiated asteroids. *Nature* **388**, 854-857.

Leger, A., Rebbert, C., and Webster, J., 1996. Cl-rich biotite and amphibole from black rock forest, cornwall, new york. *American Mineralogist* **81**, 495-504.

Liebscher, A., 2007. Experimental studies in model fluid systems, *Fluid-fluid interactions*. Mineralogical Soc Amer, Chantilly.

Lieftink, D. J., Nijland, T. G., and Maijer, C., 1994. The behavior of rare-earth elements in high-temperature cl-bearing aqueous fluids - results from the odegardens-verk natural laboratory. *Canadian Mineralogist* **32**, 149-158.

Lindsley, D. H. and Nekvasil, H., 1989. A ternary feldspar model for all reasons. *EOS, Transactions of the American Geophysical Union* **70**, 506.

Lunine, J. I., Chambers, J., Morbidelli, A., and Leshin, L. A., 2003. The origin of water on mars. *Icarus* **165**, 1-8.

MacDonald, G. A., 1968. Composition and origin of hawaiian lavas. *Geological Society of America Memoir* **116**, 477-522.

Madden, M. E. E., Bodnar, R. J., and Rimstidt, J. D., 2004. Jarosite as an indicator of water-limited chemical weathering on mars. *Nature* **431**, 821-823.

Mandeville, C. W., Webster, J. D., Rutherford, M. J., Taylor, B. E., Timbal, A., and Faure, K., 2002. Determination of molar absorptivities for infrared absorption bands of h2o in andesitic glasses. *American Mineralogist* **87**, 813-821.

Mason, B., Nelen, J. A., Muir, P., and Taylor, S. R., 1975. The composition of the chassigny meteorite. *Meteoritics* **11**, 21-27.

Mathez, E. A., 1995. Magmatic metasomatism and formation of the merensky reef, bushveld complex. *Contributions to Mineralogy and Petrology* **119**, 277-286.

Mathez, E. A., Boudreau, A. E., and McCallum, I. S., 1985. Apatite and biotite from the stillwater and bushveld complexes and the nature of hydrothermal activity. *Canadian Mineralogist* **23**, 308-308.

Mathez, E. A. and Webster, J. D., 2005. Partitioning behavior of chlorine and fluorine in the system apatite-silicate melt-fluid. *Geochimica et Cosmochimica Acta* **69**, 1275-1286.

Mazdab, F. K., 2003. The diversity and occurrence of potassium-dominant amphiboles. *Can. Miner.* **41**, 1329-1344.

McCubbin, F. M. and Nekvasil, H., 2007. Volatile history of the martian chassigny dunite as told by the mineral phases.*7th International conference on Mars*, Pasadena, CA.

McCubbin, F. M. and Nekvasil, H., 2008. Maskelynite-hosted apatite in the chassigny meteorite: Insights into late-stage magmatic volatile evolution in martian magmas. *American Mineralogist* **93**, 676-684.

McCubbin, F. M., Nekvasil, H., Harrington, A. D., Elardo, S. M., and Lindsley, D. H., In Press-a. Compositional diversity and stratification of the martian crust: Inferences from crystallization experiments on the picrobasalt humphrey from gusev crater, mars. *J. Geophys. Res.-Planet.*

McCubbin, F. M., Nekvasil, H., Harrington, A. D., Elardo, S. M., and Lindsley, D. H., In Press-b. Compositional diversity and stratification of the martian crust: Inferences from crystallization experiments on the picrobasalt humphrey from gusev crater, mars. *Journal of Geophysical Research-Planets.*

McCubbin, F. M., Nekvasil, H., and Lindsley, D. H., 2006a. Apatite as a key to evaluating the volatile budget of martian magmas: Implications from the chassigny meteorite*Proceedings of the 37th Lunar and Planetary Science Conference*, Houston, TX.

McCubbin, F. M., Nekvasil, H., and Lindsley, D. H., 2006b. Oxy-component in kaersutite: How much can be a primary magmatic feature?*EOS (Transactions, American Geophysical Union)* AGU.

McCubbin, F. M., Nekvasil, H., and Lindsley, D. H., 2007a. Late-stage volatile evolution in martian magmas: Inferences from maskelynite-hosted apatite of the chassigny meteorite *Proceedings of the 38th Lunar and Planetary Science Conference.*

McCubbin, F. M., Nekvasil, H., Lindsley, D. H., and Filiberto, J., 2006c. The chemical nature of kaersutite experimentally produced at 0 kbar. *Proceedings of the 37th Lunar and Planetary Science Conference*, #1097.

McCubbin, F. M., Nekvasil, H., Smirnov, A., and Lindsley, D. H., 2007b. Kaersutite in the chassigny martian meteorite: How much water? *Geochimica et Cosmochimica Acta* **71**, A.

McEwen, A. S., Hansen, C. J., Delamere, W. A., Eliason, E. M., Herkenhoff, K. E., Keszthelyi, L., Gulick, V. C., Kirk, R. L., Mellon, M. T., Grant, J. A., Thomas, N., Weitz, C. M., Squyres, S. W., Bridges, N. T., Murchie, S. L., Seelos, F., Seelos, K., Okubo, C. H., Milazzo, M. P., Tornabene, L. L., Jaeger, W. L., Byrne, S., Russell, P. S., Griffes, J. L., Martinez-Alonso, S., Davatzes, A., Chuang, F. C., Thomson, B. J., Fishbaugh, K. E., Dundas, C. M., Kolb, K. J., Banks, M. E., and Wray, J. J., 2007. A closer look at water-related geologic activity on mars. *Science* **317**, 1706-1709.

McLennan, S. M., 2001. Crustal heat production and the thermal evolution of mars. *Geophysical Research Letters* **28**, 4019-4022.

McLennan, S. M., 2003. Large-ion lithophile element fractionation during the early differentiation of mars and the composition of the martian primitive mantle. *Meteoritics & Planetary Science* **38**, 895-904.

McLennan, S. M., Bell, J. F., Calvin, W. M., Christensen, P. R., Clark, B. C., de Souza, P. A., Farmer, J., Farrand, W. H., Fike, D. A., Gellert, R., Ghosh, A., Glotch, T. D., Grotzinger, J. P., Hahn, B., Herkenhoff, K. E., Hurowitz, J. A., Johnson, J. R., Johnson, S. S., Jolliff, B., Klingelhofer, G., Knoll, A. H., Learner, Z., Malin, M. C., McSween, H. Y., Pocock, J., Ruff, S. W., Soderblom, L. A., Squyres, S. W., Tosca, N. J., Watters, W. A., Wyatt, M. B., and Yen, A., 2005. Provenance and diagenesis of the evaporite-bearing burns formation, meridiani planum, mars. *Earth and Planetary Science Letters* **240**, 95-121.

McSween, H. Y. and Harvey, R. P., 1993. Outgassed water on mars - constraints from melt inclusions in snc meteorites. *Science* **259**, 1890-1892.

McSween, H. Y., Ruff, S. W., Morris, R. V., Bell, J. F., Herkenhoff, K. E., Gellert, R., Stockstill, K. R., Tornabene, L. L., Squyres, S. W., Crisp, J. A., Christensen, P. R., McCoy, T. J., Mittlefehldt, D. W., and Schmidt, M., 2006a. Alkaline volcanic rocks from the columbia hills, gusev crater, mars. *Journal of Geophysical Research - Planets* **111**, 15.

McSween, H. Y. and Treiman, A. H., 1998. Martian meteorites, *Planetary materials*.

McSween, Y., Wyatt, M. B., Gellert, R., Bell, J. F., Morris, R. V., Herkenhoff, K. E., Crumpler, L. S., Milam, K. A., Stockstill, K. R., Tornabene, L. L., Arvidson, R. E., Bartlett, P., Blaney, D., Cabrol, N. A., Christensen, P. R., Clark, B. C., Crisp, J. A., Des Marais, D. J., Economou, T., Farmer, J. D., Farrand, W., Ghosh, A., Golombek, M., Gorevan, S., Greeley, R., Hamilton, V. E., Johnson, J. R., Joliff, B. L., Klingelhofer, G., Knudson, A. T., McLennan, S., Ming, D., Moersch, J. E.,

Rieder, R., Ruff, S. W., Schroder, C., de Souza, P. A., Squyres, S. W., Wanke, H., Wang, A., Yen, A., and Zipfel, J., 2006b. Characterization and petrologic interpretation of olivine-rich basalts at gusev crater, mars. *Journal of Geophysical Research-Planets* **111**.

Merzbacher, C. and Eggler, D. H., 1984. A magmatic geohygrometer - application to mount st. Helens and other dacitic magmas. *Geology* **12**, 587-590.

Meurer, W. P. and Boudreau, A. E., 1996. An evaluation of models of apatite compositional variability using apatite from the middle banded series of the stillwater complex, montana. *Contributions to Mineralogy and Petrology* **125**, 225-236.

Milton, D. J. and Decarli, P. S., 1963. Maskelynite: Formation by explosive shock. *Science* **140**, 670-671.

Minitti, M. E., Leshin, L. A., Dyar, M. D., Ahrens, T. J., Guan, Y., and Luo, S. N., 2008a. Assessment of shock effects on amphibole water contents and hydrogen isotope compositions: 2. Kaersutitic amphibole experiments. *Earth Planet. Sc. Lett.* **266**, 288-302.

Minitti, M. E., Rutherford, M. J., Taylor, B. E., Dyar, M. D., and Schultz, P. H., 2008b. Assessment of shock effects on amphibole water contents and hydrogen isotope compositions: 1. Amphibolite experiments. *Earth Planet. Sc. Lett.* **266**, 46-60.

Monders, A. G., Medard, E., and Grove, T. L., 2007. Phase equilibrium investigations of the adirondack class basalts from the gusev plains, gusev crater, mars. *Meteoritics & Planetary Science* **42**, 131-148.

Monkawa, A., Mikouchi, T., Koizumi, E., Sugiyama, K., and Miyamoto, M., 2006. Determination of the fe oxidation state of the chassigny kaersutite: A microxanes spectroscopic study. *Meteoritics & Planetary Science* **41**, 1321-1329.

Morgan, G. B. and London, D., 1996. Optimizing the electron microprobe analysis of hydrous alkali aluminosilicate glasses. *American Mineralogist* **81**, 1176-1185.

Morgan, G. B. and London, D., 2005. Effect of current density on the electron microprobe analysis of alkali aluminosilicate glasses. *American Mineralogist* **90**, 1131-1138.

Morrison, J., 1991. Compositional constraints on the incorporation of cl into amphiboles. *American Mineralogist* **76**, 1920-1930.

Mottana, A., Sassi, F. P., Thompson, J. B., and Guggenheim, S., 2002. *Micas: Crystal chemistry and metamorphic petrology*. Mineralogical Society of America, Washington, D.C.

Mysen, B. O., Virgo, D., Popp, R. K., and Bertka, C. M., 1998. The role of h_2o in mmartian magmatic systems. *American Mineralogist* **83**, 942-946.

Nash, W. P., Carmichael, I. S. E., and Johnson, R. W., 1969. Mineralogy and petrology of mount suswa, kenya. *Journal of Petrology* **10**, 409-439.

Naumann, T. R. and Geist, D. J., 1999. Generation of alkalic basalt by crystal fractionation of tholeiitic magma. *Geology* **27**, 423-426.

Navrotsky, A., Forray, F. L., and Drouet, C., 2005. Jarosite stability on mars. *Icarus* **176**, 250-253.

Nekvasil, H., 1990. Reaction relations in the granite system: Implications for trachytic and syenitic magmas. *American Mineralogist* **75**, 560-571.

Nekvasil, H., 1992a. Feldspar crystallization in felsic magmas - a review. *Transactions of the Royal Society of Edinburgh* **83**, 399-407.

Nekvasil, H., 1992b. Ternary feldspar crystallization in high-temperature felsic magmas. *American Mineralogist* **77**, 592-604.

Nekvasil, H., 1994. Ternary feldspar/melt equilibria: A review, *Feldspars and their reactions*. Kluwer Academic Publishers, Parson, L. Ed., Netherlands.

Nekvasil, H., Dondolini, A., Horn, J., Filiberto, J., Long, H., and Lindsley, D. H., 2004. The origin and evolution of silica-saturated alkalic suites: An experimental study. *Journal of Petrology* **45**, 693-721.

Nekvasil, H., Filiberto, J., McCubbin, F. M., and Lindsley, D. H., 2007. Alkalic parental magmas for the chassignites? *Meteoritics & Planetary Science* **42**, 979-992.

Nekvasil, H., Filiberto, J., Whitaker, M. L., and Lindsley, D. H., 2003. Magmas parental to the chassigny meteorite: New considerations*6th International Conference on Mars*.

Nekvasil, H. and Lindsley, D. H., 1990. Termination of the 2-feldspar + liquid curve in the system ab-or-an-h_2o at low h_2o contents. *American Mineralogist* **75**, 1071-1079.

Norman, M. D., 1999. The composition and thickness of the crust of mars estimated from rare earth elements and neodymium-isotopic compositions of martian meteorites. *Meteoritics & Planetary Science* **34**, 439-449.

Nyquist, L. E., Bogard, D. D., Shih, C. Y., Greshake, A., Stoffler, D., and Eugster, O., 2001. Ages and geologic histories of martian meteorites. *Space Science Reviews* **96**, 105-164.

Ohmoto, H. and Rye, R. O., 1979. Isotopes of sulfur and carbon. In: Barnes, H. L. (Ed.), *Geochemistry of hydrothermal ore deposits*. Wiley, New York.

Pan, Y. M. and Fleet, M. E., 2002. Compositions of the apatite-group minerals: Substitution mechanisms and controlling factors, *Phosphates: Geochemical, geobiological, and materials importance.*

Papike, J. J., Karner, J. M., and Shearer, C. K., 2006. Comparative planetary mineralogy: Implications of martian and terrestrial jarosite. A crystal chemical perspective. *Geochimica Et Cosmochimica Acta* **70**, 1309-1321.

Phillips, B. L., 2000. Nmr spectroscopy of phase transitions in minerals, *Transformation processes in minerals*. Mineralogical Soc America, Washington.

Piccoli, P. M. and Candela, P. A., 2002. Apatite in igneous systems, *Phosphates: Geochemical, geobiological, and materials importance.*

Polovina, J. S., Hudson, D. M., and Jones, R. E., 2004. Petrographic and geochemical characteristics of postmagmatic hydrothermal alteration and mineralization in the j-m reef, stillwater complex, montana. *Canadian Mineralogist* **42**, 261-277.

Popp, R. K. and Bryndzia, L. T., 1992. Statistical analysis of fe^{3+}, ti, and oh in kaersutite from alkalic igneous rocks and mafic mantle xenoliths. *American Mineralogist* **77**, 1250-1257.

Popp, R. K., Hibbert, H. A., and Lamb, W. M., 2006. Oxy-amphibole equilibria in ti-bearing calcic amphiboles: Experimental investigation and petrologic implications for mantle-derived amphiboles. *American Mineralogist* **91**, 54-66.

Popp, R. K., Virgo, D., and Phillips, M. W., 1995a. H deficiency in kaersutitic amphiboles: Experimental verification. *American Mineralogist* **80**, 1347-1350.

Popp, R. K., Virgo, D., Yoder, H. S., Hoering, T. C., and Phillips, M. W., 1995b. An experimental-study of phase-equilibria and fe oxy-component in kaersutitic amphibole - implications for the $f_{(h2)}$ and $a_{(h2o)}$ in the upper-mantle. *American Mineralogist* **80**, 534-548.

Righter, K., Dyar, M. D., Delaney, J. S., Vennemann, T. W., Hervig, R. L., and King, P. L., 2002. Correlations of octahedral cations with oh^-, o^{2-}, cl^-, and f^- in biotite from volcanic rocks and xenoliths. *Am. Mineral.* **87**, 142-153.

Ritchey, J. L., 1980. Divergent magmas at crater lake, oregon: Products of fractional crystallization and vertical zoning in a shallow, water-undersaturated chamber. *Journal of Volcanology and Geothermal Research* **7**, 373-386.

Robie, R. A. and Hemingway, D. S., 1995. Thermodynamic properties of minerals and related substances at 298.15 k and 1 bar (105 pascals) pressure and at higher temperatures. In: Survey, U. G. (Ed.).

Rogers, A. D. and Christensen, P. R., 2007. Surface mineralogy of martian low-albedo regions from mgs-tes data: Implications for upper crustal evolution and surface alteration. *Journal of Geophysical Research-Planets* **112**.

SAINT, 2002. *Bruker-AXS: Madison, WI.*

Sassi, R., Cruciani, G., Mazzoli, C., Nodari, L., and Craven, J., 2008. Multiple titanium substitutions in biotites from high-grade metapelitic xenoliths (euganean hills, italy): Complete crystal chemistry and appraisal of petrologic control. *Am. Mineral.* **93**, 339-350.

Sato, H., Yamaguchi, Y., and Makino, K., 1997. Cl incorporation into successively zoned amphiboles from the ramnes cauldron, norway. *American Mineralogist* **82**, 316-324.

Sautter, V., Jambon, A., and Boudouma, O., 2006. Cl-amphibole in the nakhlite mil 03346: Evidence for sediment contamination in a martian meteorite. *Earth and Planetary Science Letters* **252**, 45-55.

Scoates, J. S., Lindsley, D. H., van der Kolk, D., and Anderson, K., 1999. Fractional crystallization experiments on a candidate parental magma to anorthosite. *EOS, Transactions of the American Geophysical Union* **80**, F1096.

Sharma, A., Scott, J. H., Cody, G. D., Fogel, M. L., Hazen, R. M., Hemley, R. J., and Huntress, W. T., 2002. Microbial activity at gigapascal pressures. *Science* **295**, 1514-1516.

Sheldrick, G. M., 2000. Shelxtl, 6.10. *Bruker-AXS: Madison, WI.*

Sheldrick, G. M., 2001. Sadabs, a program for the siemens area detector absorption. *Bruker-AXS: Madison, WI.*

Shmulovich, K., Heinrich, W., Moller, P., and Dulski, P., 2002. Experimental determination of ree fractionation between liquid and vapour in the systems nacl-h2o and cacl2-h2o up to 450 degrees c. *Contrib. Mineral. Petr.* **144**, 257-273.

Shmulovich, K. I., Tkachenko, S. I., and Plyasunova, N. V., 1995. Phase equilibria in fluid systems at high pressures and temperatures. In: Shmulovich, K. I., Yardley,

B. W. D., and Gonchar, G. A. Eds.), *Fluids in the crust: Equilibrium and transport properties*. Chapman and Hall, London.

SMART, 2001. *Bruker-AXS: Madison, WI.*

Squyres, S. W., Arvidson, R. E., Blaney, D. L., Clark, B. C., Crumpler, L., Farrand, W. H., Gorevan, S., Herkenhoff, K. E., Hurowitz, J., Kusack, A., McSween, H. Y., Ming, D. W., Morris, R. V., Ruff, S. W., Wang, A., and Yen, A., 2006a. Rocks of the columbia hills. *Journal of Geophysical Research-Planets* **111**.

Squyres, S. W., Grotzinger, J. P., Arvidson, R. E., Bell III, J. F., Christensen, P. R., Clark, B. C., Crisp, J. A., Farrand, W., Herkenhoff, K. E., Johnson, J. R., Klingelhöfer, G., Knoll, A. H., McLennan, S. M., McSween, H. Y., Morris, R. V., Rice, J. W., Rieder, R., and Soderblom, L. A., 2004. In-situ evidence for an ancient aqueous environment at meridiani planum, mars. *Science* **306**, 1709.

Squyres, S. W., Knoll, A. H., Arvidson, R. E., Clark, B. C., Grotzinger, J. P., Jolliff, B. L., McLennan, S. M., Tosca, N., Bell, J. F., Calvin, W. M., Farrand, W. H., Glotch, T. D., Golombek, M. P., Herkenhoff, K. E., Johnson, J. R., Klingelhofer, G., McSween, H. Y., and Yen, A. S., 2006b. Two years at meridiani planum: Results from the opportunity rover. *Science* **313**, 1403-1407.

Squyres, S. W., Knoll, A. H., Arvidson, R. E., Clark, B. C., Grotzinger, J. P., Jolliff, B. L., McLennan, S. M., Tosca, N. J., Bell, J. F., Calvin, W. M., Farrand, W. H., Glotch, T. D., Golombek, M. P., Herkenhoff, K. E., Johnson, J. R., Klingelhoefer, G., McSween, H. Y., and Yen, A. S., 2006c. Two years at meridiani planum: Results from the opportunity rover. *Science* **313**, 1403-1407.

Stalder, R., Foley, S. F., Brey, G. P., and Horn, I., 1998. Mineral aqueous fluid partitioning of trace elements at 900-1200°c and 3.0-5.7 gpa: New experimental data for garnet, clinopyroxene, and rutile, and implications for mantle metasomatism. *Geochimica et Cosmochimica Acta* **62**, 1781-1801.

Stoffregen, R. E., 1993. Stability relations of jarosite and natrojarosite at 150-250°c. *Geochimica et Cosmochimica Acta* **57**, 2417.

Stoffregen, R. E., Alpers, C. N., and Jambor, J. L., 2000. Alunite-jarosite crystallography, thermodynamics and geochronology. In: Alpers, C. N., Jambor, J. L., and Nordstrom, D. K. Eds.), *Sulfate minerals: Crystallography, geochemistry and environmental significance*. Mineralogical Society of America, Washington, D.C.

Stormer, J. C., Pierson, M. L., and Tacker, R. C., 1993. Variation of f-x-ray and cl-x-ray intensity due to anisotropic diffusion in apatite during electron-microprobe analysis. *American Mineralogist* **78**, 641-648.

Sudarsanan, K. and Young, R. A., 1969. Significant precision in crystal structural details - holly springs hydroxyapatite. *Acta Crystallographica Section B-Structural Crystallography and Crystal Chemistry* **B 25**, 1534-&.

Tacker, R. C. and Stormer, J. C., 1989. A thermodynamic model for apatite solid-solutions, applicable to high-temperature geologic problems. *American Mineralogist* **74**, 877-888.

Taylor, G. J., Boynton, W., Bruckner, J., Wanke, H., Dreibus, G., Kerry, K., Keller, J., Reedy, R., Evans, L., Starr, R., Squyres, S., Karunatillake, S., Gasnault, O., Maurice, S., d'Uston, C., Englert, P., Dohm, J., Baker, V., Hamara, D., Janes, D., Sprague, A., Kim, K., and Drake, D., 2006. Bulk composition and early differentiation of mars. *Journal of Geophysical Research-Planets* **111**.

Taylor, L. A., Patchen, A., Mayne, R. G., and Taylor, D. H., 2004. The most reduced rock from the moon, apollo 14 basalt 14053: Its unique features and their origin. *American Mineralogist* **89**, 1617-1624.

Taylor, S. R., 2001. *Solar system evolution: A new perspective.* Cambridge University Press.

Thompson, R. N., 1975. Primary basalts and magma genesis .2. Snake river plain, idaho, USA. *Contributions to Mineralogy and Petrology* **52**, 213-232.

Tosca, N. J., Knoll, A. H., and McLennan, S. M., 2008a. Water activity and the challenge for life on early mars. *Science* **320**, 1204-1207.

Tosca, N. J., McLennan, S. M., Clark, B. C., Grotzinger, J. P., Hurowitz, J. A., Knoll, A. H., Schroder, C., and Squyres, S. W., 2005. Geochemical modeling of evaporation processes on mars: Insight from the sedimentary record at meridiani planum. *Earth and Planetary Science Letters* **240**, 122-148.

Tosca, N. J., McLennan, S. M., Dyar, M. D., Sklute, E. C., and Michel, F. M., 2008b. Fe oxidation processes at meridiani planum and implications for secondary fe mineralogy on mars. *J. Geophys. Res.-Planet* **113**.

Treiman, A. H., 2005. The nakhlite meteorites: Augite-rich igneous rocks from mars. *Chemie Der Erde-Geochemistry* **65**, 203-270.

Vanko, D. A., 1986. High-chlorine amphiboles from oceanic rocks - product of highly-saline hydrothermal fluids. *American Mineralogist* **71**, 51-59.

Varela, M. E., Kurat, G., Bonnin-Mosbah, M., Clocchiatti, R., and Massare, D., 2000. Glass-bearing inclusions in olivine of the chassigny achondrite: Heterogeneous trapping at sub-igneous temperatures. *Meteoritics & Planetary Science* **35**, 39-52.

Veksler, I. V., 2006. Crystallized melt inclusions in gabbroic rocks, *Melt inclusions in plutonic rocks, webster, j. D. Ed.* Mineralogical Association of Canada, Montreal.

Vicenzi, E. P., Fries, M., Fahey, A., Rost, D., Greenwood, J. P., and Steele, A., 2007a. Detailed elemental, mineralgical, and isotopic examination of jarosite in martian meteorite mil 03346*Poceedings of the Lunar and Planetary Science Conference XXXVIII* Houston, TX.

Vicenzi, E. P., Fries, M., Fahey, A., Rost, D., Greenwood, J. P., and Steele, A., 2007b. Evidence for young jarosite precipiation on mars. *Meteoritics and Planetary Science* **42**, A157.

Wadhwa, M. and Crozaz, G., 1995. Trace and minor elements in minerals of nakhlites and chassigny - clues to their petrogenesis. *Geochimica et Cosmochimica Acta* **59**, 3629-3645.

Wanke, H. and Dreibus, G., 1994. Chemistry and accretion history of mars. *Philosophical Transactions of the Royal Society of London Series a-Mathematical Physical and Engineering Sciences* **349**, 285-293.

Wanke, H., Dreibus, G., Jagoutz, E., Palme, H., Spettel, B., and Weckwerth, G., 1986. Alha 77005 and on the chemistry of the shergotty parent body (mars). *Lunar and Planetary Science, XVII*, 919-920.

Watson, L. L., Hutcheon, I. D., Epstein, S., and Stolper, E. M., 1994. Water on mars - clues from deuterium/hydrogen and water contents of hydrous phases in snc meteorites. *Science* **265**, 86-90.

Webster, J. D., 1992a. Fluid-melt interactions involving cl-rich granites - experimental study from 2 to 8 kbar. *Geochimica et Cosmochimica Acta* **56**, 659-678.

Webster, J. D., 1992b. Water solubility and chlorine partitioning in cl-rich granitic systems - effects of melt composition at 2 kbar and 800°c. *Geochimica et Cosmochimica Acta* **56**, 679-687.

Webster, J. D., 1997a. Chloride solubility in felsic melts and the role of chloride in magmatic degassing. *Journal of Petrology* **38**, 1793-1807.

Webster, J. D., 1997b. Exsolution of magmatic volatile phases from cl-enriched mineralizing granitic magmas and implications for ore metal transport. *Geochimica et Cosmochimica Acta* **61**, 1017-1029.

Webster, J. D., 2004. The exsolution of magmatic hydrosaline chloride liquids. *Chemical Geology* **210**, 33-48.

Webster, J. D. and De Vivo, B., 2002. Experimental and modeled solubilities of chlorine in aluminosilicate melts, consequences of magma evolution, and implications for exsolution of hydrous chloride melt at mt. Somma-vesuvius. *American Mineralogist* **87**, 1046-1061.

Webster, J. D., Kinzler, R. J., and Mathez, E. A., 1999. Chloride and water solubility in basalt and andesite melts and implications for magmatic degassing. *Geochimica et Cosmochimica Acta* **63**, 729-738.

Webster, J. D. and Mandeville, C. W., 2007. Fluid immiscibility in volcanic environments, *Fluid-fluid interactions*.

Webster, J. D. and Rebbert, C. R., 1998. Experimental investigation of h_2o and cl^- solubilities in f-enriched silicate liquids; implications for volatile saturation of topaz rhyolite magmas. *Contributions to Mineralogy and Petrology* **132**, 198-207.

Wen, S. X. and Nekvasil, H., 1994. Solvcalc - an interactive graphics program package for calculating the ternary feldspar solvus and for 2-feldspar geothermometry. *Computers & Geosciences* **20**, 1025-1040.

Whitaker, M. L., Nekvasil, H., and Lindsley, D. H., 2005. Potential magmatic diversity on mars*Proceedings of the Lunar and Planetary Science Conference XXXVI*.

Whitaker, M. L., Nekvasil, H., Lindsley, D. H., and Difrancesco, N. J., 2007. The role of pressure in producing compositional diversity in intraplate basaltic magmas. *Journal of Petrology* **48**, 365-393.

White, T. J. and Dong, Z. L., 2003. Structural derivation and crystal chemistry of apatites. *Acta Crystallographica Section B-Structural Science* **59**, 1-16.

Wieczorek, M. A. and Zuber, M. T., 2004. Thickness of the martian crust: Improved constraints from geoid-to-topography ratios. *Journal of Geophysical Research-Planets* **109**.

Willmore, C. C., Boudreau, A. E., and Kruger, F. J., 2000. The halogen geochemistry of the bushveld complex, republic of south africa: Implications for chalcophile element distribution in the lower and critical zones. *Journal of Petrology* **41**, 1517-1539.

Wright, J. B., 1970. High pressure phases in nigerian cenozoic lavas, distribution and geotectonic setting. *Bulletin of Volcanology* **34**, 833-847.

Yesinowski, J. P. and Eckert, H., 1987. Hydrogen environments in calcium phosphates ^1h mas nmr at high spinning speeds. *Journal of the American Chemical Society* **109**, 6274-6282.

Yin, Q. Z., Jacobsen, S. B., Yamashita, K., Blichert-Toft, J., Telouk, P., and Albarede, F., 2002. A short timescale for terrestrial planet formation from hf-w chronometry of meteorites. *Nature* **418**, 949-952.

Zeng, Q. and Nekvasil, H., 1996. An associated solution model for albite-water melts. *Geochimica et Cosmochimica Acta* **60**, 59-73.

Zeng, Q., Nekvasil, H., and Grey, C. P., 2000. In support of a depolymerization model for water in sodium aluminosilicate glasses: Information from nmr spectroscopy. *Geochimica et Cosmochimica Acta* **64**, 883-896.

Zhu, C. and Sverjensky, D. A., 1991. Partitioning of f-cl-oh between minerals and hydrothermal fluids. *Geochimica et Cosmochimica Acta* **55**, 1837-1858.